Final Report

Evaluation of Weather Modification Modeling in the Wind River Range, WY

Sarah Tessendorf, Lulin Xue, Dan Breed, Courtney Weeks, Kyoko Ikeda, Duncan Axisa, Roy Rasmussen

Research Applications Laboratory (RAL)

National Center for Atmospheric Research (NCAR)

2015-11-30

Report prepared by NCAR for

The U.S. Bureau of Reclamation

Weather Modification Modeling Evaluation in the Wind River Range, WY

Table of Contents

LIST OF FIGURES

LIST OF TABLES

Evaluation of Weather Modification Modeling in the Wind River Range, WY

Executive Summary

The purpose of this project is to evaluate the potential for cloud seeding using numerical cloud models and to assist forecasters in identifying opportunities for cloud seeding over the Wind River Range in Wyoming. Three tasks were included in this project: 1) deployment of instrumentation to help identify cloud seeding opportunities and evaluate the model, 2) a climatological analysis that utilized an 8-year high-resolution model dataset to evaluate the cloud seeding potential of storms in the Wind River Range, and 3) real-time forecast modeling activities including adapting a real-time forecast model to identify cloud seeding opportunities over the region and simulate seeding in those cases.

The Wyoming Water Development Commission (WWDC) funded an operational ground-based cloud seeding program in the Wind River Range for the 2014–2015 winter season. Weather Modification Incorporated (WMI) was the contractor that operated the program. WMI forecasters launched soundings from Pinedale, Wyoming to assess if atmospheric conditions were suitable for seeding. They also utilized radiometer data (Task 1) and real-time model forecasts tailored to the Wind River Range (Task 3) to determine when to seed. There were 21 cloud seeding cases called during the 2014–2015 operational cloud seeding season; 11 on the west slope of the Range.

As part of Task 1, a microwave radiometer and two weather stations were deployed along the west slope of the Wind River Range. In addition to being utilized by WMI forecasters during the 2014–2015 winter seeding season, the radiometer data was also utilized for model evaluation studies. The radiometer data indicated that liquid water was present in all of the operational seeding cases on the west slope.

For the second task, an eight-year average seasonal precipitation characteristics and frequency of seeding opportunities by either ground or airborne seeding techniques on both the west and east slopes of the Wind River Range was identified. The typical wind regimes were shown to be westerly to northwesterly, with some southwesterly events, as well as some easterly events on the eastern slopes of the Wind River Range. The analysis showed that the most frequent seeding opportunities were on the western slopes of the Range.

For the eight-year period analyzed, Snow Telemetry (SNOTEL) precipitation gauge data showed that the November–April period brings about a half of the annual precipitation to the Wind River Range region. The model indicated that the precipitation is 20 to 100% higher at the crest as compared to the locations of the SNOTEL sites, but this cannot be confirmed without observational data at those higher elevations. For the 8-year period analyzed, the model compared well with the SNOTEL observations within known measurement error.

Airborne seeding potential had similar frequencies as ground seeding. A key limitation of ground-based seeding is that the wind direction and stability can limit the dispersion of the silver iodide (AgI) plume up and over the mountain barrier. If both ground and airborne

seeding criteria are considered, roughly 45% more of a given winter season could be seeded relative to a ground-based program alone. An interesting and unexpected finding from the climatology analysis was the potential for airborne seeding outside of the November–April period. The results indicated that year-round airborne seeding could provide, on average, 100 additional seeding hours beyond the number of seedable hours when snow occurred in the November–April period. This suggests the possibility to extend snowpack augmentation activities into the beginning of the runoff season.

For the third task, the Real-Time Four Dimensional Data Assimilation (RT-FDDA) version of the Weather Research and Forecasting (WRF) model was run in real time during the 2014–2015 winter season over the Wind River Range. WMI forecasters utilized this tailored forecast model output, along with the real-time data from the microwave radiometer, to identify cloud seeding opportunities during the operational seeding program. Software engineering work was completed to set up a real-time cloud seeding forecast system with the RT-FDDA model. The cloud seeding forecast system included a "case-calling" algorithm that was adapted to run on the RT-FDDA model output to automatically assess the forecast conditions for cloud seeding opportunities, and then, when cloud seeding opportunities were identified by the algorithm, a second forecast model simulation was initiated that explicitly simulated cloud seeding to provide a forecast of the simulated effects from seeding. The cloud seeding forecast system was run retrospectively for the 2014–2015 season and results from those model simulations were analyzed to provide an estimate of the potential seasonal impact from seeding and to compare the model-identified seeding cases with those identified by the forecasters in order to improve the case-calling algorithm. The model results were also compared against observations from the radiometer and other available measurements to evaluate the model's performance.

An important finding was that the model results simulated on average a less than 1% seeding effect over the Range for ground-based seeding for the 2014–2015 season. The likely reason for this was the presence of stable layers in the upstream sounding, causing the ground generator AgI plumes to be largely diverted around the Range. Adding airborne seeding increased the simulated seeding effect, as it was able to target the upper liquid water layer without being significantly blocked by the Range. Additional years of analysis are needed, including sounding data, to confirm this result.

Based on the results of this report, we provide eight recommendations related to improving the efficacy of the cloud seeding program in the Wind River Range.

1) We recommend running the real-time cloud seeding forecast system in real time for additional Wyoming operational seeding seasons. There are at least three purposes for these recommended model simulations:
    a. It would provide a tailored forecast model for operational forecasters that would include forecast trajectories from generators and simulated seeding effects forecasts prior to the forecaster calling cases.
    b. The seasonal seeding forecast model output can be used to assess *seasonal* simulated seeding effects for the various basins. This provides a means to evaluate the operational program while also helping proportion where the benefits may accrue, which can help in determining future cost share arrangements.

   c. It would provide multiple years of simulated seeding effects in order to evaluate how the seasonal simulated seeding impacts vary by season, thereby also resolving if the 2014–2015 season was anomalous. A key aspect of this effort would be to collect and analyze sounding data for each event in order to determine the stability of the air upstream of the Range.
2) We recommend further refinement to the case-calling algorithm to better match operational case calling.
3) We recommend continued radiometer measurements and local soundings to identify seeding cases in the region. These data also provide valuable data for validation of any associated modeling activities. If funds allow, we would recommend a second radiometer on the northwestern side of the Range to capture the high liquid water contents identified in the eight year climatology that often occurred independent of the liquid water content observed by the Boulder radiometer.
4) We recommend the deployment of snow gauges along the crest of the Wind River Range to obtain precipitation measurements to verify the model results in this portion of the Range. The model suggests that the highest snowfall occurs in this region, and thus it is important to know whether this is true or not. This recommendation is challenging due to land use and ownership in those regions, but is a need nonetheless. We recommend using the model eight-year dataset to identify the best sites by doing a correlation analysis between existing gauge sites and potential new sites to identify the best, yet fewest, locations needed for additional gauges.
5) We recommend considering airborne seeding in the region to extend the seeding season, while also providing additional opportunities for seeding, especially for cases that are stable and limit the potential for ground-based seeding dispersion of AgI over the target area.
6) As a follow-on recommendation to #1, we recommend developing a real-time integrated display of the model and observations, which includes the model output compared to observations for real-time model verification, to aid forecasters in cloud seeding case calling.
7) Conduct additional analysis on the eight-year model dataset by running the case-calling algorithm to identify cases, and conducting both ground and airborne seeding simulations on cases so identified. Annual simulated seeding impacts due to ground, airborne, and the two combined would be estimated and related to the stability of the oncoming flow. This differs from Recommendation #1c in that sounding data would not be available to verify the results, but has the advantage of considering multiple years without having to wait for multiple future seeding seasonal forecasts to be run as in Recommendation #1.
8) Future studies should evaluate the ability of the model to vertically disperse AgI from the ground generators over the complex terrain of the Wind River Range using a Large Eddy Simulation approach.

1. Introduction

The purpose of this project was to utilize numerical cloud models to evaluate the cloud seeding potential over the Wind River Range as well as assist forecasters in identifying opportunities over this Range. Three tasks were included in this project: 1) deployment of instrumentation to assist with identifying cloud seeding opportunities and for use in model evaluation, 2) a climatological analysis that utilized an eight-year high-resolution model output to evaluate the cloud seeding potential of storms in the Wind River Range, and 3) real-time forecast modeling activities including adapting a real-time forecast model to identify cloud seeding opportunities over the region and simulate seeding in those cases.

1.1. Task Overview

1.1.1. Task 1: Deploy Instrumentation

The goal of this task was to deploy and operate a microwave radiometer near Boulder, Wyoming during the winter 2014–2015 and make the data from the radiometer available in near real-time via a website and also archived for later model evaluation efforts. The radiometer provides critical liquid water path (LWP) data for the operational cloud seeding program forecasters and for verification data for the modeling efforts. In addition, this task aimed to deploy and operate meteorological instrumentation and precipitation gauges at accessible sites in the Wind River Range to aid in evaluation of the model simulations.

1.1.2. Task 2: Climatology Analyses

The purpose of this task was to create a climatology of supercooled liquid water (SLW) over the Wind River Range using an eight-year high-resolution modeling dataset produced by the Colorado Headwaters project (Rasmussen et al. 2014). The simulations will be verified by comparison to existing Snow Telemetry (SNOTEL) precipitation gauges and other available data. A key outcome of this task will include an estimate of the percent of time that seedable conditions are present in winter storms impacting the region. The data will be stratified by storm character (such as cloud top temperature, stability, and wind speed) in order to gain an understanding of the type of storms that occur in the region.

1.1.3. Task 3: Cloud Seeding Modeling

The goal of this task was to quantify the potential impact of cloud seeding on the distribution and amount of precipitation in winter storms by adapting the NCAR cloud seeding forecast system for the Wind River Range and provide the proper configuration of the system that could be used as a decision support tool for cloud seeding operations in this region. The system was incorporated into the Real-time Four Dimensional Data Assimilation (RT-FDDA) numerical forecasting system that was run for the Wyoming Weather Modification Pilot Project (WWMPP). Prior to this, the seeding module was run in a non-real-time system for Wyoming. The model will be verified with available data, such as that from the radiometer, SNOTEL gauges, and atmospheric soundings launched by Weather Modification Incorporated (WMI) in Pinedale, Wyoming.

Under this task, the modeling system will be tested by running it in real-time for the domain surrounding the Wind River Range for the period of November 15, 2014–April 15, 2015.

1.2. Relation to the Wyoming Wind River Range Operational Program

The Wyoming Water Development Commission (WWDC) funded an operational ground-based cloud seeding program in the Wind River Range for the 2014–2015 winter season (Figure 1.1). WMI was the contractor that operated the program. WMI forecasters launched soundings from Pinedale to assess if atmospheric conditions were suitable for seeding. They also utilized the radiometer data (Task 1) and RT-FDDA model forecasts tailored to the Wind River Range (Task 3) to determine when to seed.

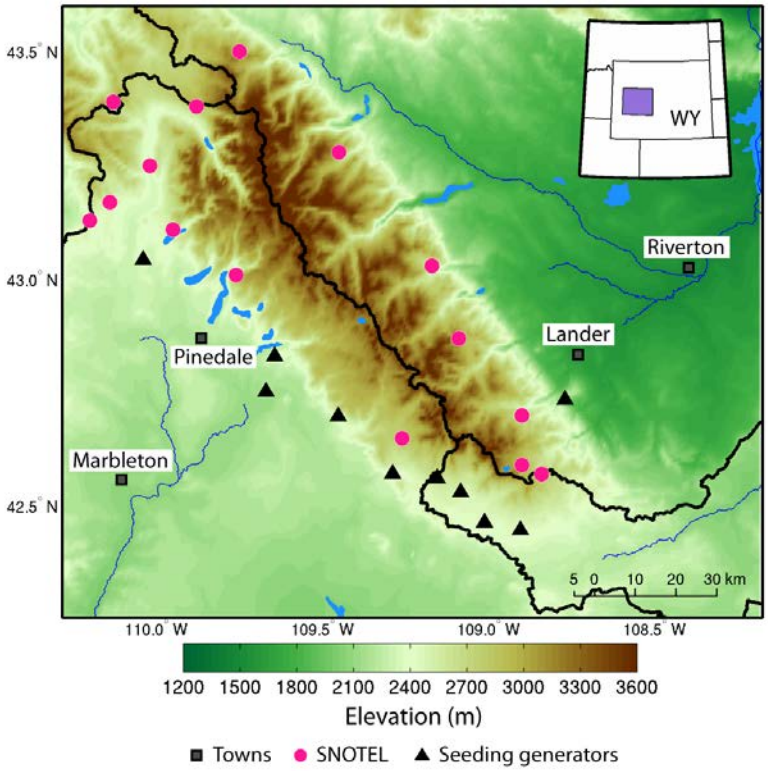

Figure 1.1. Map of the Wind River Range (terrain height in meters) illustrating the locations of the 2014-2015 facilities: ground-based seeding generators, SNOTEL gauges, radiometer site, and met stations. The WMI soundings were launched from Pinedale. National Weather Service (NWS) soundings are launched from Riverton.

Twenty-one cases were seeded during the 2014–2015 operational seeding program (see Table 1.1). Interestingly, nearly half were cases occurred on the east slope in this particular season.

Table 1.1. Table of the cases seeded in the Wind River Range by the operational program run by WMI during the 2014-2015 winter season. Cases shaded in gray were focused on the east slope of the Wind River Range, utilizing the one ground generator on that slope (at Enterprise).

Wind River Operational Seeding Cases 2014-2015

Case Number	Date (UTC)	Start Time (UTC)	End Date (UTC)	End Time (UTC)	Generators run
1	20141115	7:10	20141115	12:46	1, 2, 3, 9, 10, 12, 13
2	20141130	8:21	20141130	13:24	1, 2, 3, 9, 10, 12, 13
3	20141201	16:51	20141202	7:10	1, 2, 3, 9, 10, 12, 13
4	20141214	8:08	20141215	4:20	7 = Enterprise
5	20141220	2:13	20141220	10:09	2,3,9,10,13
6	20141220	22:38	20141221	16:20	1,2,3,9,10,12,13
7	20141225	1:44	20141225	13:24	1,2,3,4,5,9,10,12,13
8	20141225	18:15	20141226	8:26	7 = Enterprise
9	20141229	4:49	20141229	5:40	7 = Enterprise
10	20150105	6:05	20150105	19:05	9,10,12,13
11	20150116	21:26	20150117	8:32	1,2,3,9,10,12,13
12	20150215	15:52	20150215	18:29	7 = Enterprise
13	20150216	14:26	20150216	20:35	7 = Enterprise
14	20150221	15:19	20150222	6:21	7 = Enterprise
15	20150225	18:52	20150226	4:09	7 = Enterprise
16	20150226	20:41	20150227	0:23	7 = Enterprise
17	20150303	3:41	20150303	8:00	1,2,3,4,5,9,10,12,13
18	20150303	11:48	20150303	22:13	1,2,3,4,5,9,10,12,13
19	20150324	16:36	20150325	2:56	1,2,3,4,5,9,10,12,13
20	20150402	15:09	20150403	7:16	7 = Enterprise
21	20150415	14:11	20150415	18:16	7 = Enterprise

2. Task 1: Deploy Instrumentation

Observations are needed to evaluate seeding conditions and for comparison with numerical model results. Determining seeding conditions requires measurements pertinent to seeding criteria, such as temperature, winds, and SLW. Integrated path measurements of SLW were made from a microwave radiometer located just to the west of the Range at Boulder, Wyoming.

Figure 2.1 shows the locations of the instruments along with the ground-based seeding generators used in the seeding operations by WMI. The radiometer was co-located with a seeding generator as it has been for several winter seasons. The two weather stations were co-located with National Atmospheric Deposition Program (NADP) sites. Details of the instrument operation and deployment are explained in the following with examples of the data collected.

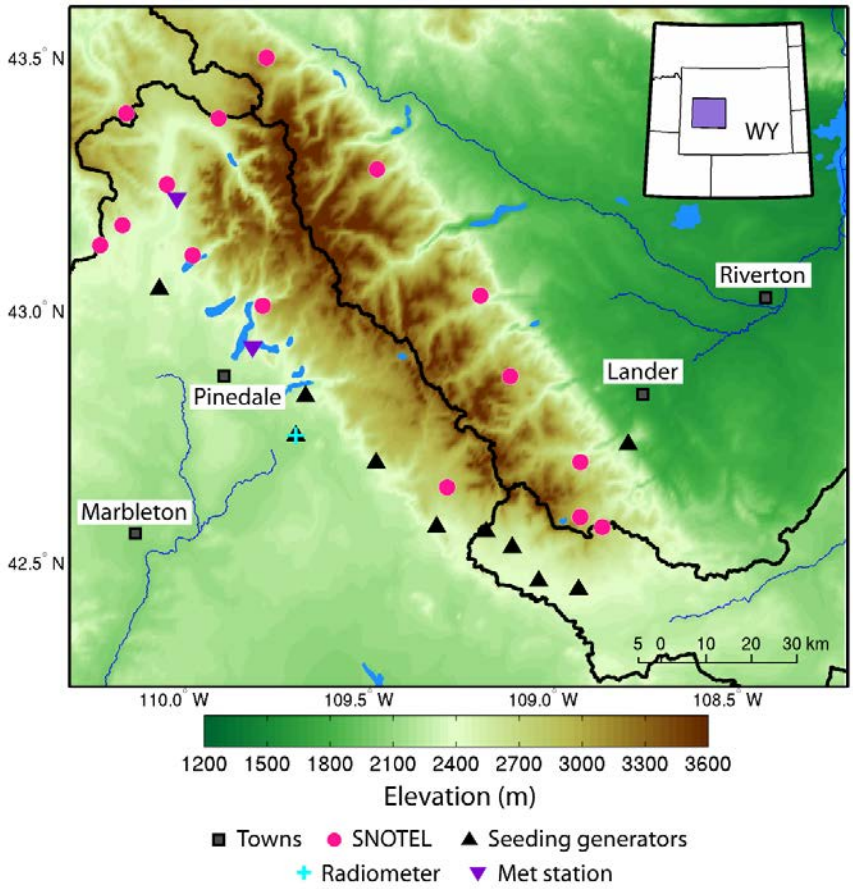

Figure 2.1. Map of the Wind River Range showing layout of measurement and operational networks. A special radiosonde site was operated by WMI at Pinedale; the nearest NWS radiosonde site was located at Riverton. Locations of SNOTELs, seeding generators, the radiometer, and the weather stations are marked with symbols as noted in the legend.

2.1. Radiometer

2.1.1. Overview

Microwave radiometers are instruments that derive integrated or path values of water vapor and liquid water. Radiometers with multiple channels can also provide profiles of these quantities and temperature, if equipped with an infrared sensor. Radiosonde measurements or soundings are able to directly profile or derive the same quantities, while microwave radiometers indirectly derive these values through measurement of the microwave emissions of the vapor and liquid water molecules in the atmosphere at specific frequencies. Radiometers can provide data updates much more frequently than information from a sounding, but they do not make direct measurements and the data tend to be much more smoothed (depending on the number of channels) than data from a sounding. Still, radiometers are able to provide important data on the moisture quantities in the atmosphere that allow a forecaster to determine whether enough liquid water exists to make seeding operations effective and allow a researcher to compare numerical model results with observations.

For the radiometer used in this study, microwave detection of water vapor and liquid water and the ability to derive profiles of water vapor make use of atmospheric radiation measurements in the 22 to 30 GHz region. A water vapor resonance feature exists at 22.2 GHz that is pressure broadened according to the pressure altitude of the water vapor distribution (Figure 2.2). The cloud liquid water emission spectrum increases approximately with the second power of frequency in this region. Using these characteristics and average thermodynamic profiles from radiosonde soundings, Radiometrics profiling radiometers can produce vertical profiles of water vapor from the surface to 10 km in height.

The Radiometrics model (WVP-1500) used in the Wind River area detects microwave emissions from the sky at five frequencies to produce the water vapor profiles and integrated LWP. For the purposes of this study, only two frequencies or channels are used to calculate integrated liquid water (zenith-referenced), which was plotted in real time for operational use as well as for post-analysis. The raw data for all the radiometers are archived for more precise calculations of LWP as needed.

The two channels used for calculating real-time LWP from the WVP-1500 model are 23.85 GHz and 30.0 GHz. Four years of radiosonde data from Riverton, Wyoming were used to calculate retrieval coefficients for the months of November–December and January–March. A weighted average of the coefficients from these two time periods is used in the liquid water calculations. Furthermore, all LWP calculations are corrected to the vertical (zenith referenced) so that values at different pointing angles are all consistent and comparable. Errors or biases in the calculated liquid water values occur due to: 1) diurnal variations; 2) longer term variations (i.e., monthly); 3) weather system changes that are substantially different than the average radiosonde parameters (resulting in large-scale pressure changes, for example); 4) scattering or other ground effects at low elevation angles; 5) amplification of small errors in converting low elevation angles to the zenith reference; and 6) instrument errors or calibration changes. The most significant variation typically comes from (3) while instrument effects (6) tend to be quite small in relation to the other sources

of bias. The resultant plots of LWP often have a baseline different than zero, but relative indications of cloud liquid water can be detected at very small values (typically 0.02 mm or less). A baseline correction is applied after the fact for absolute LWP comparisons with numerical model results.

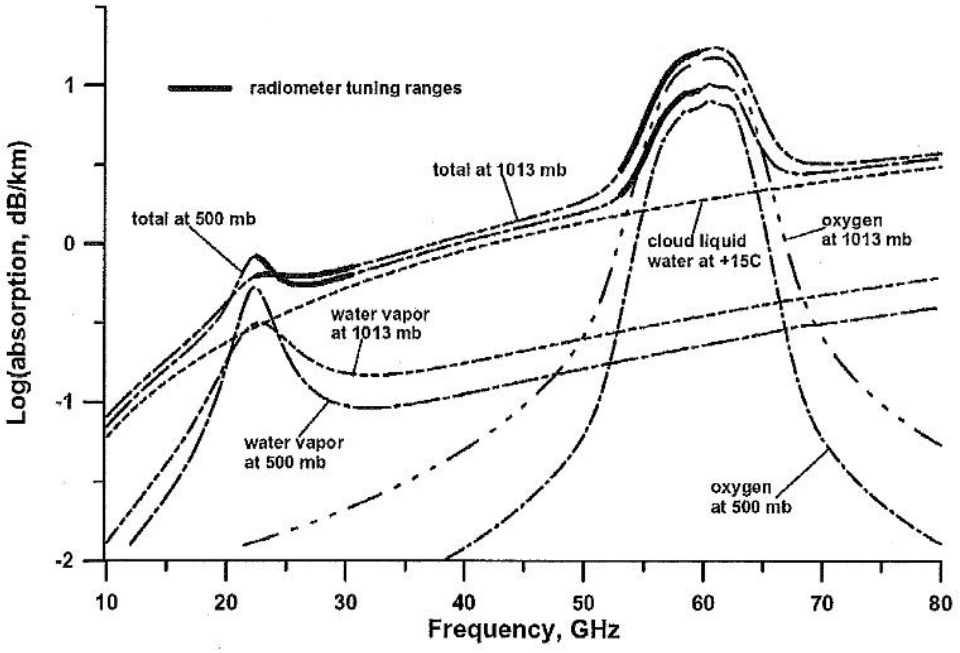

Figure 2.2. Atmospheric absorption as a function of frequency in the microwave range. Absorption curves due to water vapor, cloud liquid water, as well as the total are shown for various conditions. The WVP-1500 series operates in the range of 22-30 GHz; note the water vapor band around 22 GHz. (Figure courtesy of Radiometrics Corp.)

2.1.2. Siting and operational summary

Similar to the past seven years, the Wind River (aka Boulder) radiometer was located at a site east of Boulder, WY (coordinates: 42.7528° N, 109.6702° W; elevation: 7040 ft mean sea level [MSL]), co-located with the East Fork silver iodide (AgI) seeding generator (Figure 2.1). The radiometer set-up and viewing angle are shown in Figure 2.3.

The WVP-1500, which is the model installed at the Boulder site, is a five-channel radiometer capable of producing water vapor profiles and liquid water path. Besides obtaining a profile at the zenith angle, the Wind River radiometer collected data at elevation angles of 8°, 12°, 15°, and 30° along a fixed azimuth angle of ~65° (±5°).

For the 2014–2015 season, the radiometer was installed on 14 November 2014 and operated until 2 May 2015. The very few periods of missing data during the season were caused by the usual problems encountered in the past (e.g., power outages and Internet connectivity issues). However, the radiometer operation during the 2014–2015 season was quite robust and much more consistent than all past seasons. Only three outages occurred during the season, each about 20 hours long.

Figure 2.3. Radiometer at Boulder, Wyoming looking east towards the central Wind River Range (obscured by weather). Ground-based seeding generator at the same location is visible in the left background.

2.1.3. Data analysis and quality control

The radiometer data contained a drifting baseline, which resulted in an additive bias in the non-zero data. The baseline for the radiometer data at Boulder was corrected using asymmetric least squares smoothing (AsLS, Eilers and Boelens 2005), in which the baseline is estimated iteratively with a smoothing function that weights positive deviations much less than negative ones (see Figure 2.4 for an example). AsLS requires tuning of smoothness (λ) and asymmetry (p) parameters. As this method is very sensitive to spurious negative spikes, they were manually removed prior to baseline correction. The parameters were estimated by hand and refined for sub periods if needed.

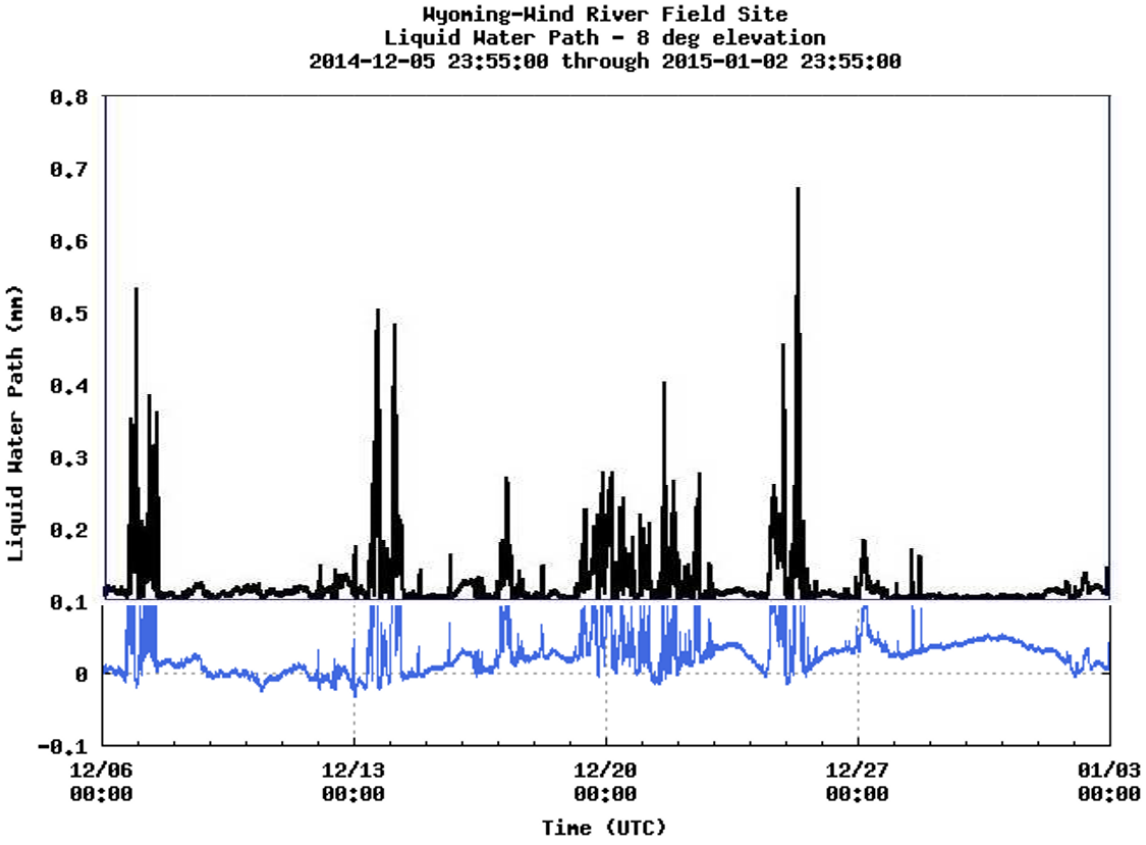

Figure 2.4. An example of the baseline correction (AsLS technique), applied to 8° elevation radiometer data from the Wind River site for the period 6 December 2014 to 3 January 2015. Uncorrected data are shown in blue and corrected data, shifted by 0.1 mm, in black.

A two-week time-series plot from the period of operation is presented in Figure 2.5. Two elevation angles that target low-lying clouds over the mountains are shown (8° and 12°). While the 8° data should provide the most useful information on supercooled cloud liquid water over the mountains, they are also the most susceptible to ground-effects since the beam width of the radiometer is 5–6° with side-lobes extending another 5° or so. However, over several seasons in the WWMPP, the 8° radiometer data showed no signs of ground-effects and should be the most representative of LWP for storms over the central Wind River Range.

The presence of SLW, which assumes that the LWP observed by the radiometer is in clouds entirely colder than 0° C, is only one criterion in the seeding decision. Cold enough temperatures for AgI to activate effectively and winds that provide a trajectory from the seeding generators to the higher terrain are also required, which are determined by complementary soundings and model forecasts. An example where LWP appears to be adequate, but other conditions were not amenable to seeding operations, can be seen on 6, 9, and 12 January 2015 (Figure 2.5). Early in the storm periods, the temperatures (not

shown) tended to be too warm, and as the cold front moved through, the temperatures dropped but the winds shifted to northwesterly becoming unfavorable.

Over the course of the 2014–2015 season, twenty-one seeding periods occurred in the Wind River Range (see Table 1.1). Figure 2.6 presents a three-day time-series plot centered on three of the 21 cases. As discussed above, the radiometer data show only one criterion in the seeding decision. The plots of the cases merely show the cloud conditions at and around the time of case calling. Also, even though cloud conditions do not appear favorable throughout the seeding period of some of the cases, decisions were made in real time based on model forecasts as well as the recent liquid water history revealed in the radiometer data. Correlating the radiometer data with numerical model output and temperature and wind observations provides a better means for analyzing case-calling criteria and the case-calling procedure.

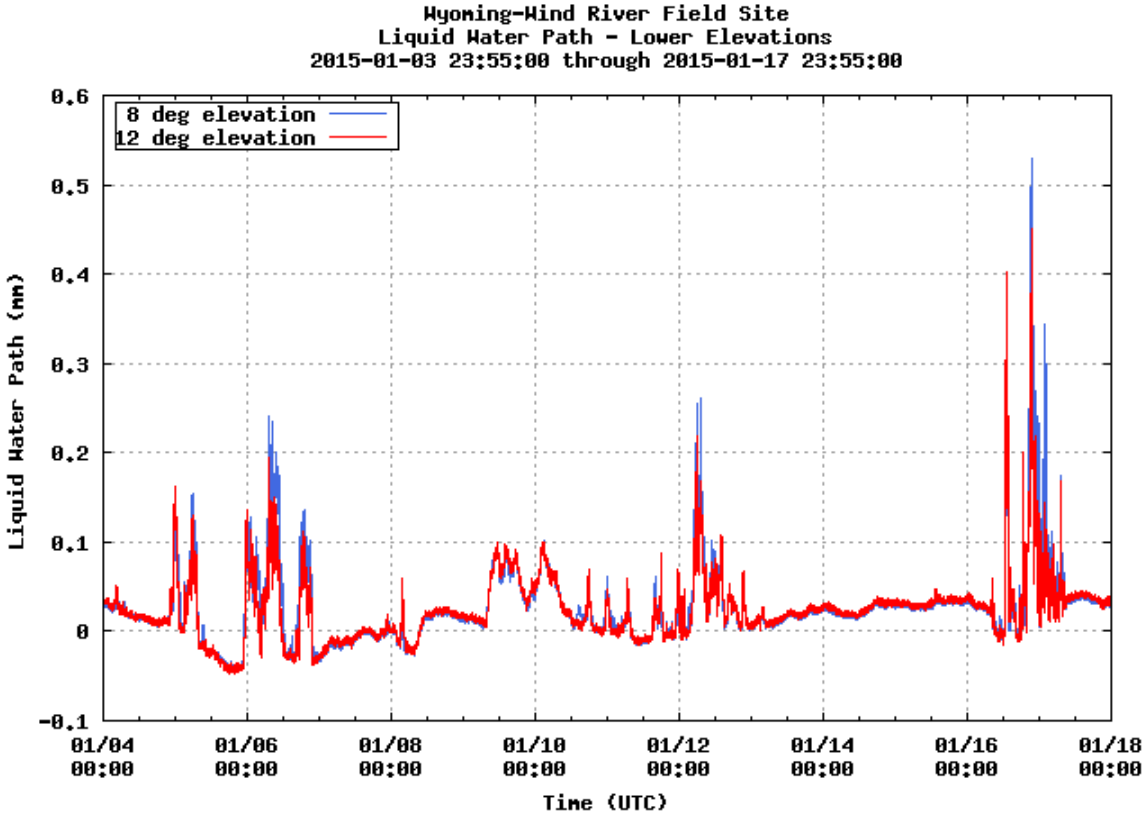

Figure 2.5. Two-week time-series plot (uncorrected) for the period 4–17 January 2015 of LWP in mm at 8° and 12° elevation angles from the Wind River radiometer. Two storms were seeded during this time period – one on 5 January 2015 and a second on 16 January 2015.

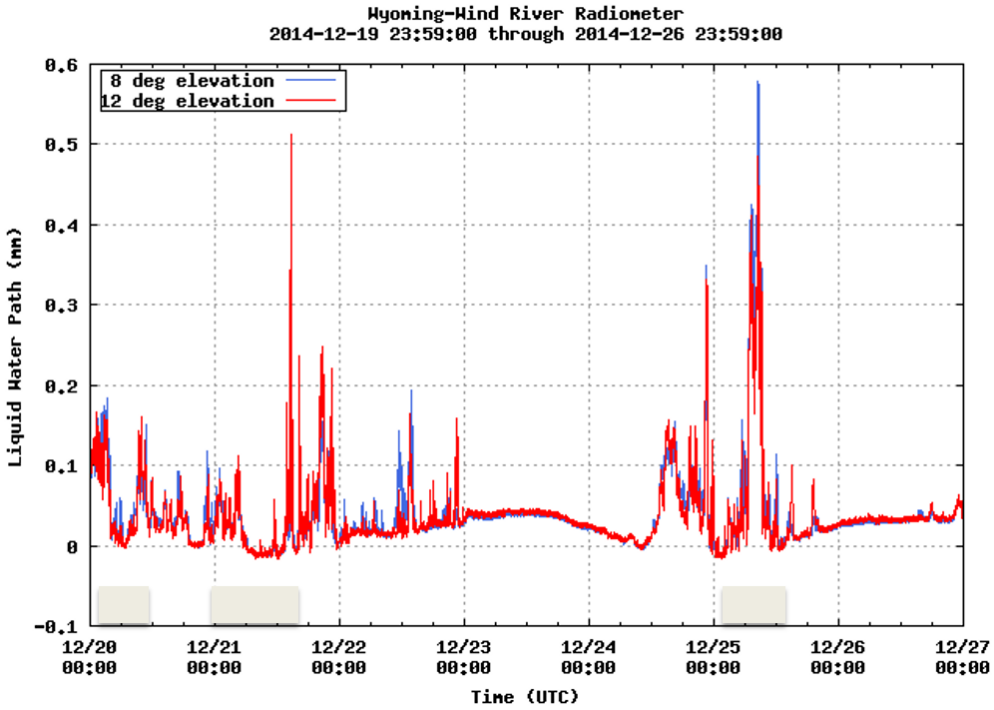

Figure 2.6. Time series of radiometer-observed LWP data at 8- and 12-degree elevation angles (blue and red, respectively) from 19–26 December 2014, with three seeding periods highlighted (light shading at the bottom of the plot).

2.1. Surface stations

Several different sources of meteorological data were available during the 2014–2015 season at variable resolutions and frequencies. SNOTEL observations were used extensively as climatological benchmarks. Since the SNOTEL sites only report hourly accumulations (and some with even less frequency), they are not ideally suited for high-resolution measurements. A Vaisala WXT510 weather transmitter was installed at six of the ground-based seeding generators. The WXT510 measured winds, temperature, humidity, pressure, and precipitation. However, the data were not recorded regularly because there were no data loggers installed with the sensor. About 13 hours of data (every 10 min) were manually downloaded during a seeding period from only the sensors on those generators that were operated. So, the data from these weather stations were not consistent over the season and from storm to storm. Another very limited data source was the temperature and humidity measurements from the radiometer, which were recorded about every minute.

High-resolution meteorological and precipitation observations were proposed to supplement the other irregular data sources. Permission from the US Forest Service (USFS) to locate the weather stations on USFS land was required and was an arduous task. Therefore, installation of the stations was delayed, causing very little data to be collected during the season. Instruments could only be installed at two of the three proposed sites. The weather station sites measured winds (including gusts), temperature, humidity, solar

radiation, soil moisture and snow depth every 5 min. They were co-located with the NADP sites, which measured precipitation – Gypsum Creek and Fremont Lake.

2.1.1. Siting and operational summary

Table 2.1 lists the locations of the weather stations associated with the extra sensors at the NADP sites and the locations of the ground-based generator sites, six of which have WXT510 sensors. The sites are listed north to south with the last site (Enterprise) located on the southeast side of the Wind River Range. These locations can be cross-referenced to the map in Figure 2.1.

Twenty-one seeding events occurred during the season, resulting in 21 periods of WXT510 data (Table 1.1). The high-resolution weather stations recorded data from 13 April to 30 May 2015.

Table 2.1. Weather station (NADP) sites and ground-based generator sites.

Site Name	Latitude	Longitude	Elevation (ft)	Sensors
Gypsum Creek	43.2227	-109.9917	7,982	Meteorological sensors and NADP site (near Kendall R.S. SNOTEL)
Green River	43.0440	-110.0399	7,967	WXT510 (only two cases)
Fremont Lake	42.9290	-109.7875	7,864	Meteorological sensors and NADP site (near Elkhart SNOTEL)
Boulder Lake	42.8309	-109.6438	7,803	WXT510
East Fork	42.7523	-109.6697	7,040	Radiometer - collocated
Pocket Creek	42.6983	-109.4525	7,822	WXT510
Big Sandy Opening	42.6082	-109.3094	7,923	WXT510
Block and Tackle	42.5611	-109.1547	8,512	None
White Acorn Ranch	42.5303	-109.0839	8,333	WXT510
Sweetwater	42.4624	-109.0125	7,818	None
Anderson Ridge	42.4461	-108.9044	7,978	None
Enterprise	42.7355	-108.7703	6,708	WXT510

2.1.2. Data analysis examples

A two-week plot of ambient temperature and LWP over the same January time period as that of Figure 2.5 is shown in Figure 2.7. This is an example of data from the radiometer location, roughly midway between the seeding generators (see Figure 2.1). Another example that depicts seeding conditions is given in Figure 2.8. White Acorn temperature

and wind direction data from the WXT10 sensor are plotted over a 12-hr period, 1900 UTC 2 March 2015–0700 UTC 3 March 2015. This time frame represents a seeding period from 0341–0800 UTC 3 March 2015. The temperature plot shows cold air engulfing the southern station (White Acorn) later and falling a few degrees colder than at the radiometer location along the Wind River Range. These fine-scale features of wind direction, temperature, and other variables (not shown) highlight the variations in seeding conditions over small distances and the potential coarseness of numerical model output used for decision-making. Additional weather stations provide data that can be used to compare and adjust seeding criteria as provided from numerical model output.

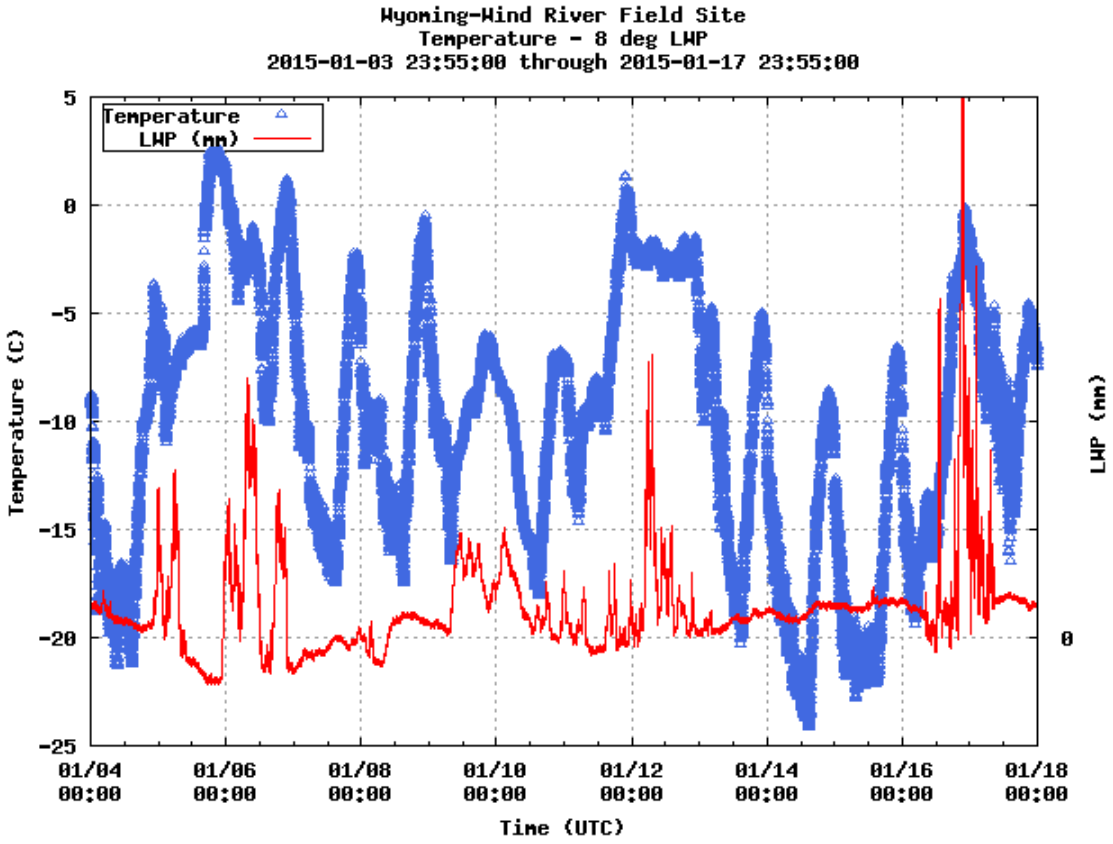

Figure 2.7. Two-week time-series plot for the period 4 –17 January 2015 of LWP (uncorrected) in mm at 8° elevation angle and ambient temperature (C) from the Wind River radiometer. The LWP data range from –0.1 to 0.5 mm. Time period is the same as in Figure 2.5.

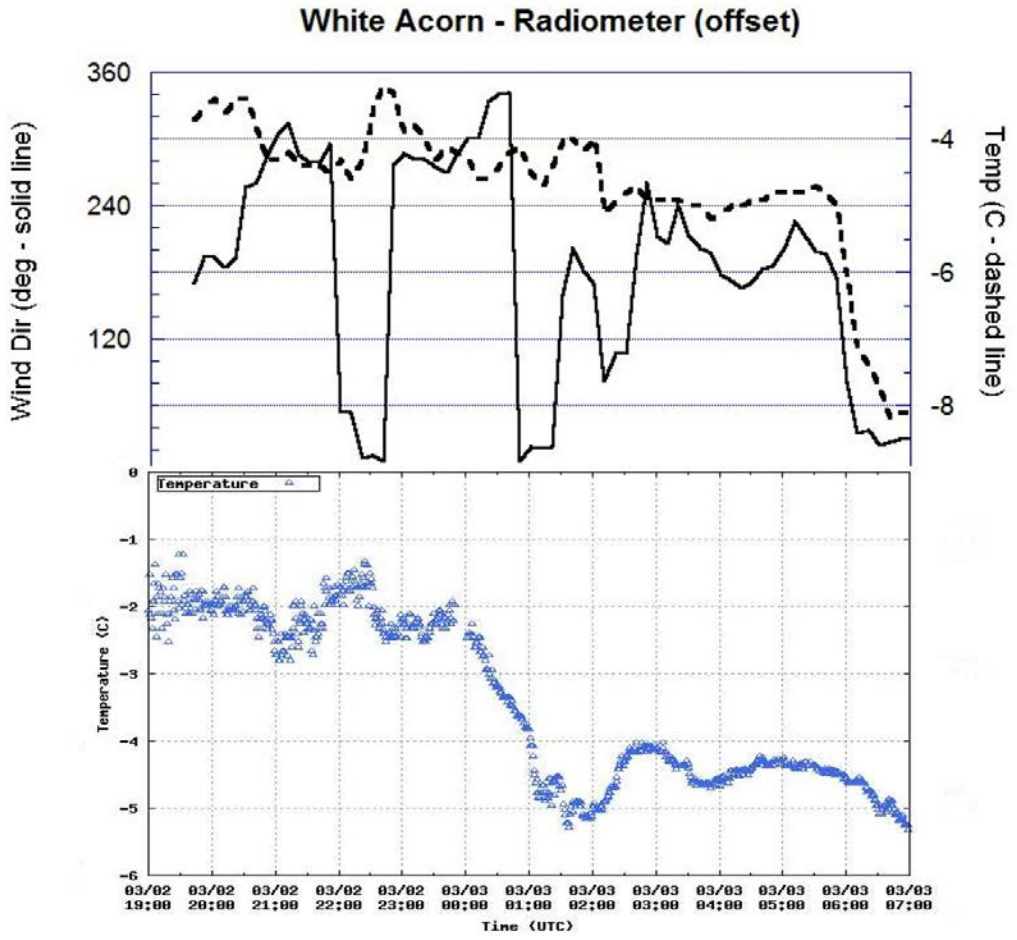

Figure 2.8. 12-hr period of temperature and wind direction (uncorrected) from White Acorn and radiometer sites on 2–3 March 2015. White Acorn data are plotted in black (line – temperature, dashed line – wind direction) and the radiometer temperature is offset below in blue symbols. Time period is 1900 UTC 2 March to 0700 UTC 3 March. The seeding period is 0341–0800 UTC 3 March, the end of the period in the plot.

3. Task 2: Climatology Analyses

The purpose of this task is to determine the characteristics of storms producing precipitation over the Wind River Range and to determine the fraction of time that seedable conditions were present in winter storms impacting the project area, including the fraction of the winter precipitation that could be effectively seeded. The following questions were addressed:

- What are the prevailing winds, temperatures, cloud depths, stabilities, and liquid water content (LWC) during precipitation over the Wind River Range?
- What fraction of the time are ground or airborne seeding conditions present?
- Which months provide the best opportunities for ground or airborne seeding?
- What fraction of the precipitation occurs when ground or airborne seedable conditions are present?

In order to be defined as a "seedable condition", several criteria must be met. First, the temperature needs to be in an appropriate range for nucleation of AgI. Studies have shown that AgI nucleate as warm as −5 °C (DeMott 1997). The criteria utilized in this study define seedable temperatures as between −6 °C and −18 °C.

In addition to an appropriate temperature for AgI to be activated, LWC needs to be present. SLW is a sign that natural precipitation processes are inefficient, and if additional ice crystals are nucleated (via AgI activation) they could grow at the expense of the SLW and fall out as additional snow. Therefore, at a minimum, both appropriate temperature and LWC criteria need to be met to determine seeding potential.

Additional variables, such as stability and winds, play a role in determining seeding potential, with regard to how effectively the AgI will be transported into the cloud where temperature and LWC criteria are suitable for seeding. Therefore, assessing the stability and wind direction is important for determining locations to release AgI and the method of delivery (i.e., ground-based generators or aircraft).

The observations needed to evaluate these environmental criteria include atmospheric soundings (to assess temperature, stability, and winds at heights where clouds form), radiometer data (to assess the presence of liquid water in the atmosphere), and precipitation gauge data (to determine when and how much precipitation fell). With the exception of SNOTEL gauge measurements, these types of observations are quite rare, especially in the western U.S. mountains, and therefore an alternative is to utilize high-resolution model reanalysis data. Not all publicly available model reanalyses include LWC as an output variable (as explained in Ritzman et al. 2015). However, an eight-year high-resolution model simulation from NCAR (Rasmussen et al. 2014) does include all of these necessary variables and was utilized for the majority of this climatological analysis.

3.1. Data and Methodology

3.1.1. Observations

Precipitation climatology in the project area was investigated using SNOTEL observation data and the high-resolution Weather and Research Forecast (WRF) model simulation

described in Section 3.1.2. Data from 15 SNOTEL sites were available for the evaluation period (magenta dots in Figure 3.1).

SNOTEL observations provide a long-term record of precipitation from weighing precipitation gauges and snowpack from snow pillows at numerous sites throughout the Western U.S. These sites are owned and operated by the Department of Agriculture Natural Resource Conservation Service (NRCS), and are typically located at elevations between 2400 and 3600 m MSL. Past and real time data are available from the NRCS web site (http://www.wcc.nrcs.usda.gov/snow/). The data have been widely used in the past for climatological studies. These studies also describe known measurement deficiencies (Serreze et al. 1999; Serreze et al. 2001; and Johnson and Marks 2004; for example) such as an undercatch of snowfall due to wind (Serreze et al. 2001; Yang et al. 1998; Rasmussen et al. 2012). Based on the location of SNOTEL gauges in a forest clearing, most of the time the wind speed is less than 2 m s^{-1}, for which an undercatch of approximately 10 – 15% is expected (Yang et al. 1998). The SNOTEL data resolution is 0.1 inch (2.5 mm). This makes it difficult to study precipitation characteristics or verify model data on sub-daily basis. However, they are suitable for use over monthly or longer periods.

Regular atmospheric sounding data were available twice daily at 0000 and 1200 UTC from the National Weather Service (NWS) office located in Riverton, WY. These data were analyzed to determine the frequency of 700 hPa wind direction when precipitation was observed at the Townsend SNOTEL site in the southeastern portion of the Wind River Range. The wind rose produced from this analysis can be compared with the same from the model-based analysis of winds over the Riverton, WY site.

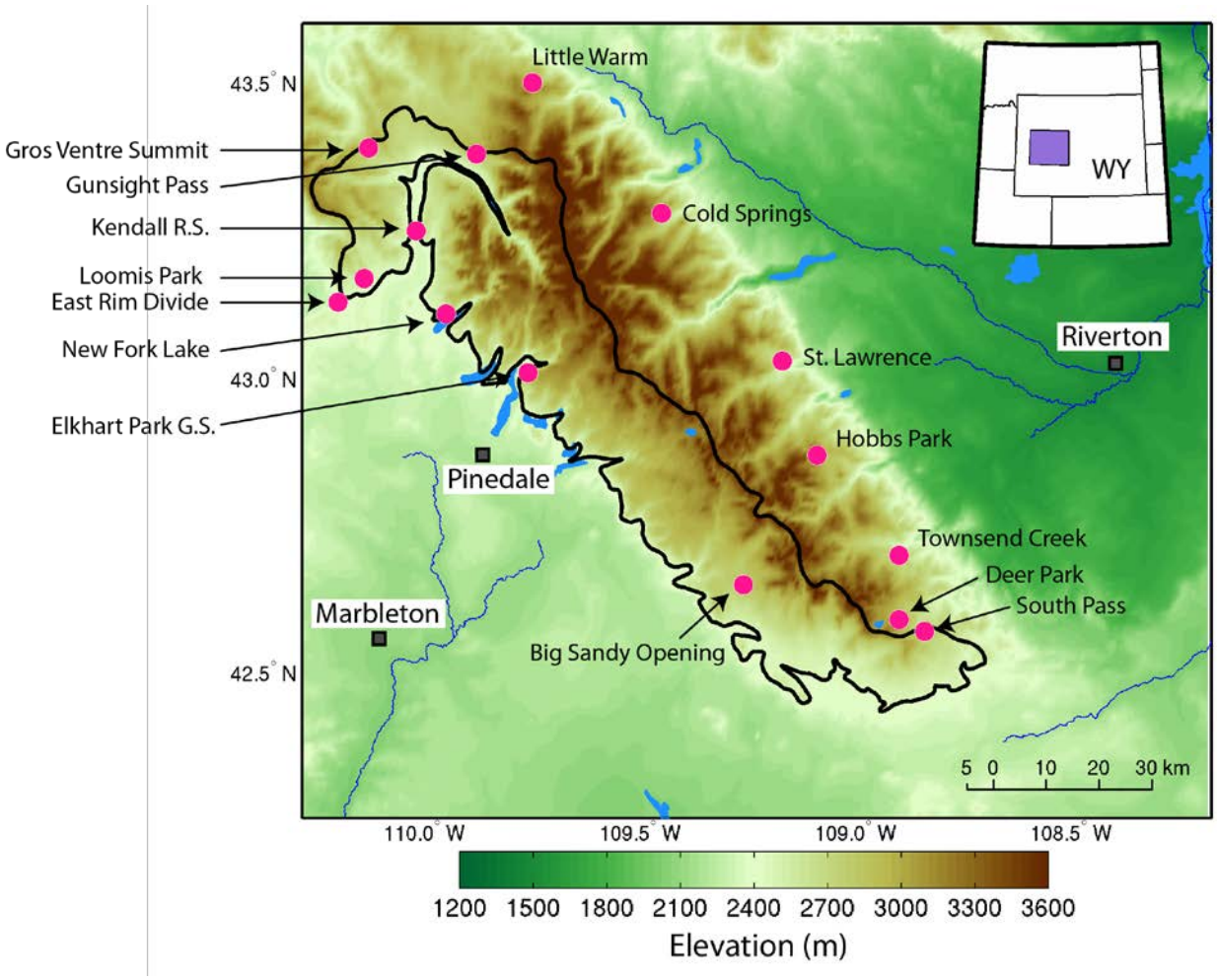

Figure 3.1. Locations of SNOTEL sites (magenta dots). Solid black line encloses the seeding target region. Squares mark near-by towns.

3.1.2. Model

Model data used in this study came from the high-resolution regional climate simulation that was performed by Rasmussen et al. (2011, 2014). The simulation was done using the WRF model (Skamarock et al. 2005) over eight years between 1 October 2000 and 30 September 2008 for the model domain shown in Figure 3.2 with a horizontal grid spacing of 4 km, which includes the Wind River Range. This single model domain covered 1200×1000 km^2 and had 45 vertical levels. The model produces output every hour and was configured with the model physics listed in Table 3.1. Ikeda et al. (2010) and Rasmussen et al. (2014) demonstrated that this model simulation well reproduced observed precipitation both temporally and spatially using SNOTEL data in the Colorado headwaters region of Colorado (see Figure 1 in Rasmussen et al. 2014). The annual precipitation from the model in that study was within 5-10% of the SNOTEL observations. This is the same model simulation that Ritzman et al. (2015) utilized for the WWMPP climatological analysis over the Medicine Bow and Sierra Madre Ranges.

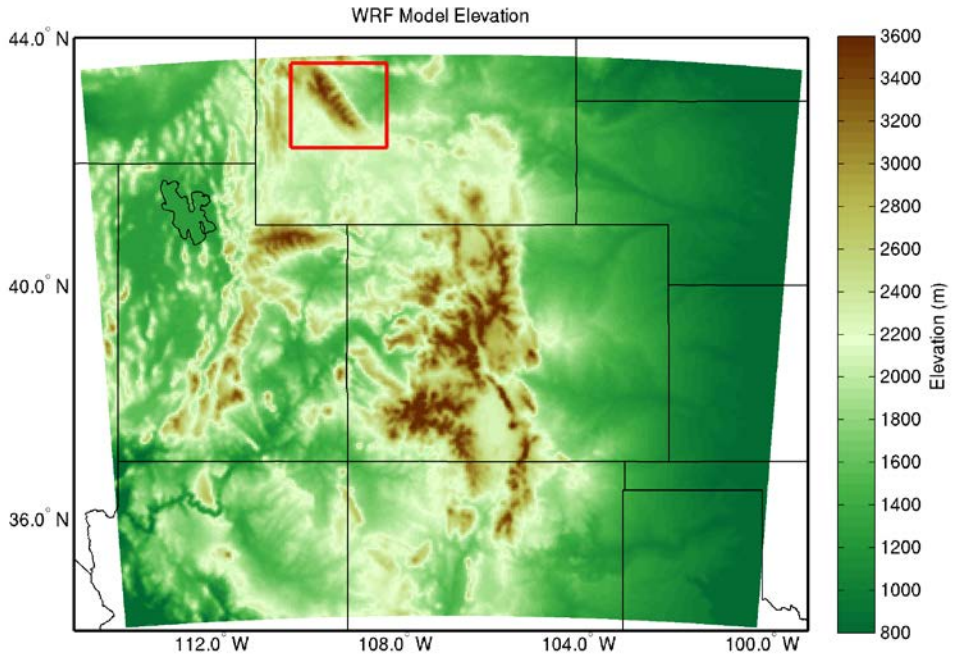

Figure 3.2. WRF model domain and elevation. Red box indicates Wind River Range where the analysis focuses.

Table 3.1. WRF model physics options.

WRF physics	Parameterization schemes	References
Land surface	Noah Land Surface Model, version 3.2, with upgraded snow physics	Chen and Dudhia (2001) Barlage et al. (2010)
Microphysics	Thompson mixed phase	Thompson et al. (2008)
Planetary boundary layer	Yonsei University PBL	Hong et al. (2006)
Longwave and shortwave radiation	Community Atmosphere Model, version 3 (CAM3)	Collins et al. (2006)
Convective parameterization	Betts-Miller-Janjic	Janjic (1994)

To establish a basis for using the model data for this study, the model data were compared to measurements from 15 SNOTEL sites in the Wind River Range (Figure 3.1), which had a continuous record during the model simulation period (see Section 3.1.2). The model data at the SNOTEL sites were obtained by taking the inverse-distance weighted average of the four data points closest to each SNOTEL site.

In addition, the regular atmospheric sounding data from the Riverton NWS office was compared to the model. Comparisons were made for the following variables:

- 700 hPa geopotential height, temperature, dew point temperature, water vapor mixing ratio, wind speed, and wind direction
- Precipitable water up to the 300 hPa level
- Squared of the Brunt-Vaisala frequency (N^2)

The atmospheric quantities at 700 hPa were found by linear interpolation from the forecast and observational data.

Precipitable water (cm) is defined as,

$$PWAT = \frac{1}{g}\frac{1}{\rho_w}\int_{p_1}^{p_2} Qv\, dp$$

,

where g is the gravitational acceleration (980 cm s^{-2}), r_w is the density of water, Qv is water vapor mixing ratio (kg kg^{-1}) at pressure level p, dp the layer thickness in terms of pressure (Pa), p_1 and p_2 are the limits of integration. In this study, the integration was performed between the surface and 300 hPa.

Dynamic stability can be expressed as the square of the Brunt-Vaisala frequency. The atmosphere is unstable when $N^2 < 0$, neutral for $N^2 = 0$, and stable for $N^2 > 0$.

N (s^{-1}) is expressed as,

$$N = \left(\frac{g}{T_v}\frac{\partial \theta_v}{\partial z}\right)^{1/2},$$

where g is the gravitational acceleration (9.8 m s^{-2}), T_v is the layer average virtual temperature (K), and $\partial\theta_v/\partial z$ is the vertical gradient of virtual potential temperature (K m^{-1}) (AMS Glossary). Virtual potential temperature was used to compute N to take into account moist/saturated air. Detailed descriptions of precipitable water and stability terms can be found in the online AMS Glossary[1].

In order to maintain consistency in the comparison of the layer-derived variables (precipitable water and N^2) between the model and sounding observations, the modeled and observed precipitable water and N^2 were excluded from the comparison if the lowest height of the Riverton sounding measurement differed from that of the WRF model by more than 30 hPa (~200 m). Only 17 % of the data over the 8-year period were eliminated by this threshold. (Note that this rule was not applied to the 700-hPa variables.)

Seeding Potential Analysis Methods

Three methods were used to determine the seeding potential of the project area: a single site analysis of 700 hPa conditions, a spatial mapping of seeding potential, and an area-based analysis.

The single site analysis was performed to examine conditions at 700 hPa at individual selected grid points on the west and east slopes of the target range. Since the 700 hPa pressure level intersects the crest of the mountain range, using the 700 hPa data for an

[1] http://glossary.ametsoc.org/wiki/Main_Page

area-based analysis is not possible. Rather, three representative sites were chosen to assess 700 hPa temperature and wind conditions: Pinedale, Wyoming on the west slope and Lander and Riverton on the east slope (Figure 3.3). Riverton was chosen to match the NWS sounding site. The modeled 700 hPa temperature and wind conditions at those single grid points were then assessed during modeled precipitation conditions. For the Pinedale single site analysis, precipitation was determined using the model output at the grid point closest to the Big Sandy SNOTEL site; for Lander and Riverton, the grid point nearest the Townsend SNOTEL site was used (Figure 3.3). While no SNOTEL sites existed on the crest of the Wind River Range to verify the modeled precipitation there, precipitation was also analyzed over a grid point along the crest of the Range (see black Crest point in Figure 3.3) since that is where the maximum precipitation typically occurred in the model simulations.

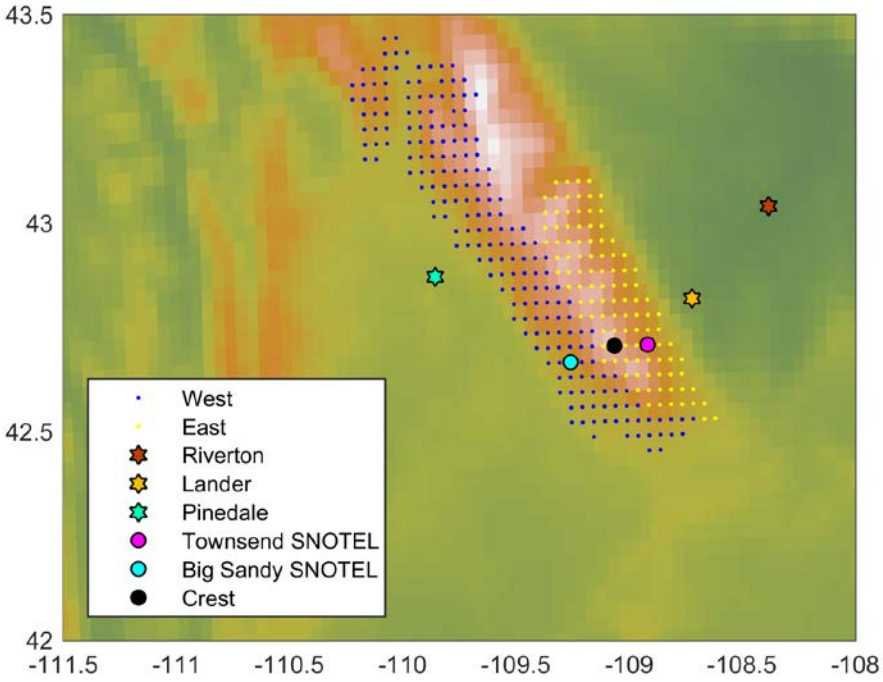

Figure 3.3. Map of the model terrain height highlighting the grid points used in the seeding potential analysis along with other key sites where model output was analyzed. The west area is shown by blue dots. The representative west precipitation site is the Big Sandy SNOTEL site (cyan circle). The east area is shown by red dots, with the representative east precipitation site the Townsend SNOTEL site (magenta circle). The "crest" precipitation site is the black circle. The Riverton (east slope), Lander (east slope), and Pinedale (west slope) sites are shown by red, orange, and green stars, respectively.

For the spatial mapping and area-based analyses, ground-based seeding potential was analyzed separately from airborne seeding potential using the vertical layer of the atmosphere under study. For ground-based seeding, the 0–1 km Above Ground Level (AGL) layer was investigated and each criterion assessed was averaged over that layer at every model grid point (4 km spacing) and output time (hourly). For airborne seeding potential, the 4–5 km MSL and the 4.75–5.85 km MSL layers were assessed by averaging each criterion over that vertical layer as was done for the ground-seeding layer.

Key criteria produced by the model output and utilized by this analysis were: temperature, LWP (defined as column integrated cloud water per unit area), LWC mixing ratio, horizontal components of wind velocity (U and V) and derived turbulence parameters (e.g., square of Brunt-*Väisälä* frequency, Froude number, and Bulk Richardson number). Of these, the primary criterion used to indicate the presence of a cloud seeding opportunity was the presence of liquid water at temperatures appropriate for AgI activation. This leads to the following criteria for assessing whether cloud seeding is viable in a region:

- Temperature (−6°C > T > −18°C)
- Liquid water path (LWP > 0.01 mm)
- Liquid water content (LWC > 0.01 g kg^{-1})

The LWP criterion resembles information that would be available to an operational forecaster using a radiometer. In contrast, the LWC criterion identifies the vertical location of liquid water and thus can be used to discriminate ground from airborne seeding opportunities.

Meeting the above criteria indicates the potential for cloud seeding. This potential can only be realized, however, if the seeding material reaches those regions. This leads to an additional set of criteria to be met:

- Wind direction
    - For west slope cases, between 180 and 290 degrees on the west side of the Range
    - For east slope cases, between 20 and 100 degrees on the east side of the Range
- Froude number > 0.5

The wind direction criterion was based on the preliminary design of the ground-based seeding program after determining the dominant wind regimes affecting the target region. These additional criteria were not required for airborne seeding potential, given that an aircraft can introduce AgI directly into the atmosphere where seeding conditions occur and the flight track can be oriented to account for wind direction.

Spatial maps were produced by utilizing the hourly model output and mapping the frequency of hours in a given time period, such as monthly or seasonally, that the primary criteria were met at each grid point. This produced maps of the frequency of seedability at each grid point for each month and each season starting November 2000 and ending April 2008.

For the area-based analysis, western (blue dots in Figure 3.3) and eastern (red dots in Figure 3.3) regions were defined. In each region, areal-averaged values for each criterion (for either ground or airborne seeding layers) were produced at every model output time (hourly). The same microphysical conditions assessed in the spatial mapping analysis (i.e., temperature and liquid water content in particular) were assessed over these regions by producing histograms of the areal-averaged values. Additionally, the frequency of time (a given month or winter season) that the areal-averaged conditions met the thresholds defined above was determined. In order to normalize the results by when precipitation occurred, a representative SNOTEL site for the given region that also had a good

comparison with the model (based upon the SNOTEL model evaluation, see Section 3.2.2) was chosen for each region. The model grid point nearest that SNOTEL site was used to determine if precipitation occurred in that region or not.

Stability indices were also derived from the model output and analyzed to evaluate its impact on ground-based seeding potential. The primary index analyzed was the Froude number (Fr). The Froude number expresses the ability of upslope airflow to go over a mountain barrier. The flow will typically be blocked by the barrier when Fr < 0.5. The flow will freely move over the barrier (unblocked) when Fr > 1. Froude number is computed from

$$Fr = \frac{U/h}{N},$$

where U is the average wind speed (m s^{-1}) perpendicular to the mountain barrier orientation over a depth of h (in m), and N is an average of the Brunt-Väisälä frequency between the same depth. In this case, h is assumed to be 1000 m. N (s^{-1}) is expressed as

$$N = \left(\frac{g}{T_v} \frac{\partial \theta_v}{\partial z} \right)^{1/2},$$

where g is the gravitational acceleration (9.8 m s^{-2}), T_v is the layer average virtual temperature (K), and $\partial \theta_v / \partial z$ is the vertical gradient of virtual potential temperature (K m^{-1}).

3.2. Characteristics of Wintertime Clouds and Precipitation

3.2.1. SNOTEL Precipitation Observations

The monthly averaged precipitation over the 15 SNOTEL sites are shown in Figure 3.4 for: a) each water year (panels a–h) and b) an eight-year average (panel i). The annual cycle of precipitation varies significantly over the eight-year period; the peak precipitation can occur in early winter or late winter/early spring depending on the year. In some years, warm season precipitation exceeds winter precipitation. For these eight years, the SNOTEL data showed that the November–April precipitation brings about a half or a little more of the annual precipitation to the Wind River Range region (Table 3.2). The November–April precipitation is quite uniformly distributed between the SNOTEL sites as shown in Figure 3.5. Out of the 15 sites, the two southernmost sites (Deer Park and South Pass), whose site elevation is relatively higher than others, had the most seasonal precipitation. It is difficult to assess the full picture of precipitation distribution without observational data at higher elevations on the Range, but the model data (described in Section 3.2.2) shows that the precipitation is 20 to 100% higher at the crest as compared to the locations of the SNOTEL sites. Confirmation of this result would require deployment of additional snow gauges along the crest line.

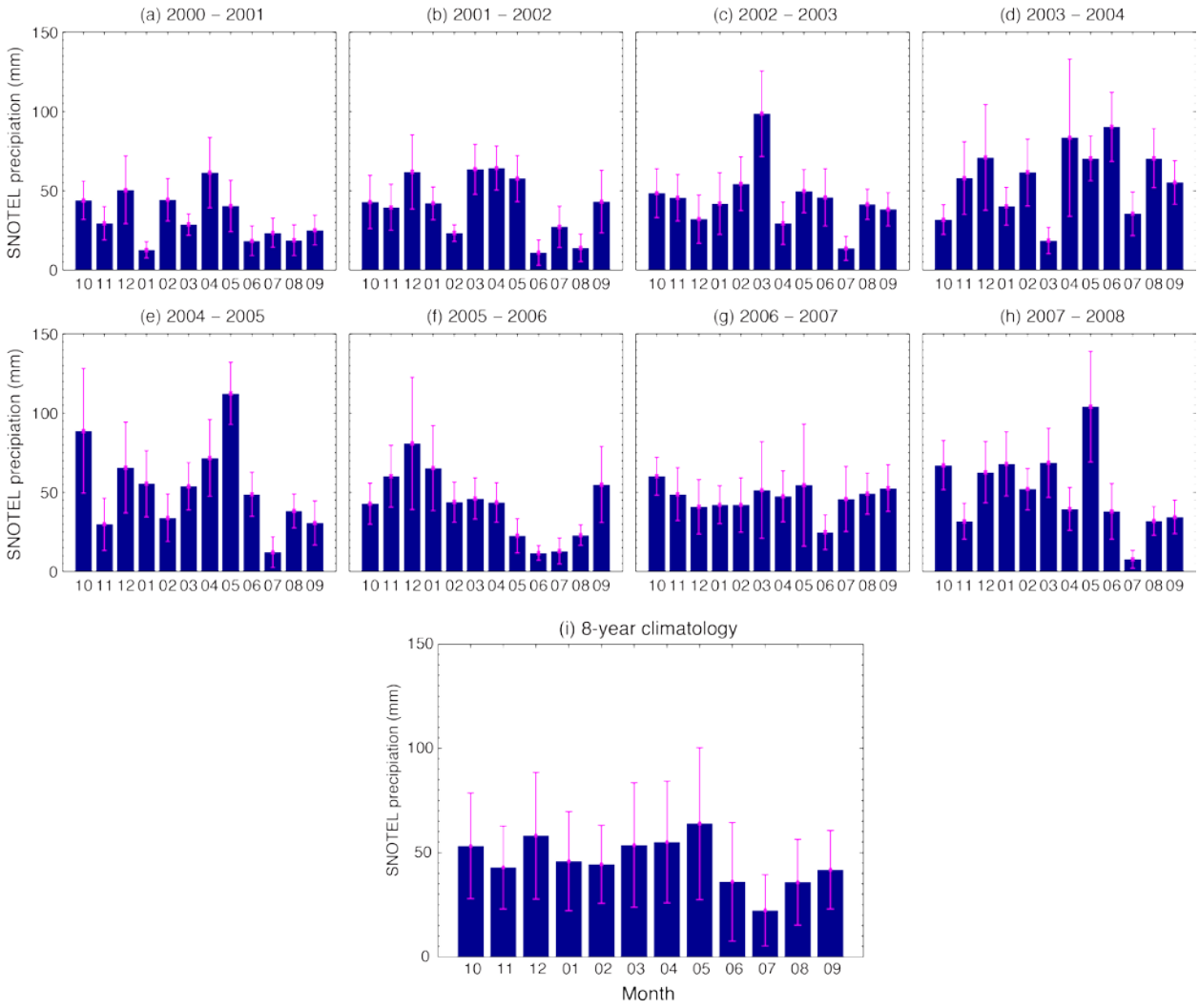

Figure 3.4. (a) – (h) Monthly precipitation averaged over 15 SNOTEL sites for each of the eight water years. (i) Eight-year climatology of monthly precipitation at the 15 SNOTEL sites. Vertical bars indicate one standard deviation from the mean.

Table 3.2. Average annual precipitation from 15 SNOTEL sites and the fraction of the annual precipitation that fell between 1 November and 30 April in each water year.

Water year	Annual precipitation (mm)	Fraction of November–April precipitation (%)
2000–2001	396.1	57
2001–2002	489.5	60
2002–2003	538.3	56
2003–2004	685.6	48
2004–2005	640.8	48
2005–2006	507.2	67
2006–2007	559.1	49
2007–2008	605.2	53

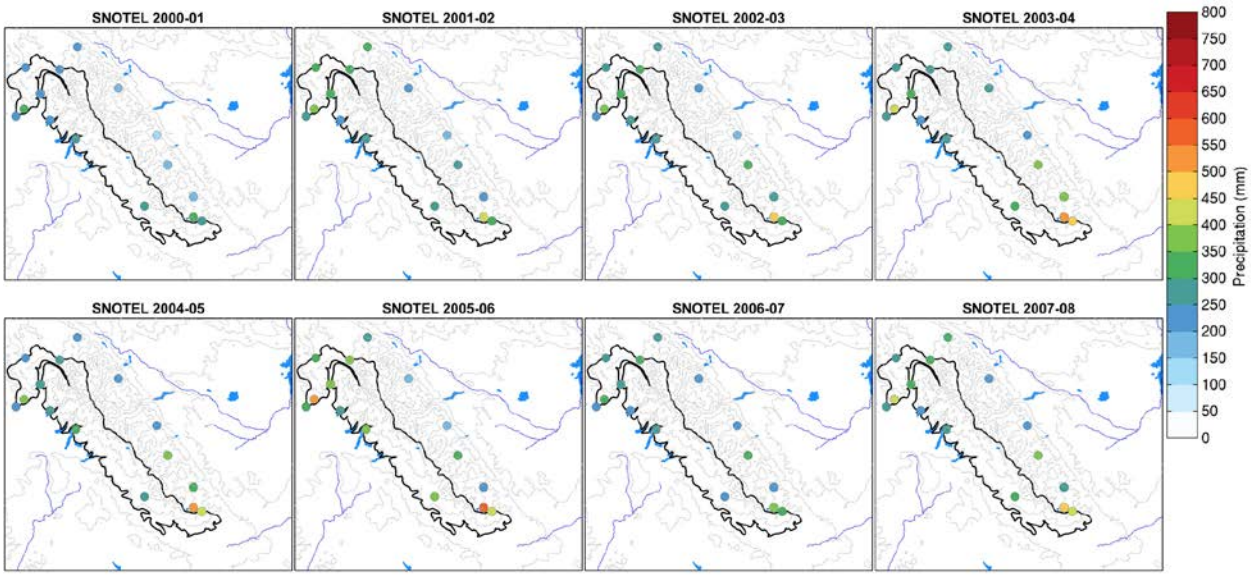

Figure 3.5. The November–April precipitation at SNOTEL sites in each water year.

To investigate winter precipitation patterns on the western and eastern slopes of the Wind River Range, daily SNOTEL precipitation from 1 November to 30 April were examined. Figure 3.6 shows the correlation coefficients of the eight-year climatology of daily precipitation at each pair of SNOTEL sites. Those from individual water years are shown in Figure 3.7. In both figures, bright colors indicate high correlation in daily precipitation between a given pair of sites.

A clear pattern emerges from the two figures; high correlations are found between nearby sites that are on the same side of the Wind River Range. On the other hand, sites on the opposite sides of the Range show weaker correlations. This suggests that precipitation

from dominant westerly winter storms are not carried much beyond the high peaks of the Range. An exception to this pattern is the high correlation between sites at the southern end of the Range: Big Sandy Opening (west) and South Pass (east) and Deer Park (east). This is likely related to dominant wind patterns over this region associated with westerly/southwesterly weather systems. Another notable location is the northern most site (on the eastern slope), Little Warm. Little Warm's correlation coefficients with any particular site tended to be moderate at best. This is could be because the site is blocked by higher terrain to its north, west, and south, or just due to the fact that this site is more isolated from the other sites. Note that the weaker correlation coefficients for the 2000–2001 season compared to other seasons is simply because it was relatively dry that year (i.e., small dynamic range of daily precipitation).

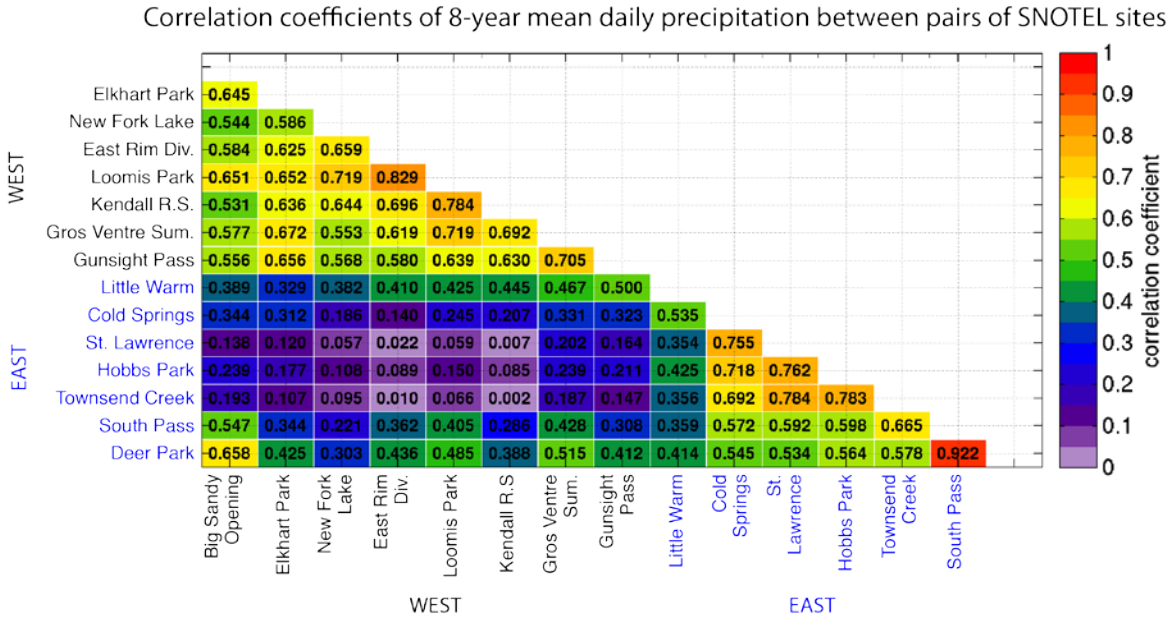

Figure 3.6. Correlation coefficients of 8-year average daily precipitation at each pair of SNOTEL sites. SNOTEL site names in black (blue) are the sites on the western (eastern) slopes of the Wind River Range.

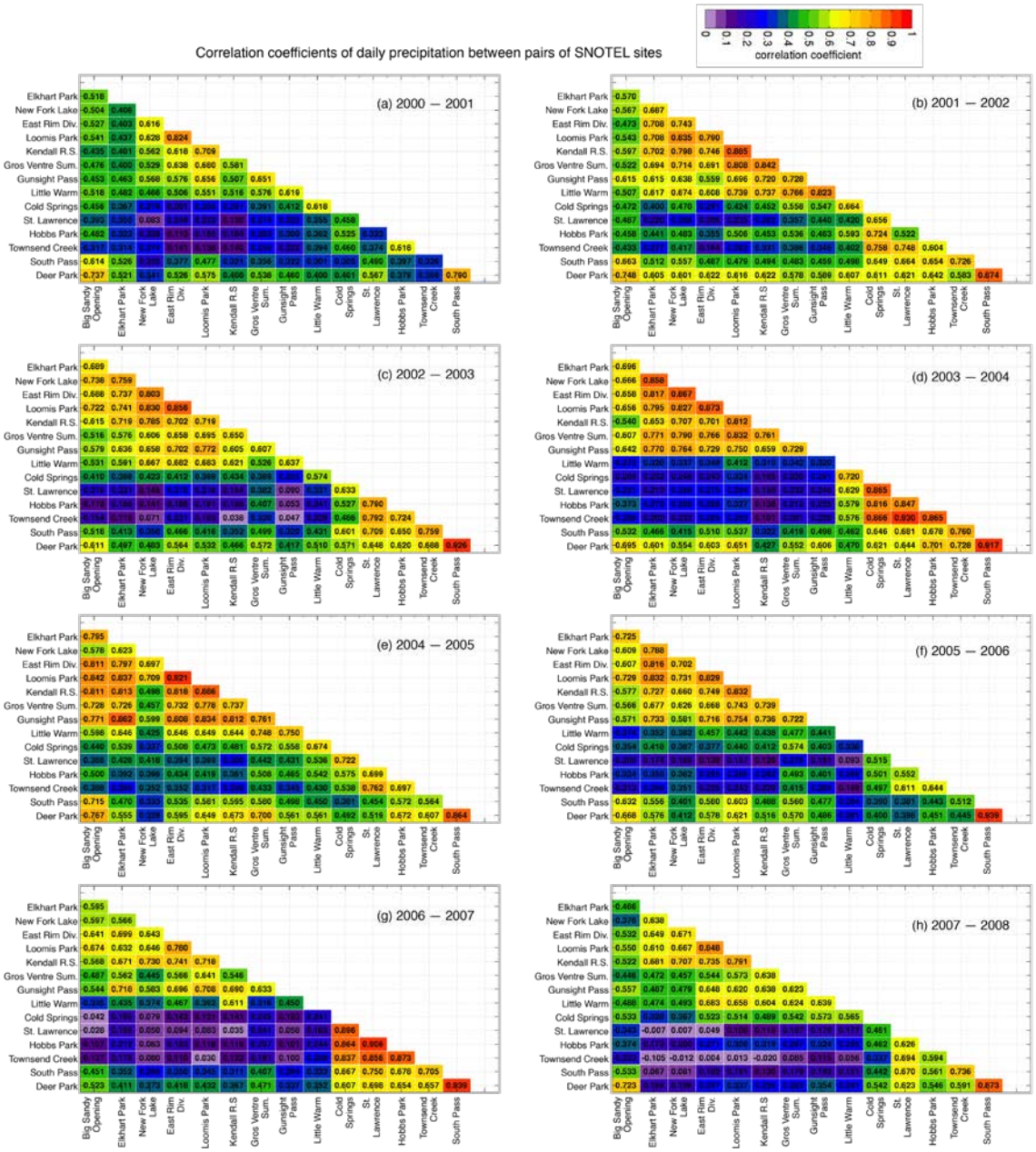

Figure 3.7. Same as Figure 3.6 but for each water year.

3.2.2. Comparison of model versus SNOTEL

Figure 3.8 shows the spatial distribution of the November–April precipitation from the WRF model 8-year regional climate simulation (recall Section 3.1.2). When compared with Figure 3.5, the WRF model's precipitation is similar to that observed (although there are no sites to verify the modeled precipitation maximum in the highest elevations).

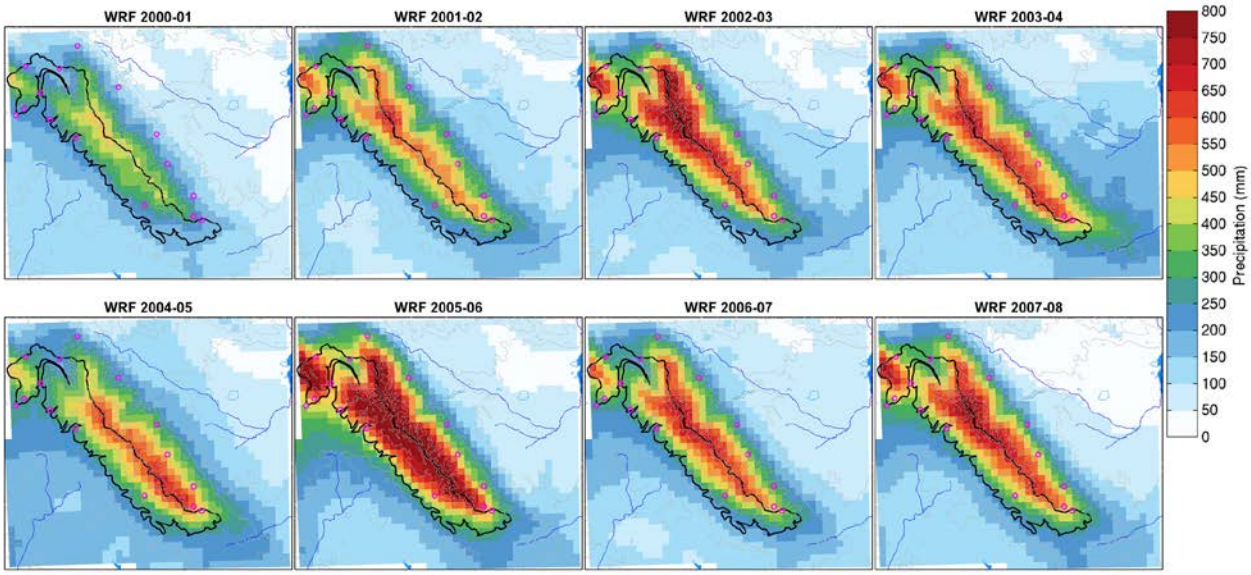

Figure 3.8. The November–April precipitation in each water year from the WRF model. Magenta circles indicate the SNOTEL site locations.

Figure 3.9 presents the eight-year climatology of precipitation accumulation at individual SNOTEL sites using both SNOTEL and the WRF model data. The agreement at Loomis Park, Little Warm, Deer Park, and South Pass are impressive. At other sites there is a tendency for the model to overestimate precipitation, except at Gunsight Pass where the model underestimated the observed precipitation. The model bias in the November – April precipitation is mostly ~30 % or less with an exception of a couple of sites. On the western slopes of the Wind River Range, the model tends to be too aggressive at New Fork Lake (seasonal bias of ~40%), Kendall R. S., and Gros Ventre Summit. On the eastern slopes, the model has a relatively higher bias at St. Lawrence Alt. (seasonal bias of ~40%) and Hobbs Park. Regardless, the WRF model captured the observations fairly well given the uncertainties in the snowfall measurements and the 4-km grid spacing of the WRF model not being able to resolve finer underlying terrain effects. The precipitation accumulation comparison at each site for each individual water year indicated that each storm event over the 8-year period was simulated (not shown). In general, discrepancies between the observations and model occurred from the model not correctly reproducing the amount from a couple of large snowstorms rather than missing an entire precipitation event. The model over-estimated precipitation in ten out the fifteen sites by ~10-20%, consistent with the estimated SNOTEL undercatch due to wind.

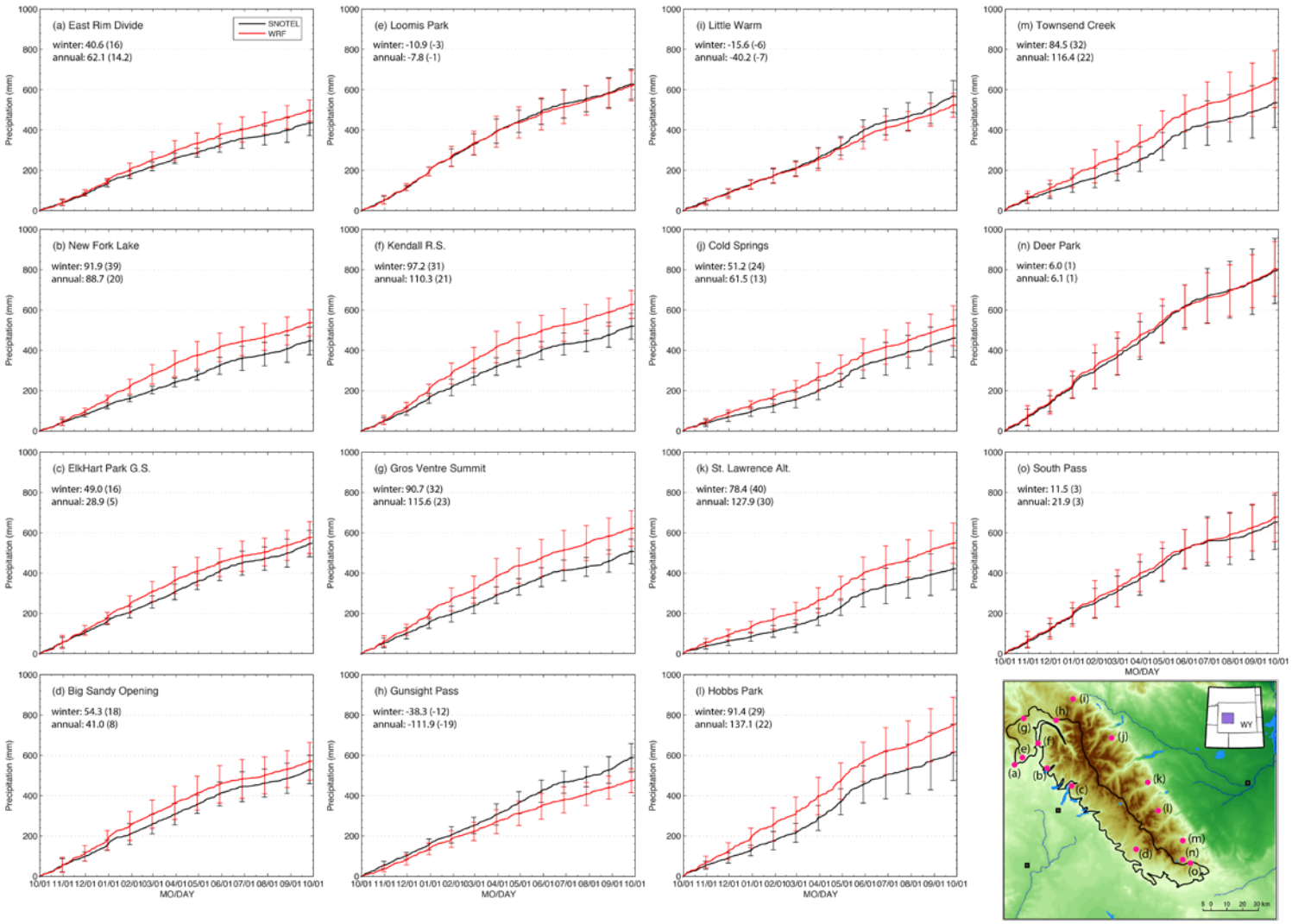

Figure 3.9. Eight-year climatology of annual precipitation accumulation at each SNOTEL site. Vertical bars are one standard deviation about the 8-year mean. Eight-year average seasonal (1 November–30 April) and annual precipitation biases are annotated (model minus observation in mm). Values in parentheses are the percent bias in the seasonal and annual biases. Refer to the map (lower right panel) for the SNOTEL site location.

Figure 3.10 presents the annual precipitation accumulation comparison averaged over the 15 SNOTEL sites in each water year. There is a good agreement between the observations and model in most years. The ability of the model to capture observed precipitation events is also illustrated in this figure. The standard deviations of the annual SNOTEL and model data are similar, indicating that the year-to-year variability is also well represented by the model. The model bias in the seasonal precipitation is ~20 % or less. Considering that SNOTEL data are typically underestimating the actual precipitation by 10–15% due to wind effects, the comparison is remarkable.

The exception to the generally excellent agreement occurred for the 2005–2006 simulation. For this particular water year, the model overestimated the observed seasonal precipitation by ~30 %. The model bias at the above-mentioned sites (e.g., New Fork Lake and Gros Ventre Summit) was notably large for a couple of early winter large snowstorms and storms in March and thus affected the results. There was no notable pattern in monthly precipitation bias (Figure 3.11), which is not surprising, given the interannual variability seen from Figure 3.4. Over the 8-year period, the model precipitation over the November–April and annual periods were 15 and 9 % more than the observed amount (Figure 3.12).

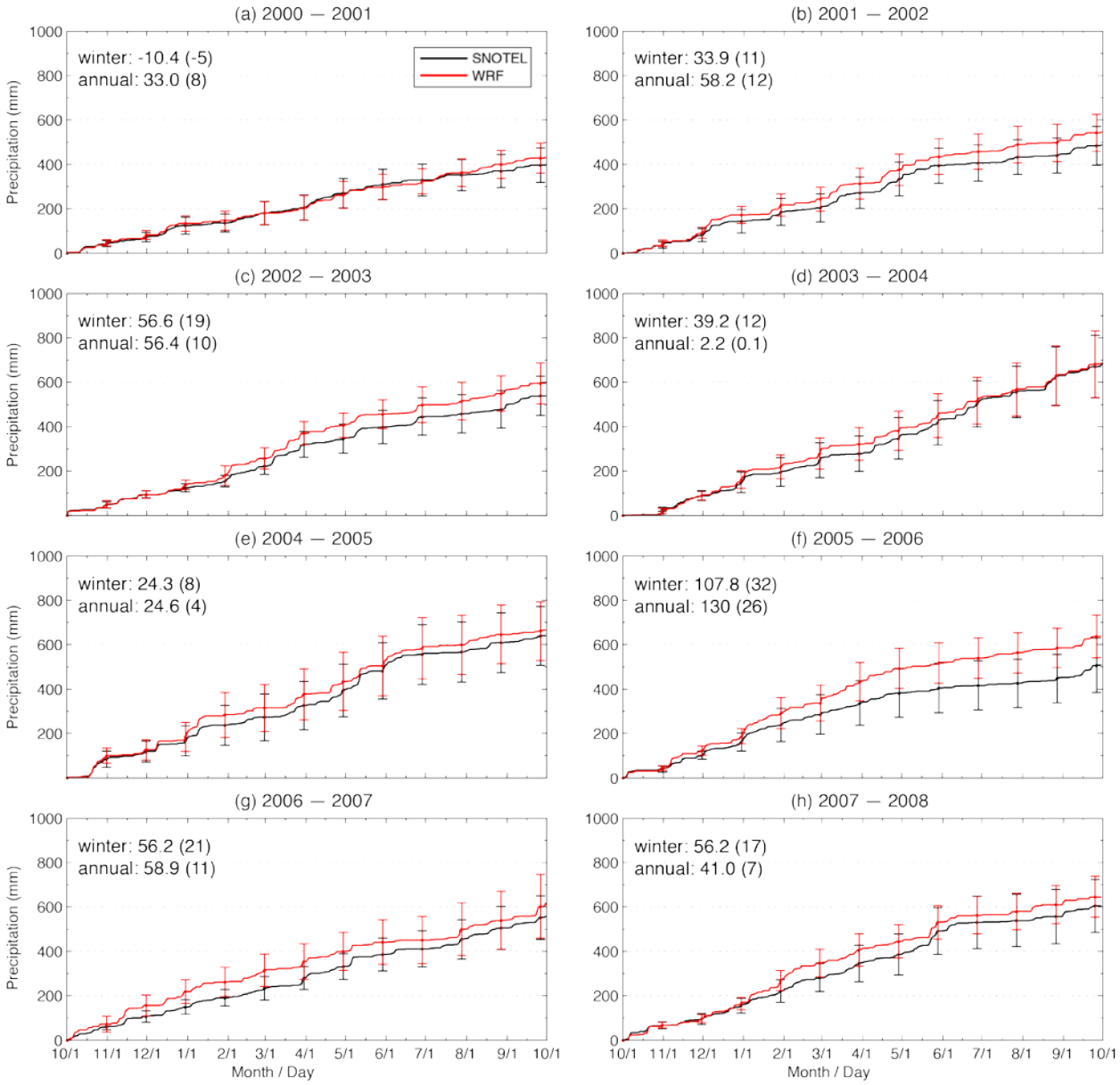

Figure 3.10. Time history of observed and simulated precipitation accumulation averaged over 15 SNOTEL sites from each water year. The model bias in the November–April (winter) and annual precipitation totals (in mm) is indicated in the upper left corners. Values in parentheses are the percent bias from the observations. The biases are taken as model minus observation.

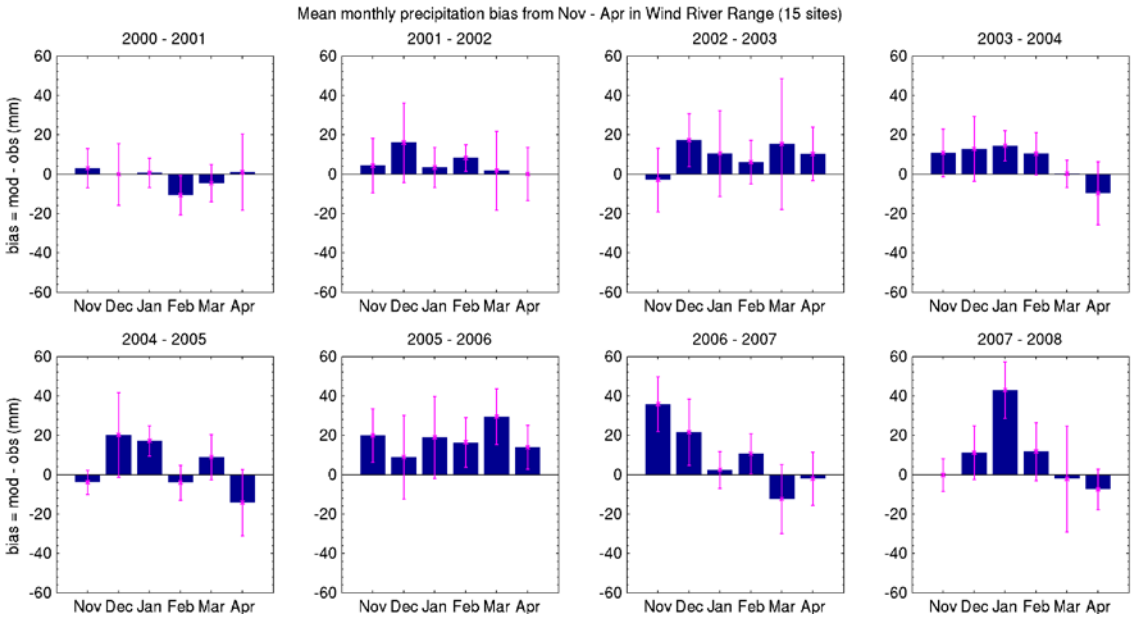

Figure 3.11: Mean monthly bias in model precipitation at 15 SNOTEL sites for each winter season. The error bars represent site-to-site variability in the model bias.

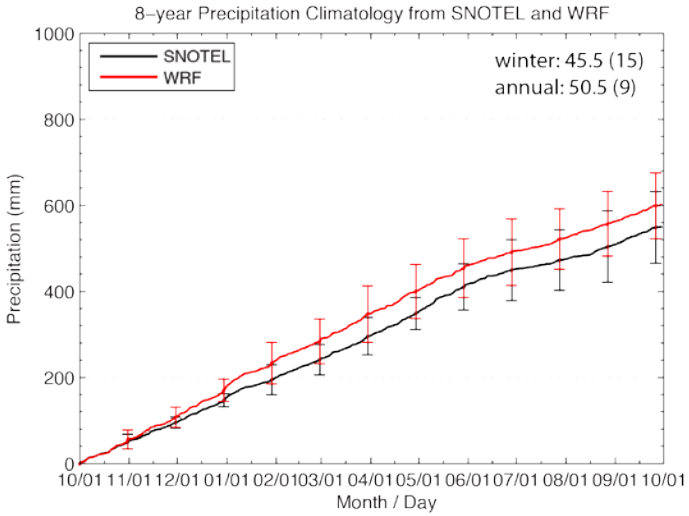

Figure 3.12. An 8-year climatology of precipitation accumulation averaged over 15 SNOTEL sites. Vertical bars are one standard deviation from the 8-year mean, representing the year-to-year variability. The model bias in the November–April (winter) and annual precipitation totals (in mm) is indicated in the upper right corner. Values in parentheses are the percent bias from the observations. The biases are taken as model minus observation.

3.2.1. Comparison of model versus Riverton soundings

In this section, the atmospheric conditions represented by the WRF model eight-year regional climate simulation are examined using the routine NWS upper-air sounding data from Riverton, Wyoming. The model and observations at 00 and 12 UTC from all seasons (not limited to April–November) were included in this evaluation. In practice, soundings are released about 1 hour before the official time. However, we did not take this into

account in this study. In addition, model values were taken from the average of the four grid cells closest to the Riverton sounding site and did not follow the exact balloon location, which drifts with wind. It is important to keep in mind these two factors as well as measurement uncertainties while interpreting the comparison results. In particular, the accuracy of humidity measurements decreases in cold and dry conditions, particularly in temperatures below –20°C (Wang et al. 2002). The measurement uncertainties depend on instrument type but Poore et al. (1995) have reported 0.2°C and 3.5 % for dry-bulb temperature and humidity, respectively, for temperatures warmer than –20°C, but humidity uncertainty becomes ~10 % or greater at colder temperatures based on the twice-daily routine global rawinsonde observations. This yields a dew point temperature uncertainty of 1–3°C.

Figure 3.13 shows scatter plots of observed versus model-simulated 700 hPa height, temperature, and dew point temperature from December–February (DJF), March–May (MAM), June–August (JJA), and September–November (SON). In general, the correlation coefficient for the 700 hPa height is high, although there is a low bias when observations indicate high heights. The agreement between the model and observations for the 700 hPa (dry-bulb) temperature is impressive and show very little bias, if any (mean error of < 0.8°C). There is more scatter in dew point temperature, and the correlation coefficient is lower than it is for the dry-bulb temperature. In all seasons, the slope of the best-fit line is less than the one-to-one line, and there is a warm bias in low dew point temperatures. A part of the discrepancy may be attributed to the measurement uncertainty in humidity as previously mentioned. However, because the model bias in cold temperatures is much larger than the known measurement uncertainty, the result suggests more moist conditions in the model than observed.

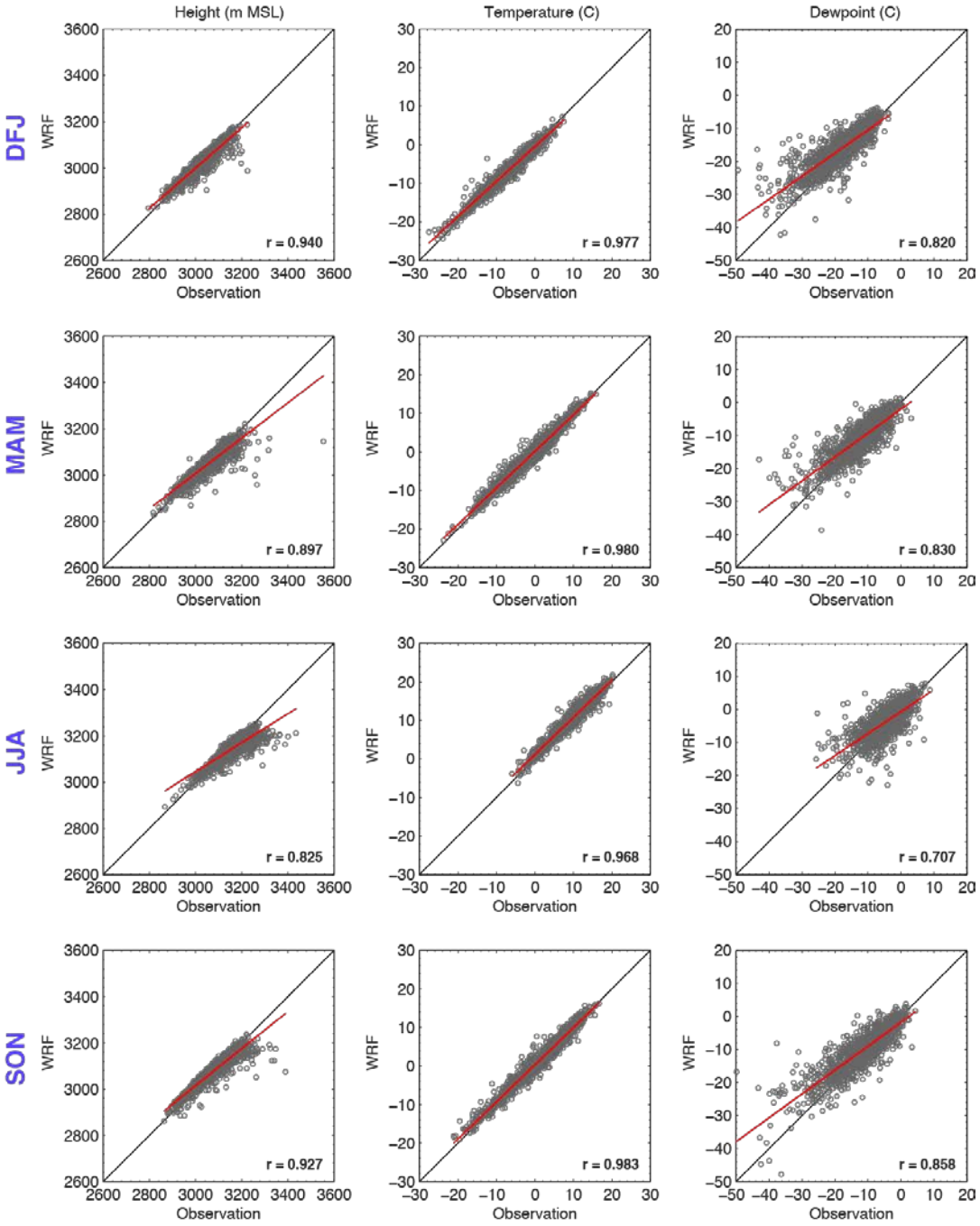

Figure 3.13. Scatter plots of observed and model-simulated 700 hPa geopotential height (m MSL, left column), temperature (°C, middle column), and dew point temperature (°C, right column) for December – January (DJF, top row), March – May (MAM, 2nd row), June – August (JJA, 3rd row), and September – November (SON, bottom row). *r* is the correlation coefficient. Red lines are the least-squared fit through the data points.

The agreement in the 700 hPa mixing ratio (Figure 3.14, left column) between the two datasets is good. However, there is a slight positive bias, especially at lower mixing ratios, which is not easily seen from the scatter plot. (Note that some outliers in MAM, JJA, and SON influenced the least-squared fit line. The slope of the best-fit lines would have been

closer to the one-to-one line without the outliers.) The mean error is small (< 0.4 g kg^{-1}) in all seasons, but the small positive bias at lower mixing ratios, which indicates the model is more moist than observations, agrees with the warm bias at colder dew point temperatures (recall Figure 3.13). Consistently, precipitable water shows a moist bias in all seasons, which almost seems systematic and could be related to the 700 hPa dew point and mixing ratio biases noted above. The mean bias was 0.25 cm or less. For both mixing ratio and precipitable water, the correlation coefficient is high in general.

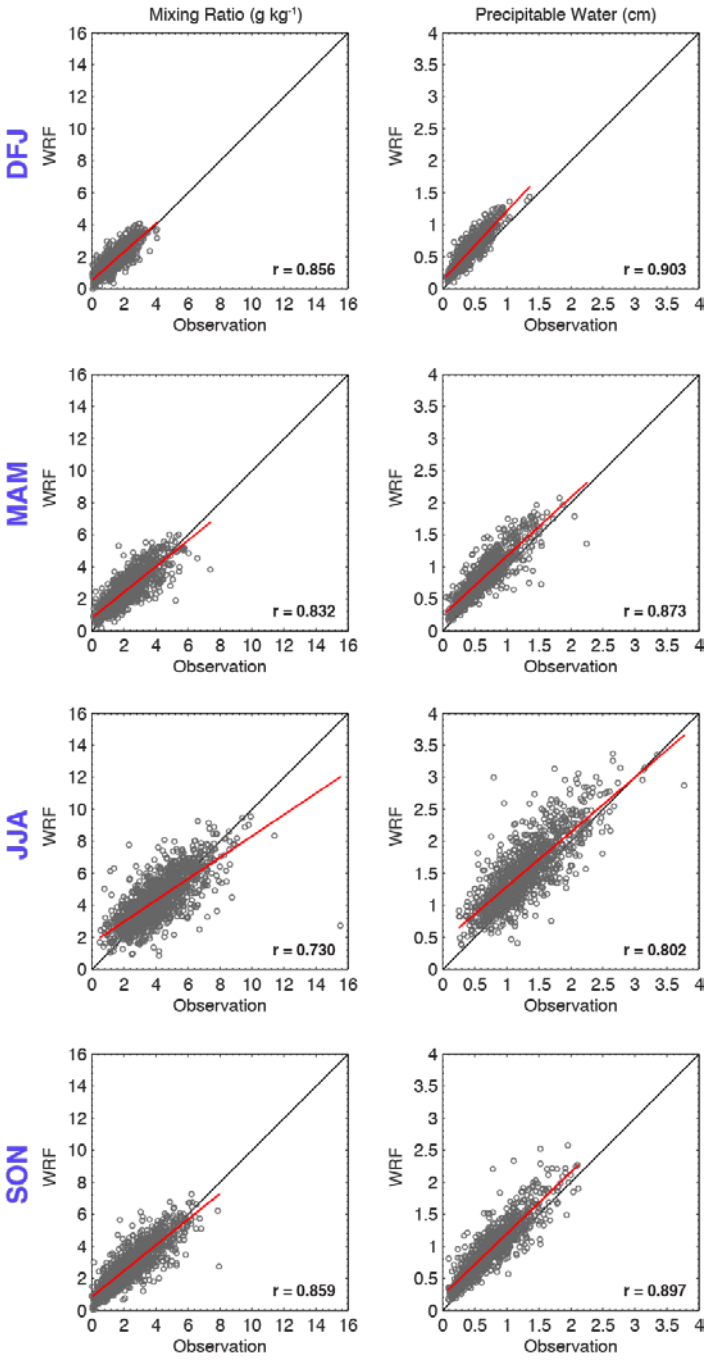

Figure 3.14. As in Figure 3.13 but for the 700 hPa mixing ratio (g kg^{-1}) and precipitable water (mm).

The correlation coefficients for wind speed are ~0.68–0.75 and the best-fit lines are nearly in line with the one-to-one line, showing fair agreement between the two datasets. Some of the scatter in the paired points may be partly attributed to the location difference between the rawinsonde at the 700 hPa level and the launch location, from where the model data points were taken. The mean bias in wind speed was 1.6 m s^{-1} or less and the mean absolute bias was less than ~3 m s^{-1}. The statistical values indicate overall good

performance by the model, but the scatter plots reveal that the model has a tendency to over predict wind speed, especially strong wind in winter to early spring during which large synoptic scale storms are frequent in the study area.

Although the locational difference of the rawinsonde between the release site and the 700 hPa level could have played a role in the wind direction comparison, most of the data points in the wind direction scatter plots lie close to the one-to-one line. The mean error in wind direction was 6–12 degrees and the mean absolute error was 30–45 degrees. The least-squared fit and the mean error suggests that the direction of wind is rotated slightly more toward westerly winds in the model. We will present later that similar wind speed and direction tendencies from the WRF 2014–2015 real-time model data were detected when those data were compared to Pinedale sounding observations (Section 4.3.1). The current results raise a speculation that the precipitation bias with respect to SNOTEL observations (discussed in Section 3.2.2) may be related to the model's slightly wet bias, tendency to have stronger wind, and/or slightly different wind direction.

Stability measured with N^2 shows a fairly good match between the observations and model. Because it is a function of virtual temperature and gradient of virtual potential temperature, the scatter is attributed to the moisture bias we have seen in Figure 3.14.

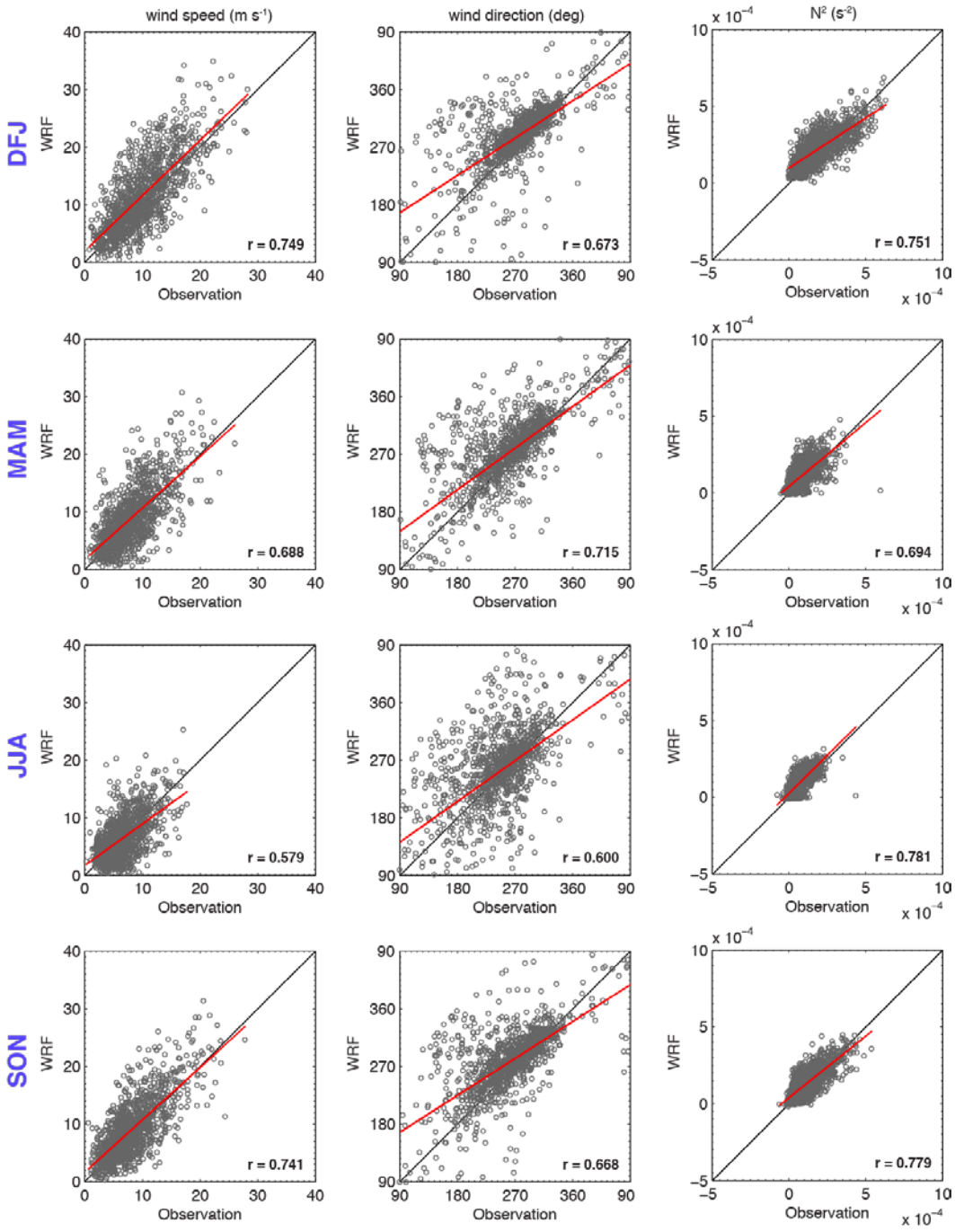

Figure 3.15. As in Figure 3.13 but showing 700 hPa wind speed (m s^{-1}), 700 hPa wind direction (degrees), and the squared of Brunt-Vaisala frequency (N^2, s^{-2}).

3.2.2. Riverton Sounding Analysis

A single site analysis was performed using 8 years of observational data from NWS soundings at Riverton and observed daily precipitation data from the Townsend SNOTEL

site matching the time period of the model analysis (see below). This analysis shows that the observed predominant 700 hPa wind direction was northwesterly and westerly on days when precipitation occurred at Townsend (Figure 3.16a). Additionally, the observed 700 hPa temperature conditions at Riverton ranged from 8°C to −22°C for the winter season and 2°C to −18°C for precipitating events (Figure 3.17a). Around 45% of wintertime hours were colder than −6°C, increasing to roughly 55% for hours with precipitation.

The model-based Riverton wind rose is similar to that from the observations (Figure 3.16), showing that westerly and west-northwesterly winds are dominant when precipitation occurs at the Townsend SNOTEL. The model-based wind rose does not show as strong of a northwesterly regime as the observations however. These model results of temperature distribution at Riverton compare nearly identically with that observed by the NWS sounding at Riverton, except that there is a slight shift of hours with precipitation to colder temperatures, such that 60% of the hours with precipitation were colder than −6°C in the model (compared to roughly 55% in the observations; Figure 3.17).

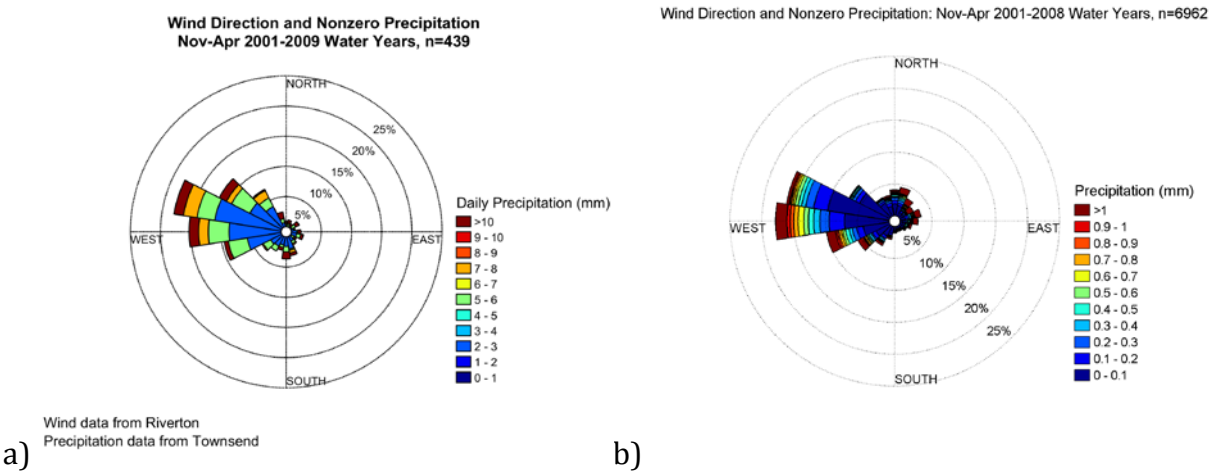

Figure 3.16. Wind rose showing the frequency of a) observed and b) modeled 700 hPa wind direction over Riverton, Wyoming when precipitation occurred over the Wind River Range, using *daily* observed data from the Townsend SNOTEL site in (a) and hourly modeled precipitation at Townsend in (b), over the 8-year period from November–April. The magnitude of *daily* observed or hourly modeled precipitation for each wind direction is indicated by the color within each wind direction bin.

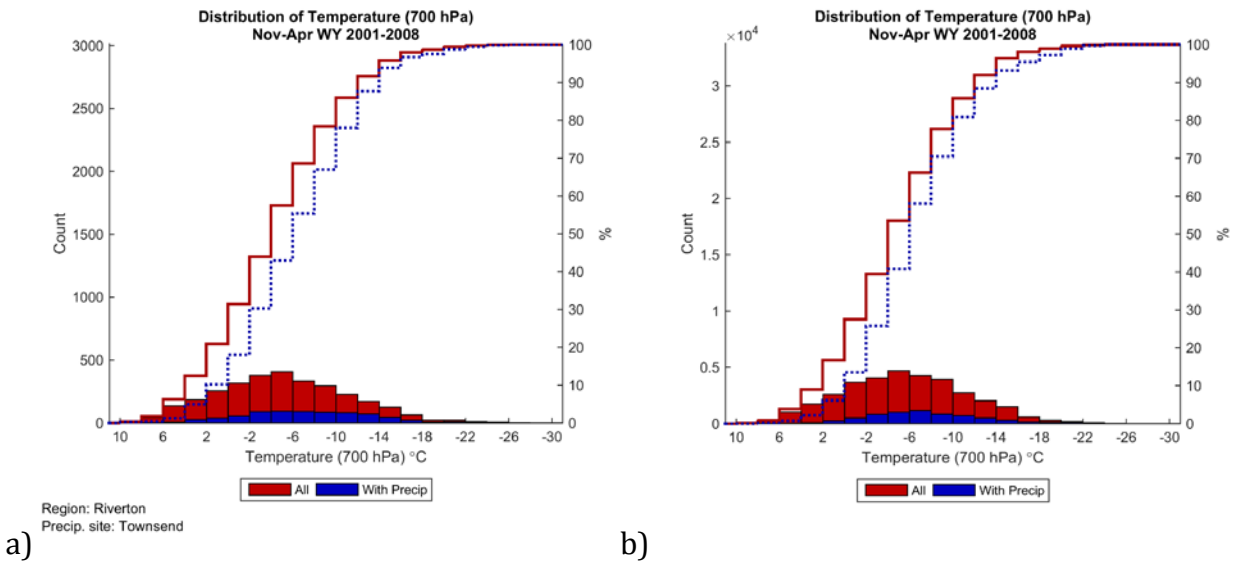

Figure 3.17. Histogram counts (left ordinate) of the a) observed and b) modeled 700 hPa temperature at Riverton, Wyoming for all soundings (red) from November–April from the 8-year period of study (water years 2001–2008) and for all soundings that had precipitation observed at the Townsend SNOTEL site (blue). Cumulative distributions for all (red) and with precipitation (blue dotted) are also overlaid using the right ordinate (%).

3.2.3. Model-based Analysis Results

Single Site Analysis

Single site analysis for Pinedale, Lander, and Riverton shows that the predominant 700 hPa wind direction when precipitation occurs is westerly (Figure 3.18–Figure 3.19, Figure 3.16b). The 700 hPa winds over Pinedale are most frequently northwesterly, then due westerly, followed by some precipitation events that are southwesterly and north-northwesterly (Figure 3.18). There are negligible events over the Wind River Range with any easterly component of the wind over Pinedale. The Lander and Riverton sites, on the east slope, have a more due-westerly dominance (Figure 3.19, Figure 3.16b). While the majority of east slope precipitation events have winds that are predominantly westerly, there are several (high-precipitating) east slope events with northeasterly winds at Lander (Figure 3.19).

The 700 hPa winds during precipitation events vary only slightly from month to month at the Pinedale site, as illustrated in Figure 3.20, with the winds being largely west-northwesterly. Monthly analysis at the Lander site shows increasing frequency of the northeasterly winds during precipitation events in the latter half of the winter season (February–April), although westerly winds are still dominant (Figure 3.21). The Riverton monthly trends are very similar to those at Lander (not shown).

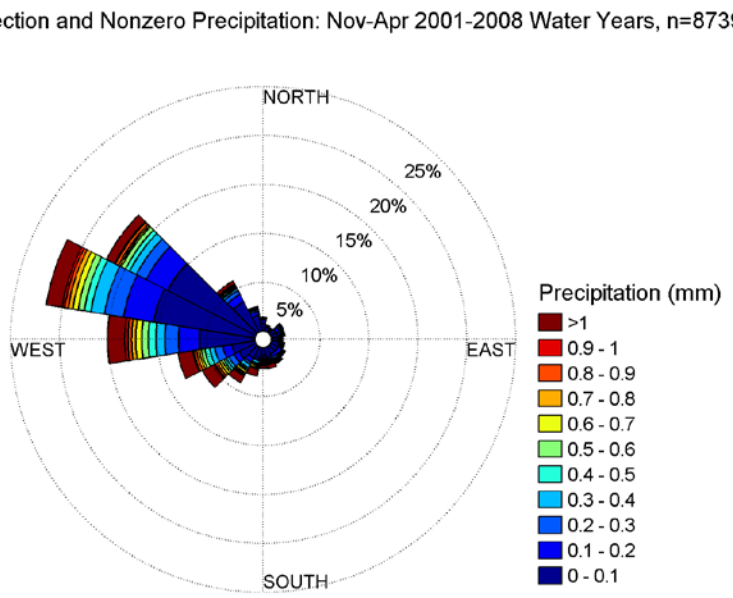

Figure 3.18. Wind rose showing the frequency of modeled 700 hPa wind direction over Pinedale, Wyoming when precipitation occurred over the Wind River Range (using the Big Sandy SNOTEL site) over the 8-year period from November–April. The magnitude of precipitation per hourly model output time for each wind direction is indicated by the color within each wind direction bin.

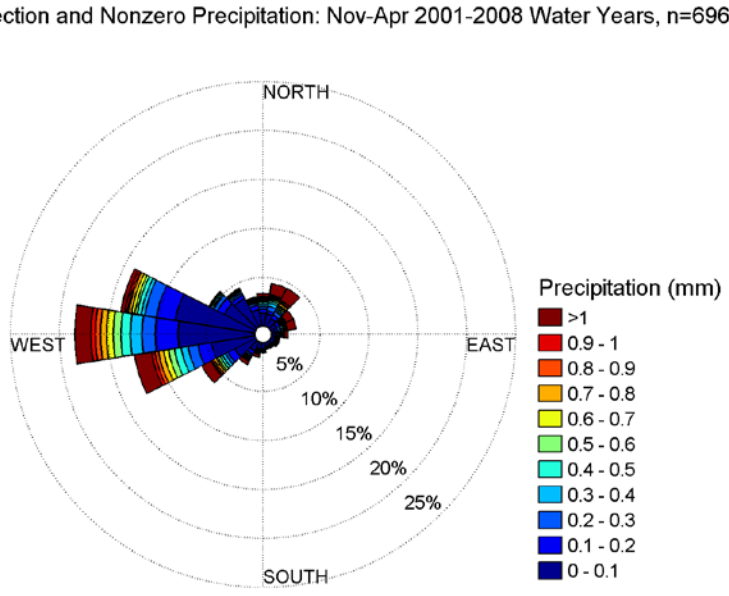

Figure 3.19. As in Figure 3.18, except for model 700 hPa winds over Lander when precipitation occurred at the Townsend SNOTEL site.

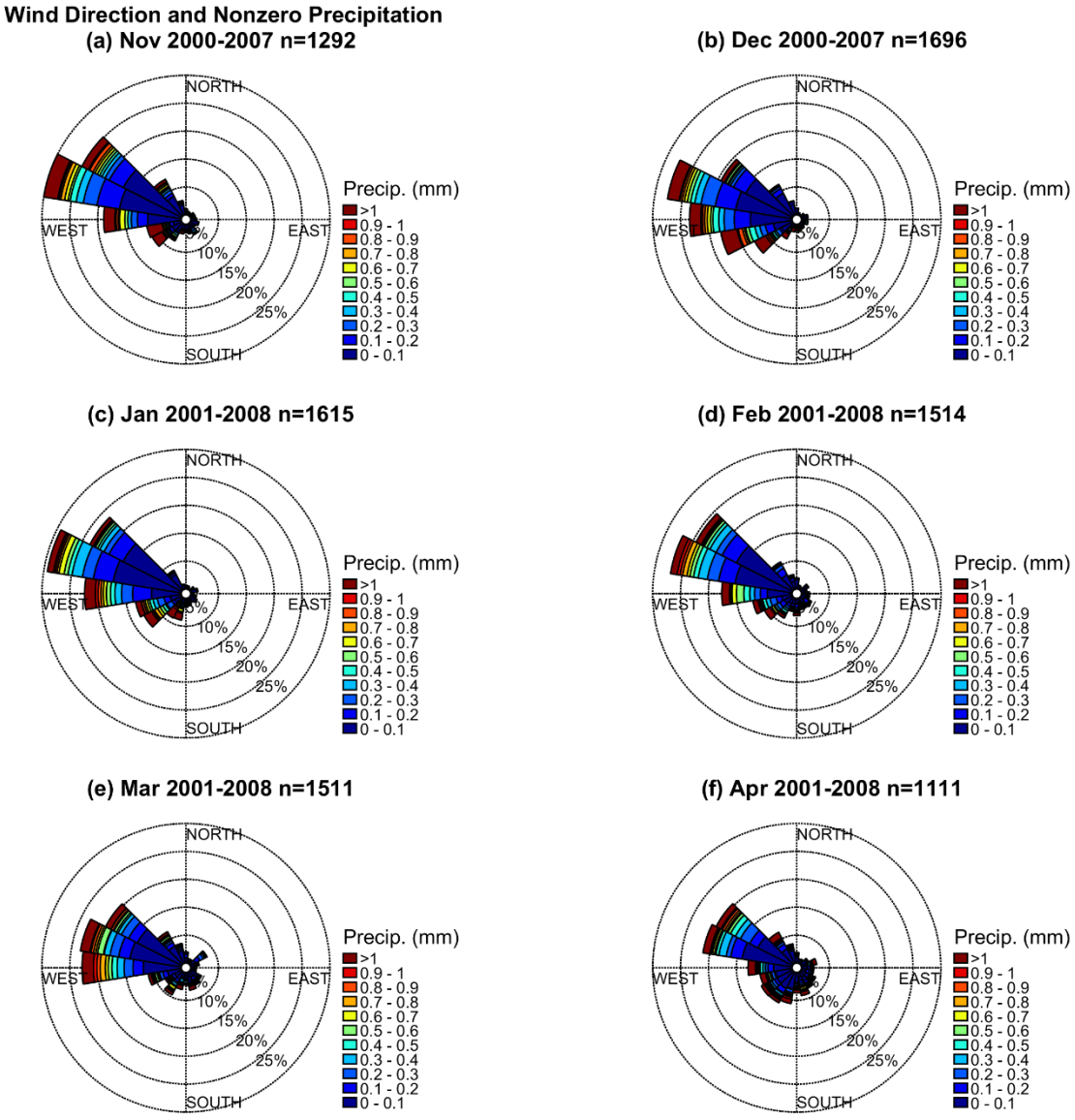

Figure 3.20. Month-by-month model wind roses of 700 hPa wind direction over Pinedale during model hours with precipitation at the Big Sandy SNOTEL site from November–April.

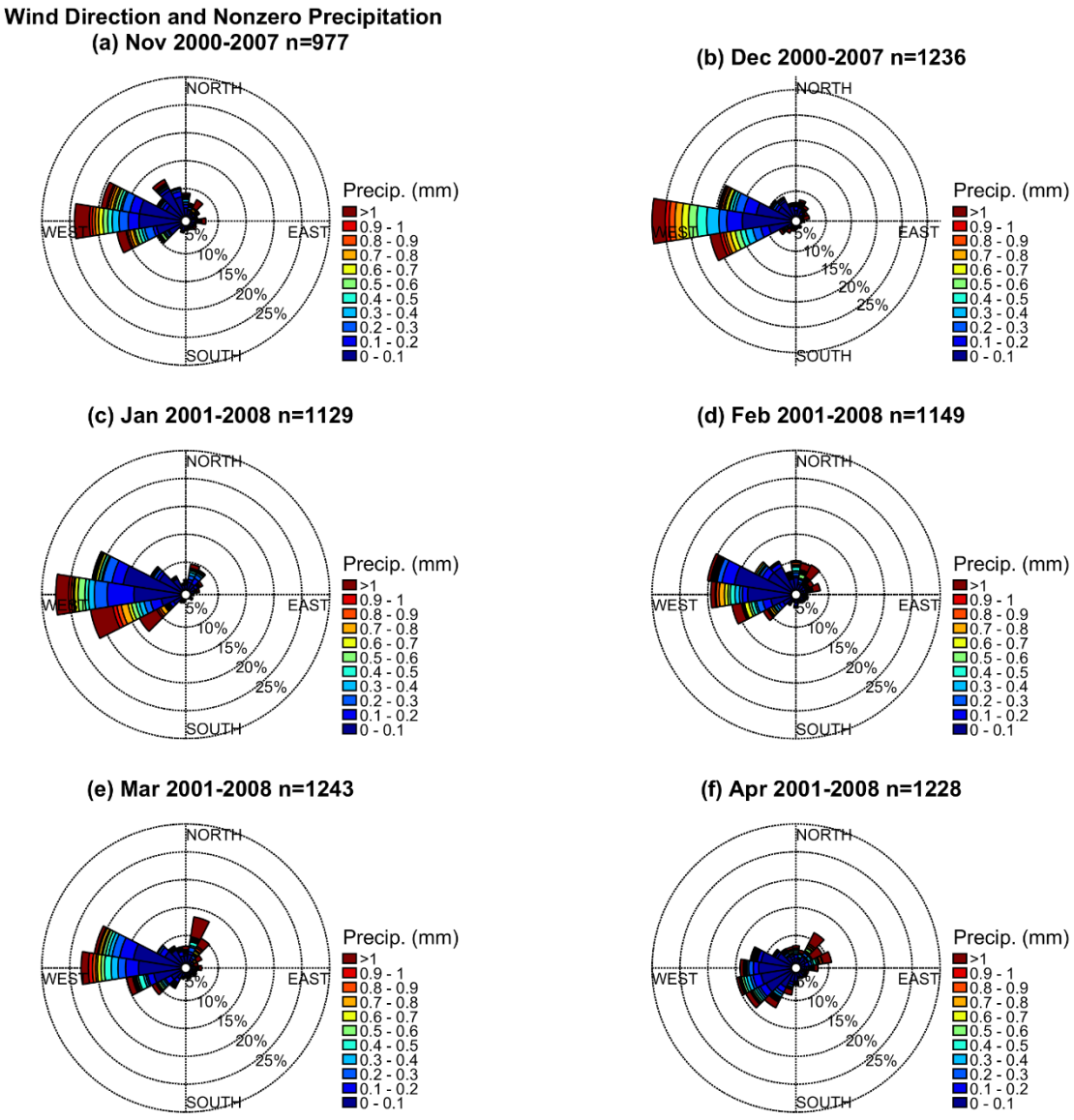

Figure 3.21. As in Figure 3.20, but for model winds over Lander and precipitation at the Townsend SNOTEL site.

The modeled 700 hPa temperatures at Pinedale over an average winter season ranged from 6°C to −22°C; however when precipitation occurred the temperatures were more focused between −2°C to −20°C (Figure 3.22). Roughly 60% of the wintertime hours over the 8-year period were colder than −6°C, whereas approximately 77% of the hours with precipitation were colder than −6°C. The 700 hPa temperature conditions at Lander were slightly warmer, ranging from 8°C to −20°C for the full winter season and 2°C to −18°C for precipitating events (Figure 3.23). Around 45% of wintertime hours were colder than −6°C, increasing to roughly 52% for hours with precipitation. Riverton 700 hPa temperatures very closely resemble those at Lander for all wintertime hours, but range only down to

−16°C for precipitating events (recall Figure 3.17b). Despite a warmer lower-temperature range at Riverton, the distribution of 700 hPa temperature during hours with precipitation is shifted to colder temperatures, resulting in roughly 60% of precipitating hours having temperatures colder than −6°C.

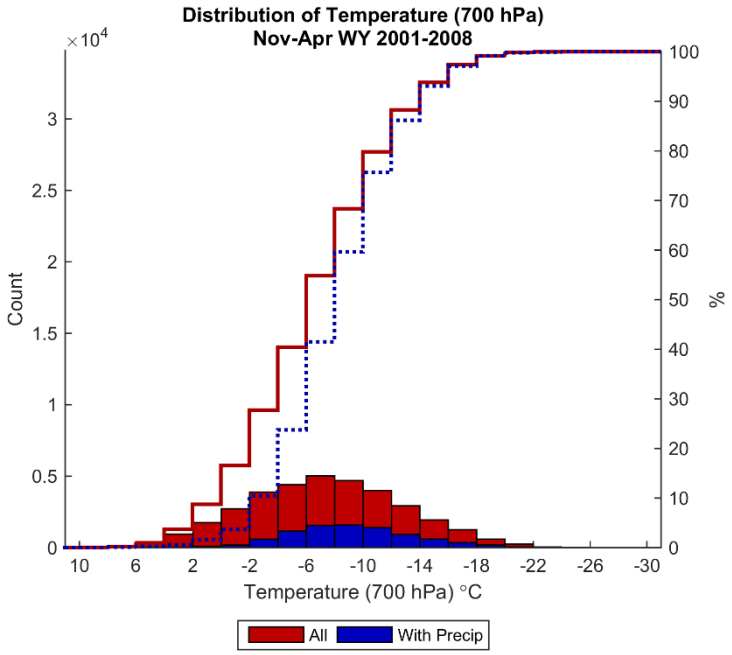

Figure 3.22. Histogram counts (left ordinate) of the modeled 700 hPa temperature at Pinedale, Wyoming for all hourly output from November–April from the 8-year (water years 2001–2008) model runs (red) and for all hourly output that had precipitation at the Big Sandy SNOTEL site (blue). Cumulative distributions for all (red) and with precipitation (blue dotted) are also overlaid using the right ordinate (%).

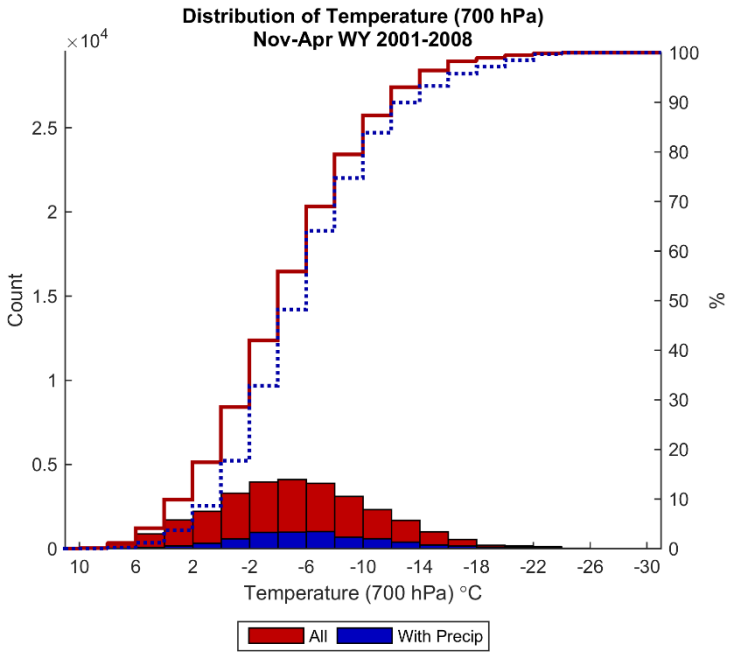

Figure 3.23. As in Figure 3.22, but using modeled 700 hPa temperature at the Lander, Wyoming site and precipitation from the Townsend SNOTEL site.

Area-based Analysis

Wintertime temperatures in the ground-seeding layer (0–1 km AGL) averaged over the western area ranged from 4°C to −24°C; however when precipitation occurred the span was more focused between −4°C and −20°C (Figure 3.24). The 0–1 km AGL temperatures averaged over the eastern area, shown in Figure 3.25, ranged from 6°C to −24°C for all hours and −2°C to −20°C when precipitation occurred.

The distribution of LWC over the western area shows that roughly 35% of all wintertime hours have no LWC, while less than 5% of the hours with precipitation have no LWC. In the eastern area, over 50% of all wintertime hours and roughly 10% of the hours with precipitation have no LWC. This suggests that in both regions, most precipitation occurs in situations with LWC and therefore some seeding potential could exist ~90–95% of the time precipitation occurs, as long as temperatures are also suitable (to be explored more below). Furthermore, the high frequency of hours with non-zero LWC *without* precipitation suggests a high frequency of conditions where precipitation could be initiated through seeding if the other conditions (e.g., temperature) are also suitable.

There is a fairly substantial difference in the LWC distributions between the eastern and western areas. The majority of all wintertime hours in the eastern area have zero LWC, while nonzero values are more prevalent in the western area. Further, the western area experiences greater quantities of LWC – as high as 0.45 g kg^{-1} – while the eastern area maxes out at 0.25 g kg^{-1}. The difference between seedable events between the eastern and western regions will be explored more below.

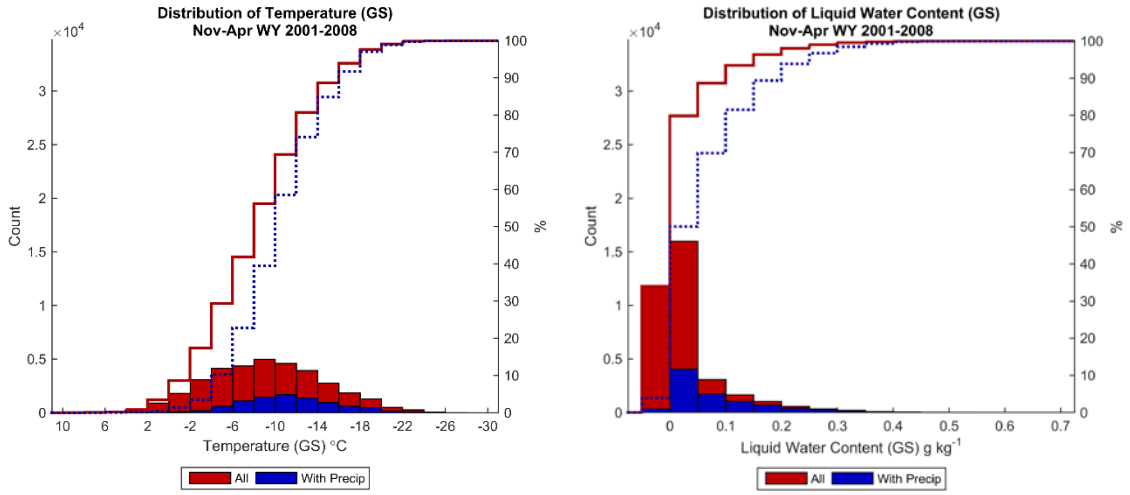

Figure 3.24. Histogram counts (left ordinate) of the west area average 0–1 km AGL temperature (left) and 0–1 km AGL LWC (right) for ground seeding (GS) for all hourly output from Nov–Apr from the 8-year (Water Years 2001–2008) model runs (red) and for all hourly model output that had precipitation at the Big Sandy precipitation site (blue). Cumulative distributions for all (red) and output hours with precipitation (blue dotted) are also overlaid using the right ordinate (%). The bar to the left of the zero includes all values equal to zero.

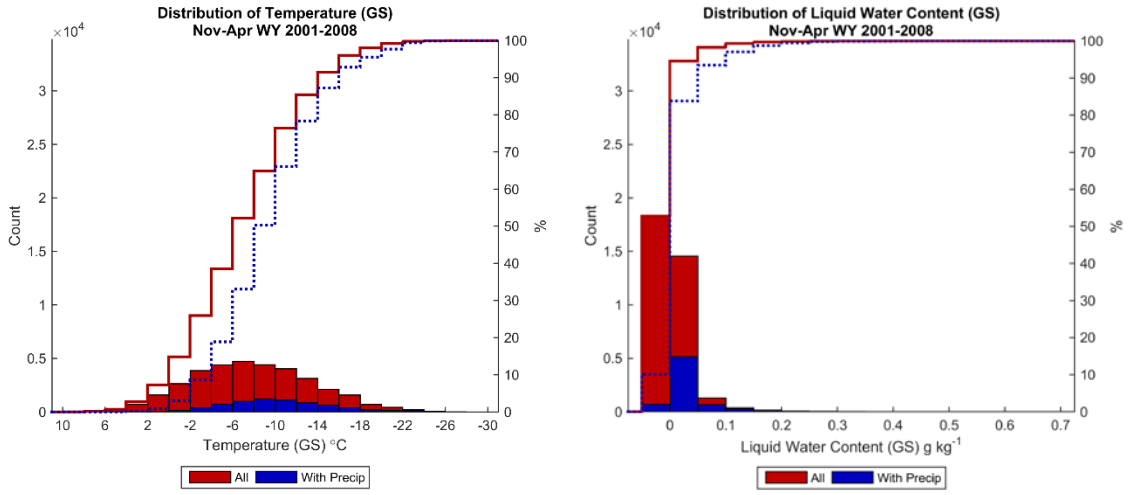

Figure 3.25. As in Figure 3.24, but areal averaged values from the eastern area and precipitation from the Townsend site.

The distribution of LWP is very similar to that of LWC for the ground-seeding layer for both areas (Figure 3.26). This is because the majority of the liquid water in the vertically-integrated LWP value is confined within the lowest layer of the atmosphere. This has implications for the feasibility of airborne seeding, as will be described more below.

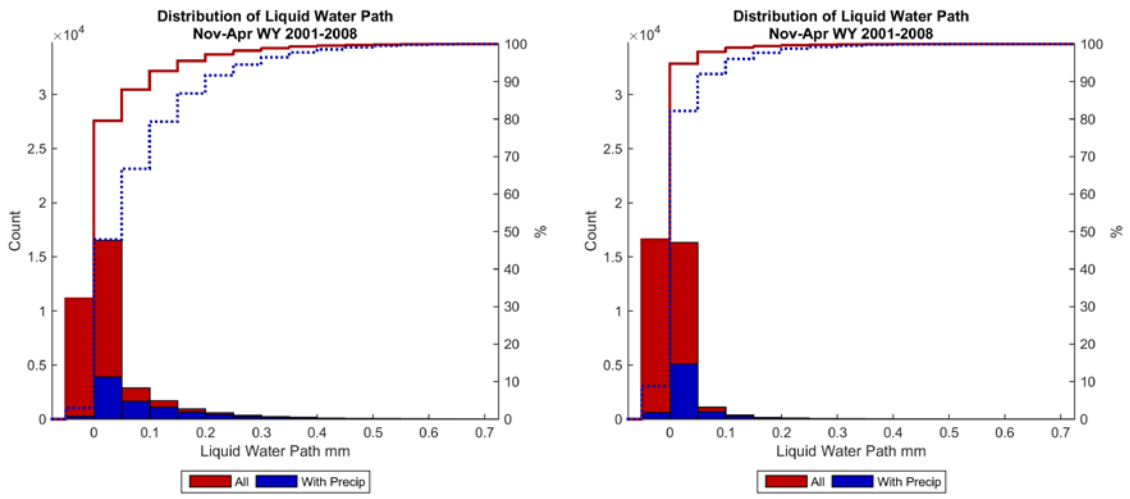

Figure 3.26. As in Figure 3.24, except for average model LWP in the western (left) and eastern (right) areas. The model precipitation was from the Big Sandy (west) and Townsend (east) sites.

The Froude number distribution illustrates that for roughly 50% of wintertime hours in the western area and 40% in the eastern area, there is a situation conducive to flow being blocked by the mountain barrier (Fr<0.5, Figure 3.27). This condition is present only ~20% of the time when precipitation occurs, however, for both regions.

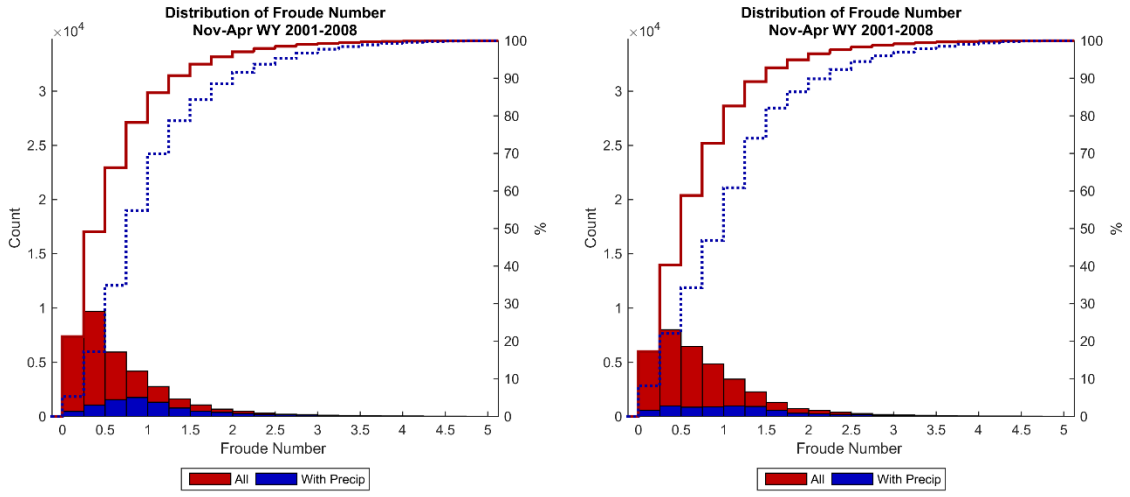

Figure 3.27. As in Figure 3.24, except for average Froude number in the western (left) and eastern (right) areas. The model precipitation was from the Big Sandy (west) and Townsend (east) sites.

Cloud base heights in the western area during winter are typically between 2500 and 3500 m MSL (~70% of all hours in winter have cloud base heights in this range), and nearly 100% of the cloud base heights during winter hours with precipitation are in this range (Figure 3.28). The eastern area experiences many more clouds with bases >6000 m MSL, and clouds during winter hours with precipitation also occur at greater heights. Cloud depths in both regions range as deep as 9000 m, but the western area shows more of a

prevalence of shallow cloud as compared to the eastern area (Figure 3.29). Precipitating clouds in the western area have depths fairly uniformly distributed between 500 and 7000 m, with less than 5% of precipitating clouds being less than 500 m in depth. Despite deeper clouds overall in the eastern area, the eastern precipitating clouds tend to be shallower than their western counterparts, with ~15% of precipitating clouds being less than 500 m deep. The western area has a greater frequency of non-precipitating clouds with cloud top temperatures in the −5°C to −20°C range than precipitating clouds (Figure 3.30). These are ideal cloud seeding conditions. The distributions of precipitating and non-precipitating clouds are very similar to one another in the eastern area.

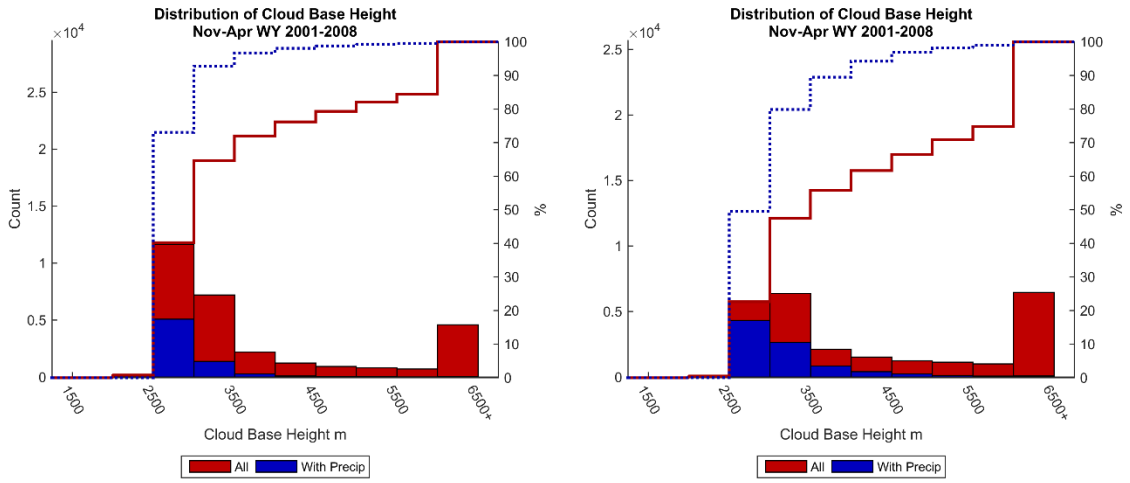

Figure 3.28 As in Figure 3.24, except for average cloud base height in the western (left) and eastern (right) areas. The model precipitation was from the Big Sandy (west) and Townsend (east) sites.

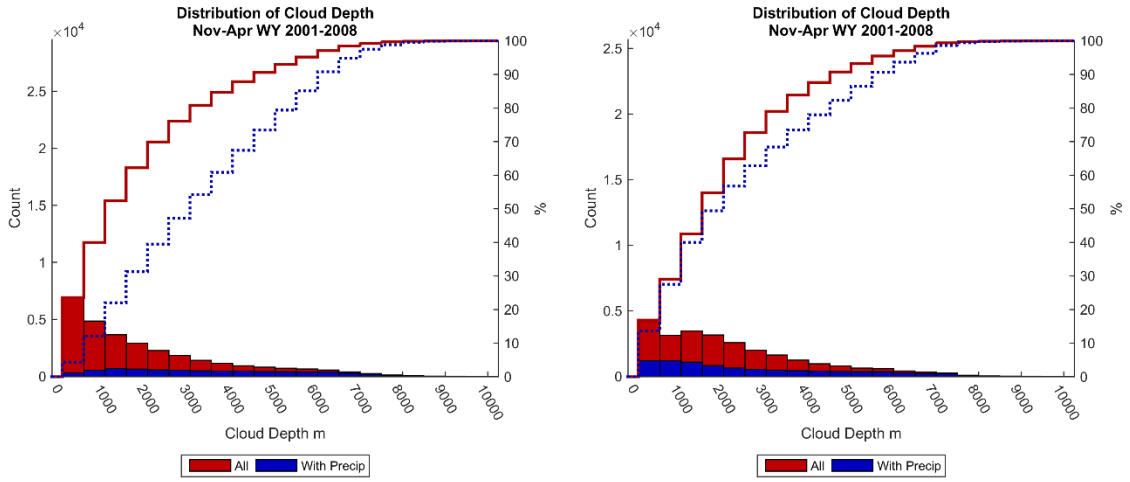

Figure 3.29. As in Figure 3.24, except for average cloud depth in the western (left) and eastern (right) areas. The model precipitation was from the Big Sandy (west) and Townsend (east) sites.

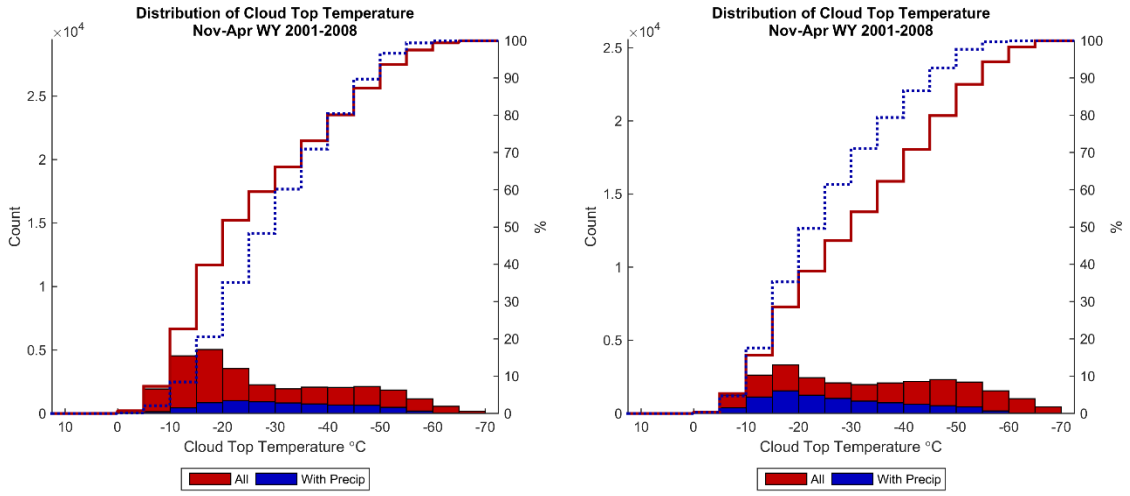

Figure 3.30. As in Figure 3.24, except for average cloud top temperature in the western (left) and eastern (right) areas. The model precipitation was from the Big Sandy (west) and Townsend (east) sites.

The amount (and percent) of seasonal precipitation that falls when the western (eastern) area-averaged 700 hPa temperatures are colder than −6°C is shown by water year in Table 3.3 (Table 3.4). The 8-year seasonal average over the western area was 72%, as compared to 60% over the eastern area. Both areas varied quite a bit from year to year, with the western side as high as 96% and down to 58%, and the eastern side ranging from 37–75%. In both areas, water year 2008 (2006) was the coolest (warmest) year, with the most (least) precipitation falling when temperatures were colder than −6°C. The eastern area had a slightly lower 8-year seasonal average precipitation than the western area, but year-to-year values indicate that the western area does not always experience more precipitation than the eastern area. However, temperatures are consistently warmer on the eastern side during precipitation events.

Total *annual* precipitation falling when 700 hPa temperatures are colder than −6°C are included in Table 3.3 and Table 3.4 in order to account for seeding opportunities that may arise outside of the November–April period. Naturally, a smaller percentage of the annual precipitation falls under suitable conditions.

Table 3.3. Seasonal (Nov–Apr) and annual (Oct–Sep) model precipitation totals extracted near the Big Sandy site and the amount of precipitation that fell when the western area average 700 hPa temperature was >= −6°C.

Season (Water Year)	Seasonal Precipitation (mm)	Seasonal Precipitation (mm) when 700 hPa T > −6°C	Annual Precipitation (mm)	Annual Precipitation (mm) when 700 hPa T > −6°C
2001	288	222 (77%)	455	235 (52%)
2002	316	250 (79%)	519	259 (50%)
2003	360	219 (61%)	544	230 (42%)
2004	345	274 (79%)	584	285 (49%)
2005	401	296 (74%)	752	318 (42%)
2006	563	328 (58%)	746	330 (44%)
2007	399	241 (60%)	648	243 (38%)
2008	412	394 (96%)	658	407 (62%)
8-year Average	386	278 (72%)	613	288 (47%)
Standard Deviation	84	60	107	61

Table 3.4. As in Table 3.3, but precipitation totals from the Townsend site and 700 hPa temperatures averaged over the eastern area.

Season (Water Year)	Seasonal Precipitation (mm)	Seasonal Precipitation (mm) when 700 hPa T > −6°C	Annual Precipitation (mm)	Annual Precipitation (mm) when 700 hPa T > −6°C
2001	173	107 (62%)	363	154 (42%)
2002	340	231 (68%)	581	265 (46%)
2003	333	196 (59%)	564	203 (36%)
2004	442	310 (70%)	867	355 (41%)
2005	426	251 (59%)	761	258 (34%)
2006	377	140 (37%)	555	157 (28%)
2007	314	165 (53%)	765	201 (26%)
2008	350	264 (75%)	668	286 (43%)
8-year Average	344	208 (60%)	652	235 (37%)
Standard Deviation	83	68	156	69

In the airborne-seeding layer (4–5 km MSL), the temperature range in wintertime is shifted slightly cooler than in the ground-seeding layer, as would be expected. Additionally, the airborne layer temperature distributions are very similar for the eastern and western areas. In the airborne layer it ranges from −2°C to −30°C, with the range slightly cooler between −8°C and −26°C when precipitation occurred (Figure 3.31, Figure 3.32). Specifically, ~90% of all wintertime hours were colder than −6°C, whereas roughly 98% of the wintertime hours with precipitation were colder than −6°C. In fact, 20–30% of all wintertime hours and 40–50% of precipitating wintertime hours have temperatures colder than −18°C, becoming too cold for AgI cloud seeding.

The range of LWC in the airborne-seeding layer over the western area is diminished compared to that in the ground-seeding layer (Figure 3.24, Figure 3.31). The range in the eastern area is not much diminished, although there are substantially more instances of precipitation with zero LWC (Figure 3.32). Again, the frequency of nonzero LWC without precipitation indicates potential seeding opportunities, although the opportunities are diminished as compared to the ground-seeding layer.

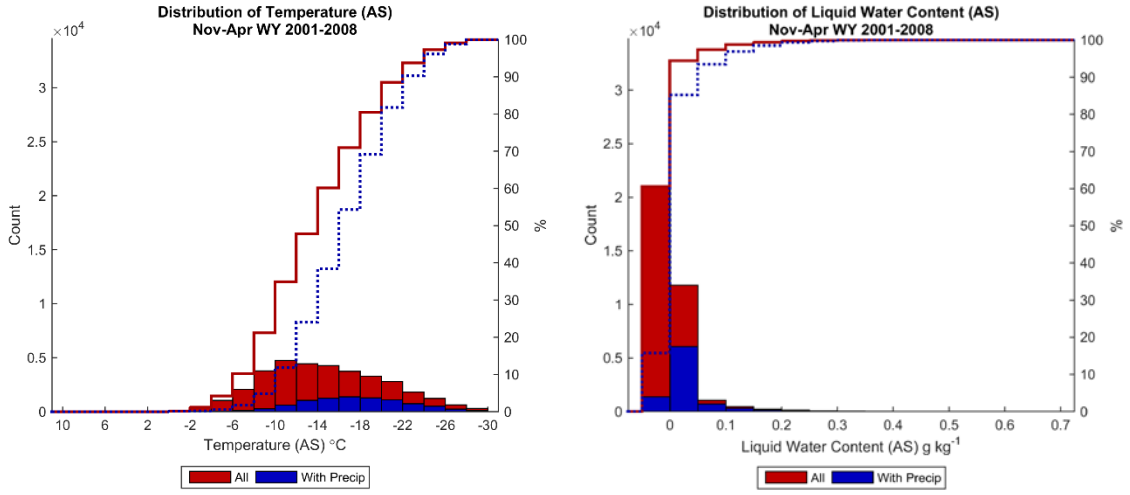

Figure 3.31. As in Figure 3.24, except for in the 4–5 km MSL layer (for airborne seeding; AS).

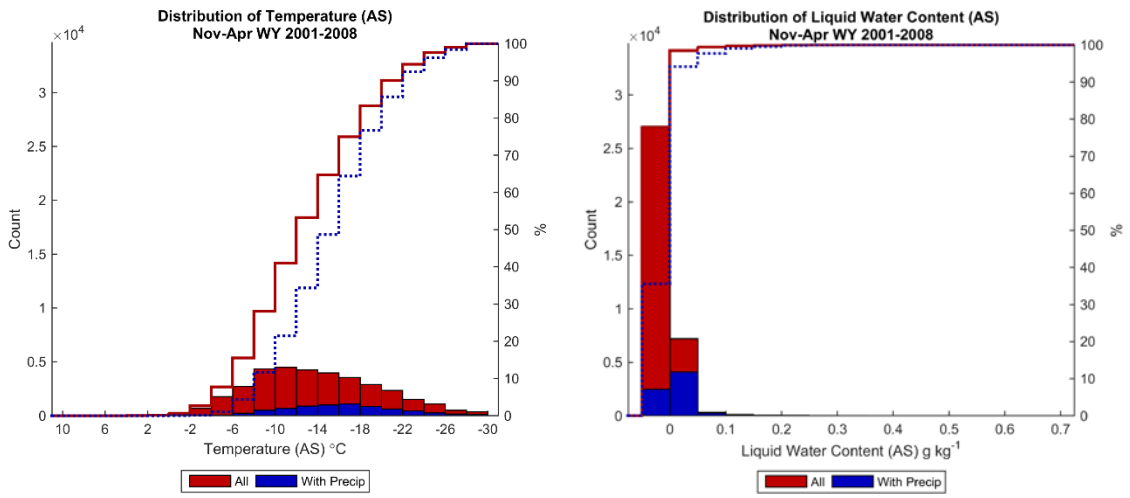

Figure 3.32. As in Figure 3.25, except for in the 4–5 km MSL layer.

A higher airborne layer was also examined for seeding opportunities (4.75–5.85 km MSL), but 50–60% of all wintertime hours and 70–80% of precipitating wintertime hours had temperatures colder than −18°C, and both the eastern and western areas show very little LWC in this range (not shown). As a result, the higher airborne layer will not be the focus of the remaining discussion.

As mentioned for both ground and airborne seeding above, the occurrence of LWC when no precipitation occurred shows potential for cloud seeding if the temperature is also suitable. Therefore, for the ground seeding layer and the 4–5 km MSL airborne seeding layer, we provide histograms of the layer average temperature during periods when there was LWC present (western area, Figure 3.33; results in the eastern area are nearly identical and thus not shown). Interestingly, the cumulative temperature distributions when LWC was present both with and without precipitation are very similar. This suggests that when LWC is present, there is no dependence on the layer temperature for precipitation to occur. Generally 90% (95%) of the time that LWC was present for ground seeding (airborne seeding) the temperature was colder than −6°C. About 10% (40%) of ground seeding (airborne seeding) temperatures were colder than −18°C, resulting in roughly 80% (55%) of wintertime events for which LWC was present having suitable temperatures for cloud seeding.

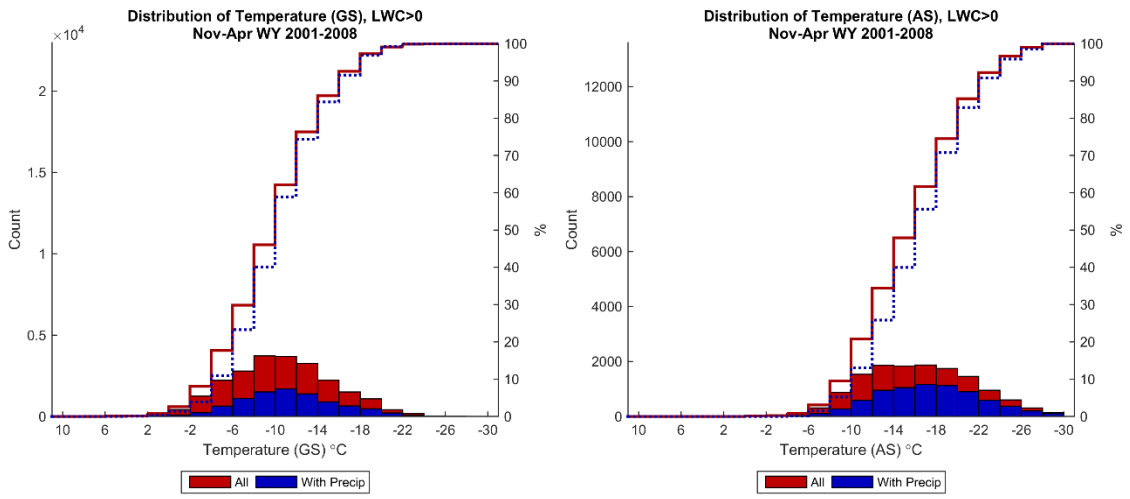

Figure 3.33. Histogram counts (left ordinate) of the western area average 0–1 km AGL temperature when LWC was present (> 0) in the layer (left) and 4–5 km MSL temperature when LWC was present in the layer (right) for all hourly output between November and April from the 8-year (Water Years 2001–2008) model runs (red) and for all hourly output that had precipitation at the Big Sandy SNOTEL site (blue). Cumulative distributions are included as in Figure 3.24.

3.3. Climatology of Cloud Seeding Opportunities

When considering the two key criteria for cloud seeding potential, appropriate temperature and the presence of liquid water, the frequency that these criteria are met can be established using either observations (if available) or model output. This provides a general sense of the frequency of cloud seeding opportunities.

Using the model output, we can calculate the fraction of hours in a given month, the entire winter season (between November and April), or the full year in which those two criteria are both met. Additional criteria that may affect the potential for seeding are wind direction and stability indices. These variables will be analyzed via the spatial mapping analysis and the area-based analysis below for both ground and airborne seeding potential. Unfortunately, observations of liquid water (such as from a radiometer) during the 8-year period of the WRF regional climate simulation are not available in order to do this analysis using observations. However, a comparison of radiometer data to model output during RSE showed good agreement in most cases (WWDC 2014).

3.3.1. Model-based Analysis Results

Ground Seeding Spatial Mapping Analysis

Figure 3.34 shows the frequency (% of time analyzed for all eight seasons) that seeding criteria are met within the 0 to 1 km AGL ground-seeding layer. LWP and LWC frequency contours have similar magnitudes and spatial coverage, indicating most of the LWC is in the ground-seeding layer. The LWP or LWC mixing ratio and their spatial distribution compared to Figure 3.34d (LWP and temperature criteria combined) indicate that the presence of liquid water is the most important factor controlling the frequency of seeding opportunities. This is clear in the northern portion of the Wind River Range where high

mixing ratios of LWC correspond to higher frequency of seeding conditions (temperature plus LWP concurrently) being met. A sharp gradient in frequency is apparent in LWP and LWC as the mountain barrier is crossed from west to east. It is immediately apparent that the frequency of seeding opportunities decreases to very low values from the peak of the Wind River Range to the eastern slopes. The western slopes of the Wind River Range are most conducive to seeding in the 0 to 1 km AGL layer. Temperature criteria are satisfied at a high frequency and have very little impact on limiting seedability. The combination of temperature and LWP concurrently shows a maximum frequency of seeding opportunities of about 30% along the northern-most portion of the Wind River Range and around 24% along the western slopes of the Wind River Range. The frequency of ground seeding opportunities along the east slope is up to 15%.

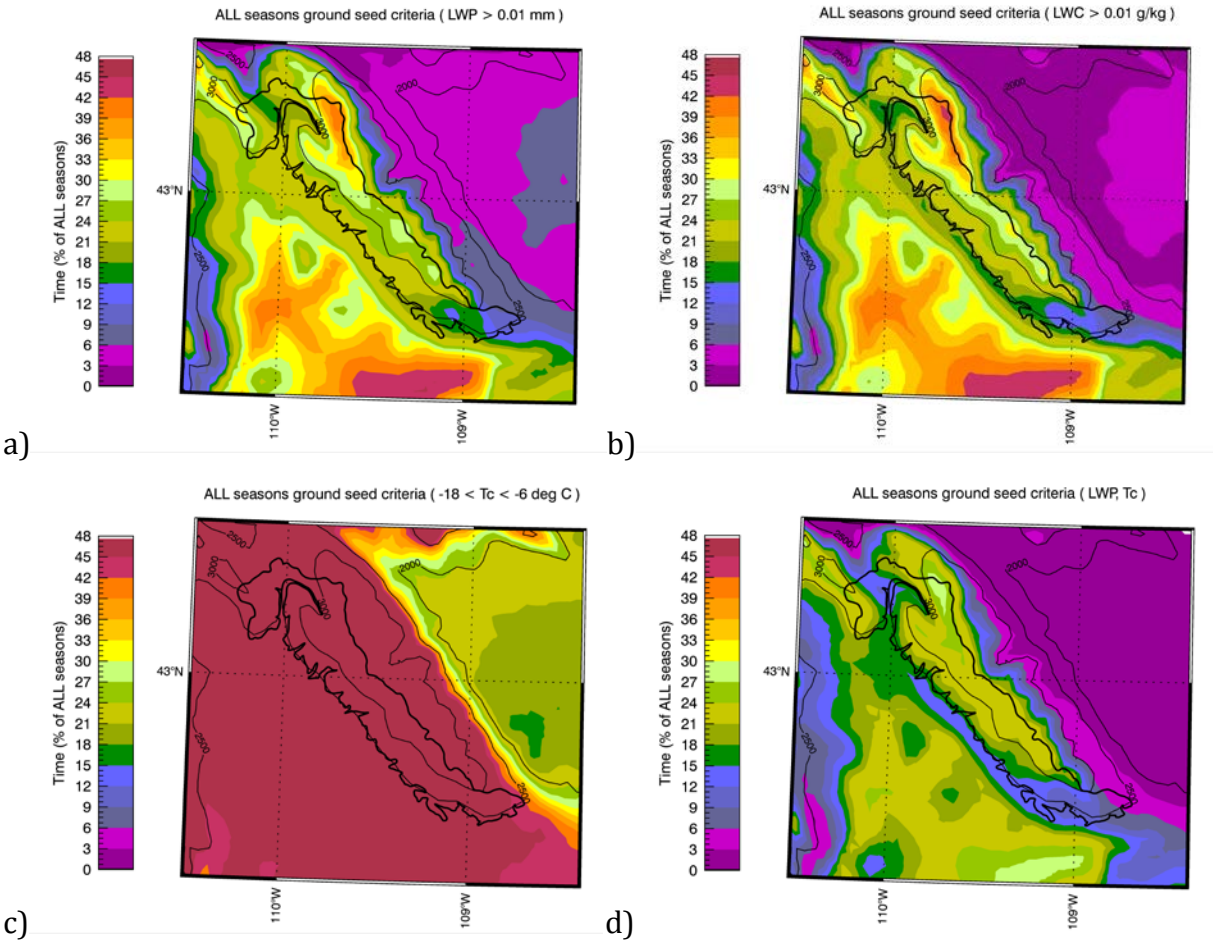

Figure 3.34. Frequency (percent of time) that seeding criteria are met within the 0–1 km AGL layer for all seasons (2000–2008): a) LWP, b) LWC, c) Temperature, d) LWP and Temperature concurrently. Note: the colorbar has a maximum value of 48% (same across all figures) and values greater than 48% are not shown. Thin black contours indicate the topography (every 500 m MSL). A thick black line outlines the Green River Basin watershed above 8000 ft, and is indicative of the Wind River Range west slope target area.

Airborne Seeding Spatial Mapping Analysis

Figure 3.35 shows the seedability frequency maps for a potential airborne seeding layer (4–5 km MSL) in the November–April winter months. The spatial pattern in frequency for all meteorological parameters is consistent with the ground seeding results over the Wind

River Range. Differences can be observed in the magnitude of the frequencies, but the similarity in the contour pattern persists. This suggests that the meteorological fields are strongly correlated with terrain features. In the 4–5 km MSL layer, the seedability decreases to no more than 24% with the highest frequency confined to a narrow strip along the western side of the crest of the Wind River Range. These reductions in airborne seedability compared to the ground-seeding layer are driven by temperatures getting too cold at these higher altitudes, given they are still based on LWP, which is the same for all layers. Analysis of LWC in the 4–5 km MSL layer indicates that the frequency of occurrence of LWC in the winter months is up to 27%, but only in the small maximum on the northern end of the Range (Figure 3.35b). Otherwise, along the rest of the west slope of the Range, the frequency of LWC occurrence is closer to 15%.

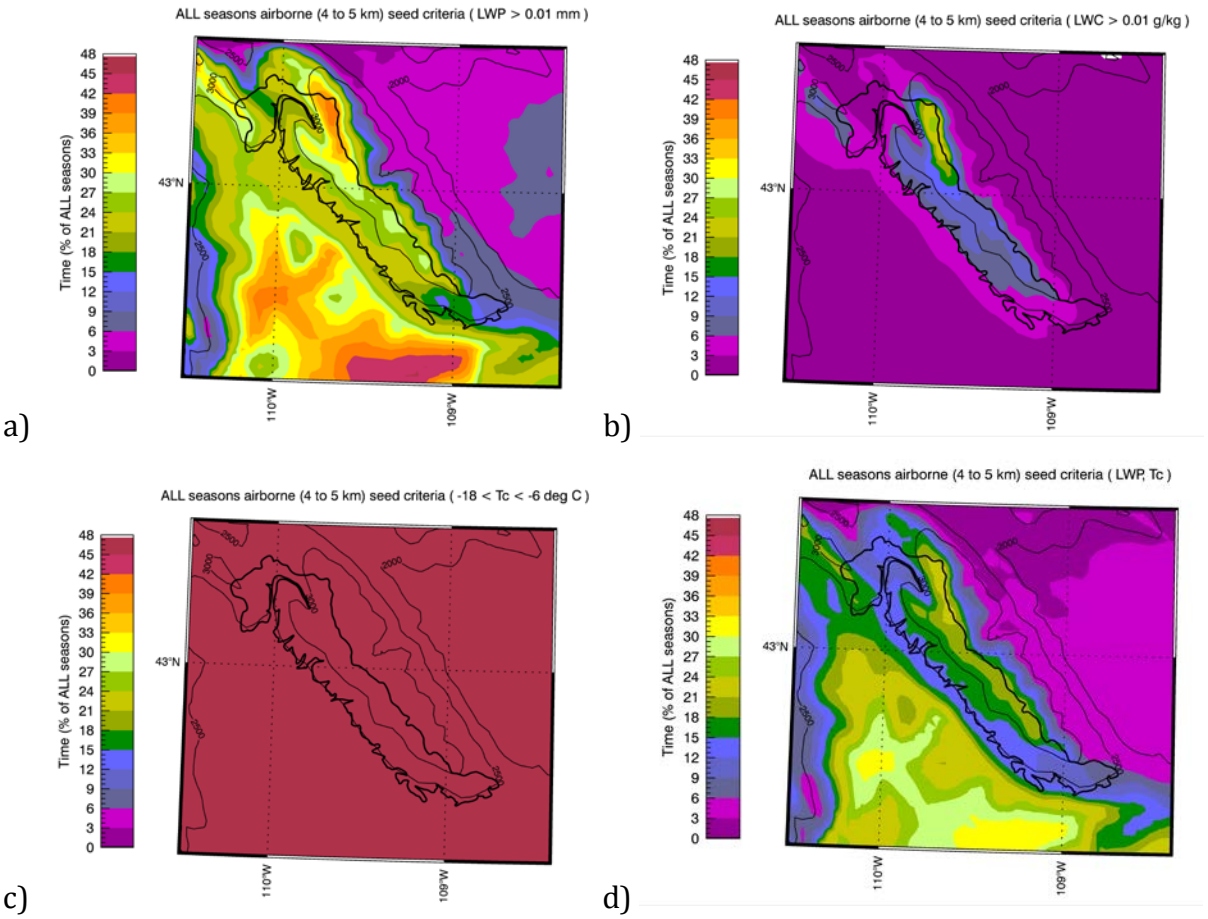

Figure 3.35. Frequency (percent of time) that seeding criteria are met within the 4–5 km MSL layer for all seasons (2000–2008): a) LWP, b) LWC, c) Temperature, d) LWP and Temperature concurrently. Note: the colorbar has a maximum value of 48% (same across all figures) and values greater than 48% are not shown. Thin black contours indicate the topography (every 500 m MSL). A thick black line outlines the Green River Basin watershed above 8000 ft, and is indicative of the Wind River Range west slope target area.

Ground Seeding Area-based Analysis

Western Area

On a monthly basis, the seasonality of ground-based cloud seeding opportunities (defined as meeting the temperature and LWC criteria) is primarily between November and April (Figure 3.36). In fact, the 8-year average fraction of hours in the month that meet these two criteria for the western area is nearly 35% from December–March. However, when these results are normalized by the presence of precipitation over the target area (using modeled precipitation from the Big Sandy SNOTEL site), the fraction of hours is nearly reduced by half. This indicates that there may be some non-precipitating opportunities for cloud seeding.

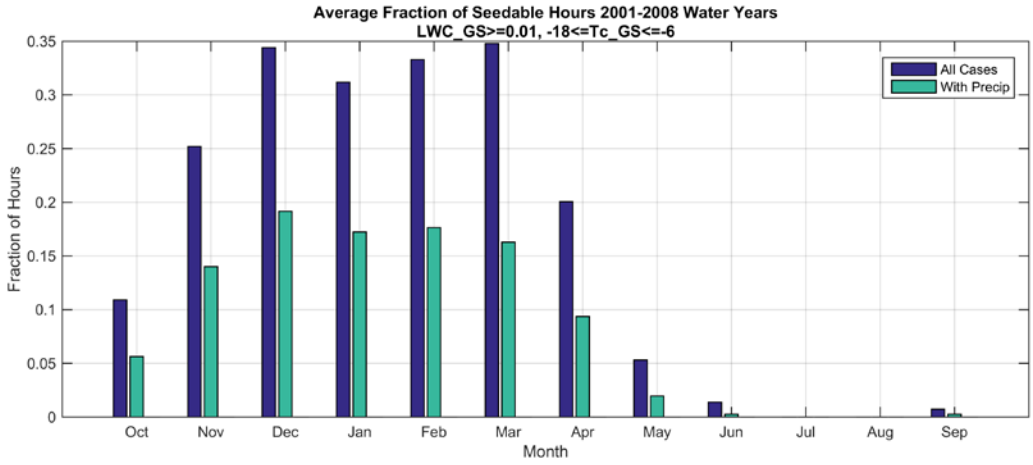

Figure 3.36. Bar chart showing the average fraction of hours in a month that met the temperature and LWC criteria averaged over the western area for ground-based seeding (0–1 km AGL; blue) and the same for hours that also had precipitation in the model near the Big Sandy SNOTEL site (green).

When the monthly distribution of wintertime hours that met temperature and LWC criteria are broken down by season, the interannual variability in seeding opportunities is apparent (Figure 3.37). For example, the 2007 water year had far fewer opportunities for ground-based seeding than most of the other water years in nearly all months. This is also supported by the seasonal fraction of hours meeting seeding criteria (temperature and LWC) for the 2007 water year in Figure 3.38. However, some years, such as water years 2004–2006, have a similar seasonal fraction of seedable hours (Figure 3.38), yet one dominant month drives the seasonal opportunities (see Figure 3.37; November, March, and January drive the results for water years 2004, 2005, and 2006, respectively). This illustrates that the seasonality of seeding opportunities varies some from year to year, but at least over the 8-year period of study, most seasons had between 25 and 35% of the wintertime hours meeting the temperature and LWC criteria, so the variable seasonality often balances out over the course of the winter. The 8-year average shows 30% of the wintertime hours as being seedable, based on meeting the primary criteria in the ground-seeding layer. Considering only cases when precipitation was simulated over the target area reduces these fractions roughly by half, with an 8-year average at ~16% of all wintertime hours being seedable with precipitation. When normalized by the presence of clouds rather than the presence of precipitation, the 8-year average frequency of ground-

based seeding opportunities is 70% (not shown). This indicates that nearly three quarters of wintertime clouds in the region meet the temperature and LWC criteria for ground-based seeding.

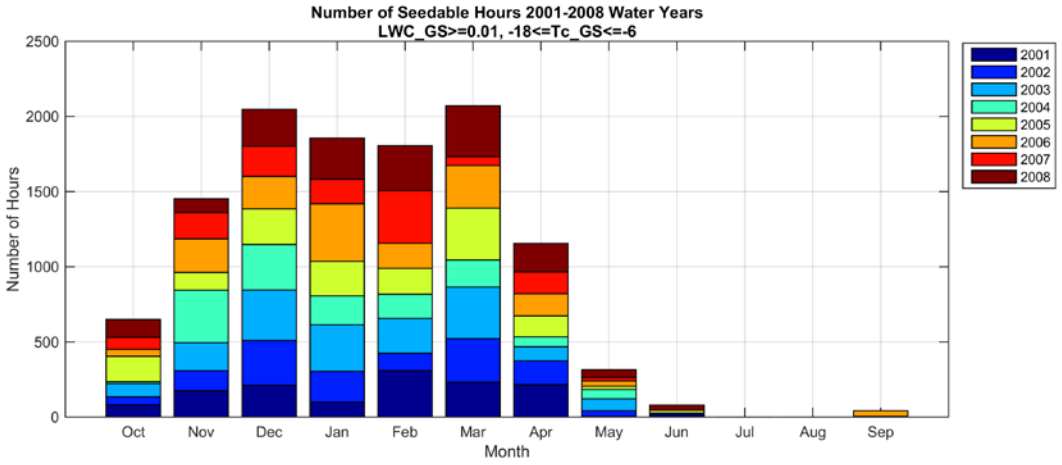

Figure 3.37. Bar chart showing the number of hours in a given month that met the temperature and LWC criteria averaged over the western area for ground-based seeding (0–1 km AGL). Each color represents one of the 8 years simulated by the model.

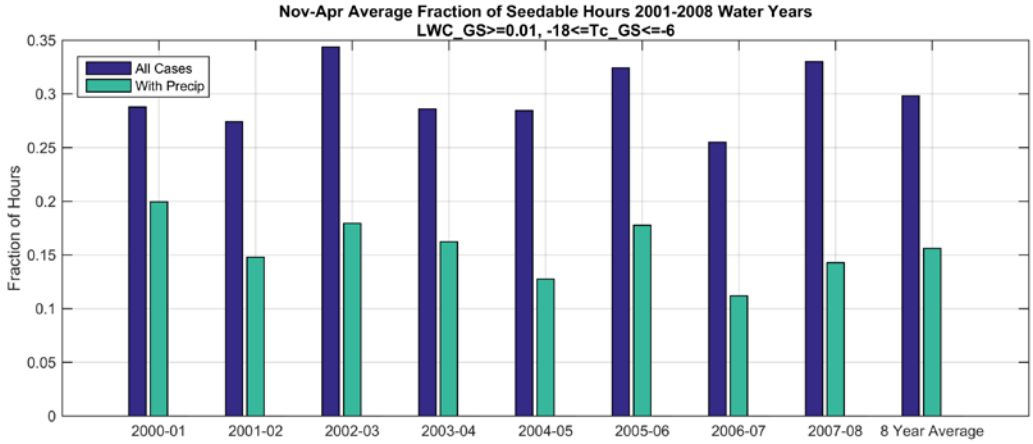

Figure 3.38. Bar chart showing the average fraction of hours in a winter season (Nov–Apr) that met the temperature and LWC criteria averaged over the western area for ground-based seeding (0–1 km AGL; blue) and the same for hours that also had precipitation in the model near the Big Sandy SNOTEL site (green).

Since ground-based seeding generators are typically at fixed locations, and based on the wind direction climatology need to be on the western upwind slopes of the Wind River Range, a wind direction criterion can be added to this analysis to identify the frequency at which seeding conditions occur when the 700 hPa wind directions are favorable for transport of the ground-based seeding material over the barrier (between 180 and 290 degrees). When imposing a wind direction criterion on the ground-based seeding potential, the frequencies were substantially reduced, from an 8-year average of 30% to 15% of all wintertime hours, and from 16% to 9% of wintertime hours that also had precipitation (Figure 3.39).

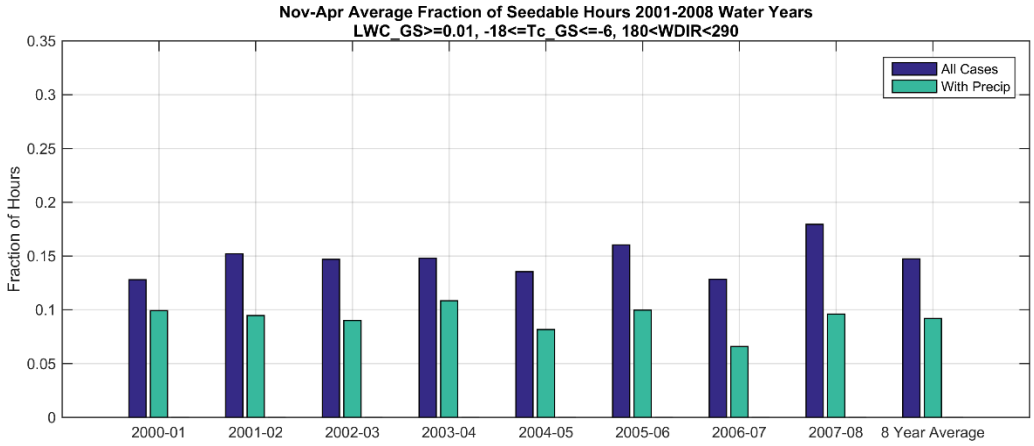

Figure 3.39. As in Figure 3.38, except also including 700 hPa wind direction (between 180 and 290 degrees) as an additional criterion for ground seeding potential.

Moreover, since AgI released from ground-based generators needs to be able to disperse vertically up and over the mountain barrier, it is important to also assess the stability of the atmosphere. When including the additional criterion of Fr > 0.5 to the analysis of frequency of ground seeding conditions (indicative that flow would be less likely to be blocked by the mountain barrier), the frequency of opportunities for ground-based seeding was reduced a bit more (Figure 3.40) to roughly 14% of the season, based on the 8-year average.

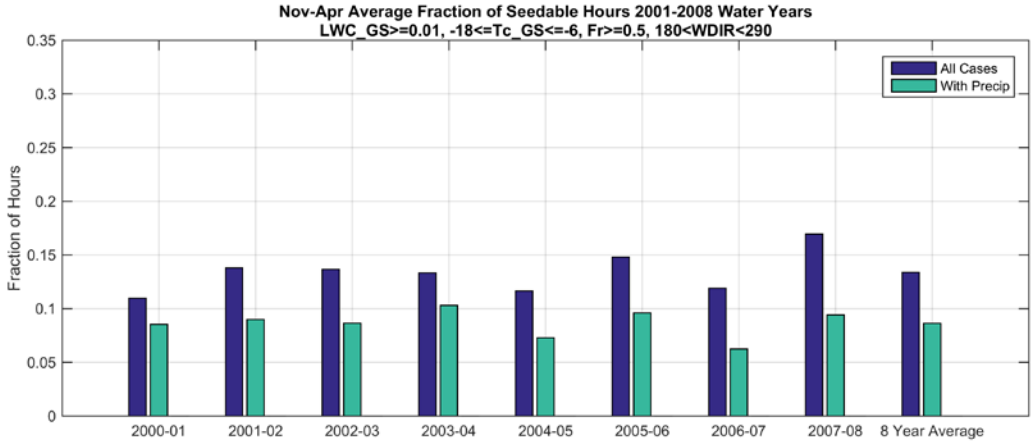

Figure 3.40. As in Figure 3.38, except also including 700 hPa wind direction and Froude number > 0.5 as additional criteria for ground seeding potential.

Eastern Area

Ground seeding opportunities in the eastern area are also primarily between November and April, but occur at a much lower rate than in the western area (roughly 18% in the December–March period as opposed to nearly 35% in the western area; Figure 3.36 and Figure 3.41). Moreover, their seasonal frequency is much more variable from year to year (Figure 3.42). Including the Froude number and wind direction criteria (on the eastern slope, restricting to 20–100 degrees) for ground seeding severely reduces the fraction of

wintertime hours conducive to ground seeding, dropping to a maximum of 2% of the winter season and an 8-year average of less than 1% (Figure 3.42; note y-axis limit).

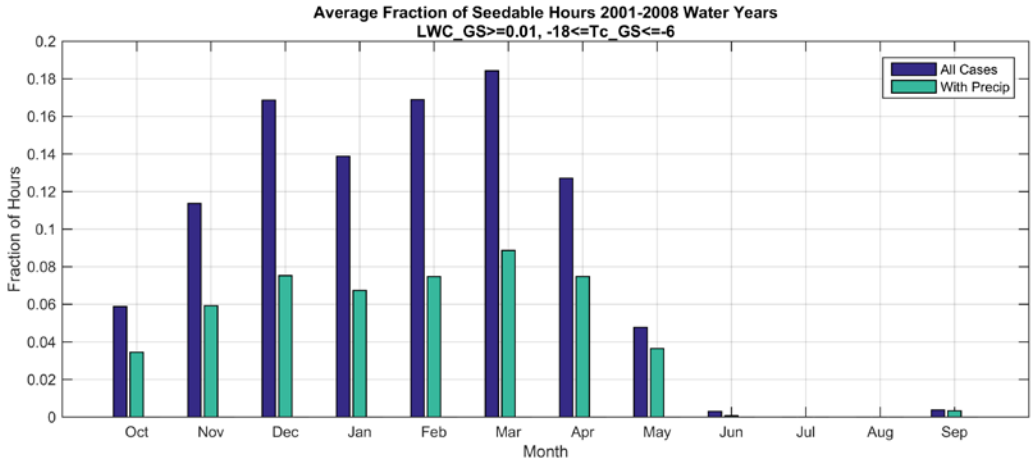

Figure 3.41. As in Figure 3.36, but over the eastern area and using precipitation near the Townsend SNOTEL site.

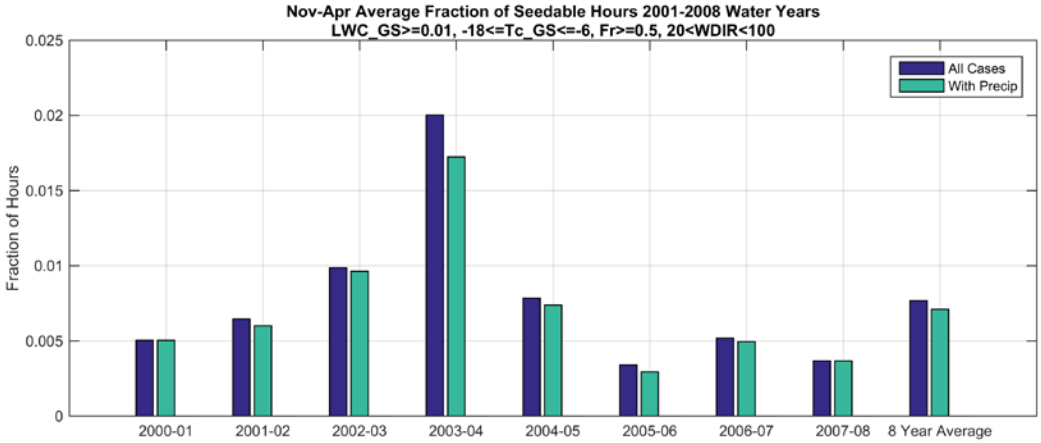

Figure 3.42. As in Figure 3.40, but over the eastern area (with the 700 hPa wind direction criterion between 20 and 100 degrees) and using precipitation near the Townsend SNOTEL site.

Indeed, combining the eastern and western areas yields only a very small increase of the fraction of wintertime hours that are ground-seedable – defined here as meeting the combined criteria of temperature, LWC, wind direction, and Froude number – as shown in Figure 3.43.

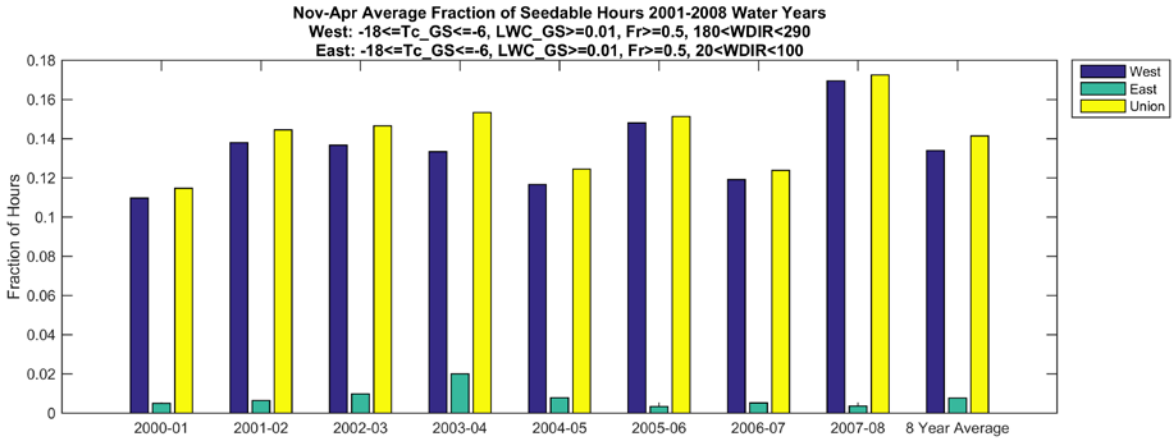

Figure 3.43. Bar chart showing the average fraction of hours in a winter season (Nov–Apr) that met the temperature, LWC, wind direction, and Froude number criteria averaged over the western area (blue) and eastern area (green) for ground-based seeding (0–1 km AGL). The union of the two regions is shown in yellow.

Airborne Seeding Area-based Analysis

Analysis of the airborne seeding opportunities is focused on the 4–5 km MSL layer, as the 4.75–5.85 km MSL layer has an extremely low frequency of potential opportunities (not shown).

Western Area

The monthly frequencies meeting the temperature and LWC criteria, shown in Figure 3.44, illustrate that while the airborne opportunities are fewer overall than ground, they extend the seedable portion of the year beginning in early fall into early summer, as opposed to being primarily in the November–April months as in the ground-seeding layer. In fact, using the full year (October–September) as opposed to the November–April subset nearly doubles the total number of seeding opportunities in a given year (Figure 3.45 and Figure 3.46). Note that these figures are showing the total number of seedable hours as opposed to the fraction of hours seedable within the period of study (previously shown in the ground seeding analysis). This was done in order to compare the difference between the airborne seedable hours in the November–April period versus the full year. When these are normalized by precipitation occurring at the Big Sandy SNOTEL site, the frequencies are reduced at about the same rate as in the ground-seeding layer. This indicates that when airborne seeding conditions are met, there is a similar likelihood that it is precipitating at the surface. Since the precipitation in the months outside of November–April may not always be snow, the same normalization by when snow was modeled at the Big Sandy SNOTEL site is included as well. As expected, the periods of precipitation that were snow in the November–April months were nearly identical (see Figure 3.45), however there is a slight (~50 hours) reduction in the frequency of airborne seeding opportunities that occurred annually when snow fell compared to when any precipitation fell (Figure 3.46). This indicates that opening up airborne seeding in this region to months outside of November–April can provide on average 100 additional hours of opportunities to augment snowfall in the Wind River Range. This could possibly extend snowpack augmentation activities into the beginning of the runoff season.

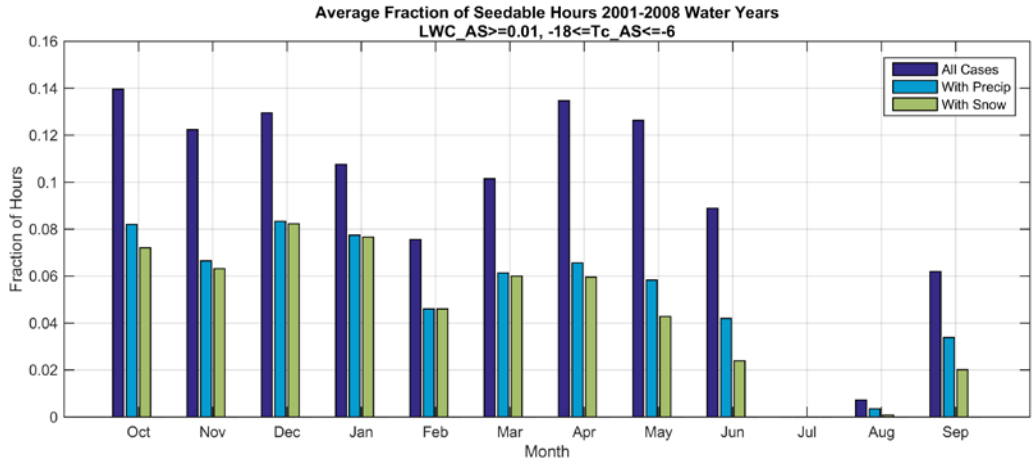

Figure 3.44. Bar chart showing the average fraction of hours in a month that met the temperature and LWC criteria averaged over the western area for airborne seeding (4–5 km MSL; blue) and the same for hours that also had any precipitation (cyan) and snow (green) in the model near the Big Sandy SNOTEL site.

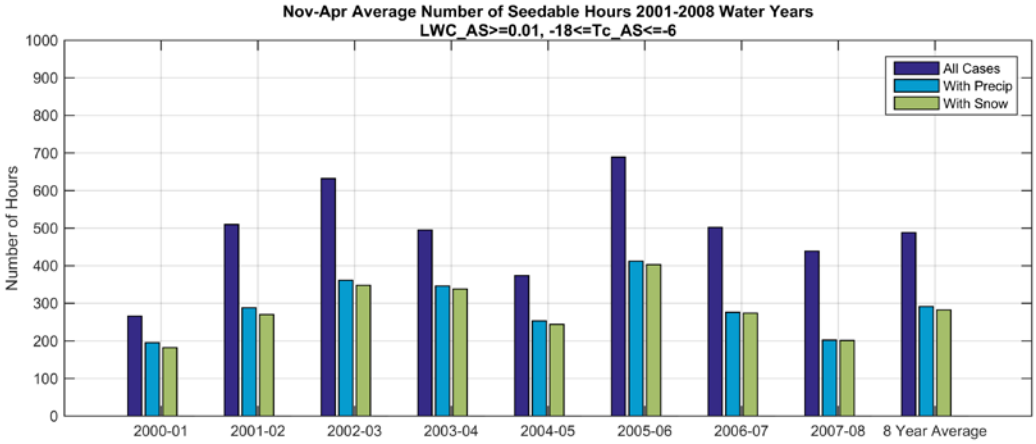

Figure 3.45. Number of hours in the November–April period for each water year meeting the temperature and LWC criteria in the 4–5 km MSL layer over the western area (blue), and the same using the Big Sandy SNOTEL site for precipitation (cyan) and snow (green).

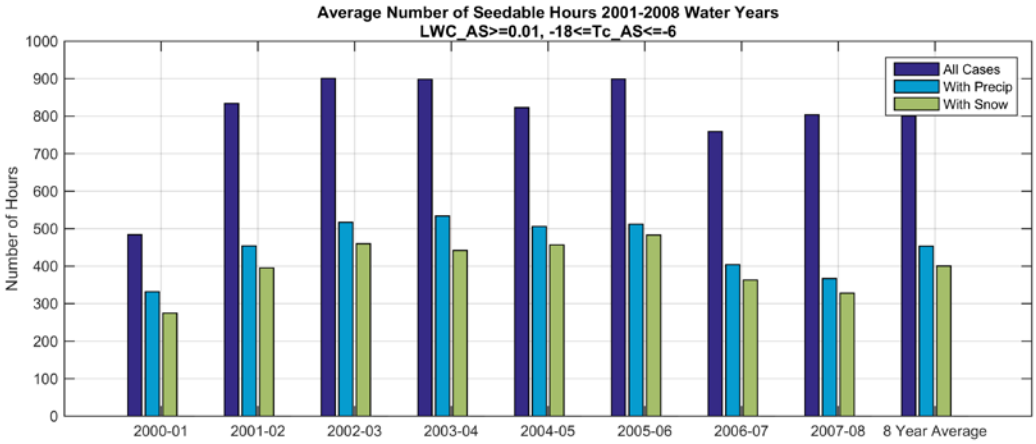

Figure 3.46. As in Figure 3.45, except for the October–September range.

As with the ground-seeding layer, there is month-to-month variability from year-to-year in the number of seedable hours (Figure 3.47). It is important to note that including May, June, September, and October provides a substantial increase in number of seedable hours for nearly every season in this period of study.

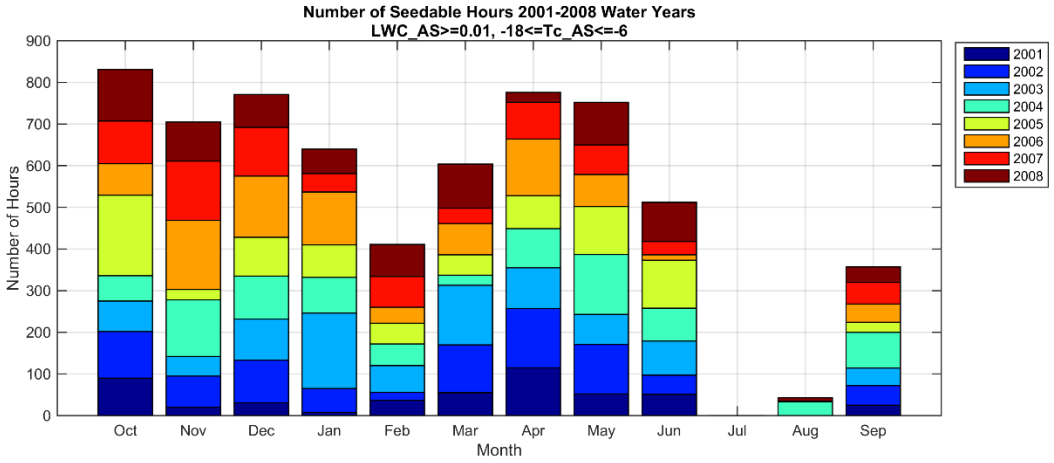

Figure 3.47. As in Figure 3.37, except for airborne seeding (4–5 km MSL).

Eastern Area

Airborne seeding opportunities in the eastern area show a similar monthly distribution as in the western area, with favorable conditions extending into the early summer and fall months. As with ground seeding, the eastern area presents seeding opportunities at about half the rate of the western area.

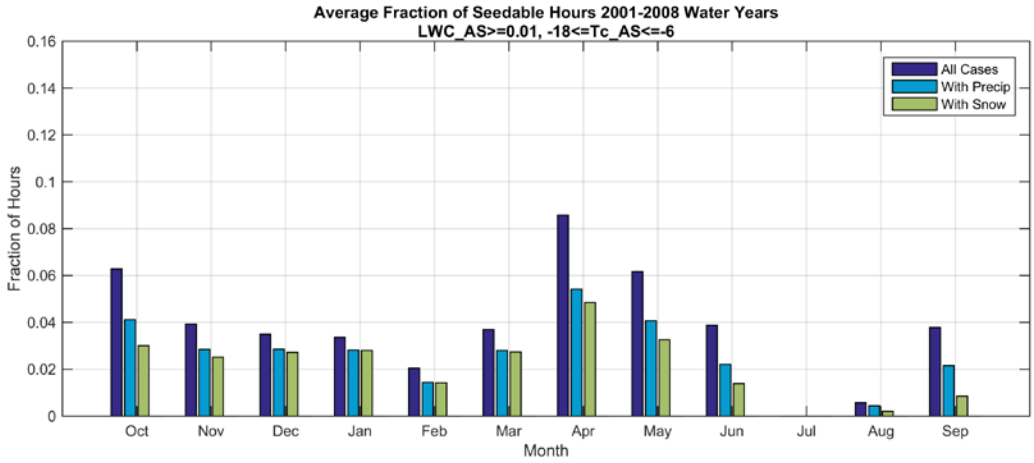

Figure 3.48. As in Figure 3.44, except for the eastern region and the Townsend SNOTEL site.

There is a slight increase overall in the average fraction of seedable hours when including the eastern region with the western region, but as with the ground-seeding layer, the increase is very small (Figure 3.49). Contrary to the ground-seeding layer, where the western and eastern cases were unique due mostly to wind direction, the two regions tend to have simultaneous favorable conditions when considering the airborne-seeding layer.

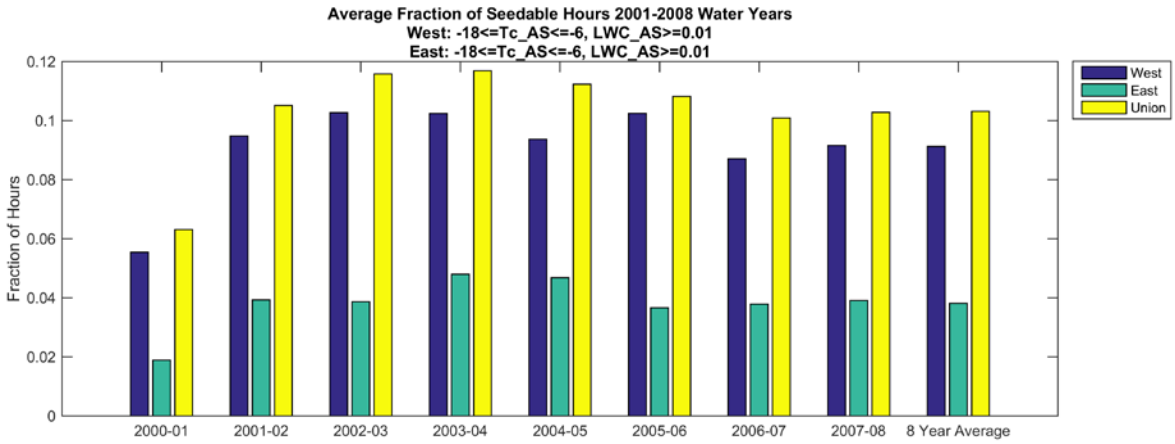

Figure 3.49. As in Figure 3.43, except for the October–September period and airborne seeding (4–5 km MSL).

Ground versus Airborne Seeding Opportunities

Using the area-based model analysis and when considering all of the additional criteria that impact ground seeding opportunities, the airborne seeding opportunities at the 4–5 km MSL layer are fairly different from ground seeding opportunities month-to-month (Figure 3.50). This is presented only for the western area, since including the eastern area provides minimal additional opportunities. The winter months are best for ground-based seeding, while the remainder of the year is favorable for a seeding effect in the airborne layer. Interestingly, the November–April 8-year average fraction of hours is comparable between ground and airborne opportunities (Figure 3.51) with both layers in the 12–14% range; however, the union of ground and airborne opportunities substantially increases the seasonal fraction of hours that are seedable. Based on the 8-year wintertime average it is nearly 20%. This suggests that the many seeding cases do not occur simultaneously in both layers. Similarly, the full year range shows both ground and airborne opportunities occurring 7–9% of the time, and the union at nearly 15% (Figure 3.52). The lower annual fraction of hours corresponds to a higher total number of hours as compared to the November–April subset (recall Figure 3.45 and Figure 3.46). Thus, a program that operates over the full year and includes both ground and airborne seeding options would see the greatest frequency of seeding opportunities.

As mentioned earlier, a higher airborne layer at 4.75–5.85 km MSL was also assessed, but has much less potential for airborne seeding given low LWC and temperatures frequently colder than −18°C. However, there are substantially more opportunities in the summer months at this altitude (Figure 3.53). Thus, a program that operates year-round and includes airborne seeding may see some benefit from including this higher layer as well. If the program is restricted to wintertime months only, the 4.75–5.85 km MSL layer would provide no benefit.

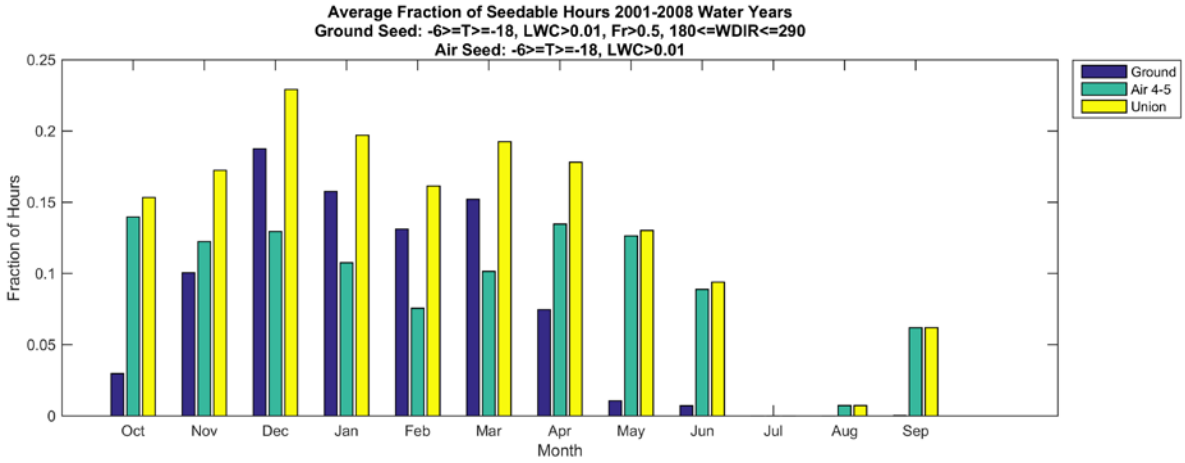

Figure 3.50. Ground (0–1 km AGL; blue) versus airborne (4–5 km MSL; green) seeding opportunities by month (fraction of hours in the month that meet the designated criteria, listed atop the figure, on average over the 8-year period). The frequency of occurrence of cases from the union of both ground and airborne seeding potential is shown in the yellow bar for each time period.

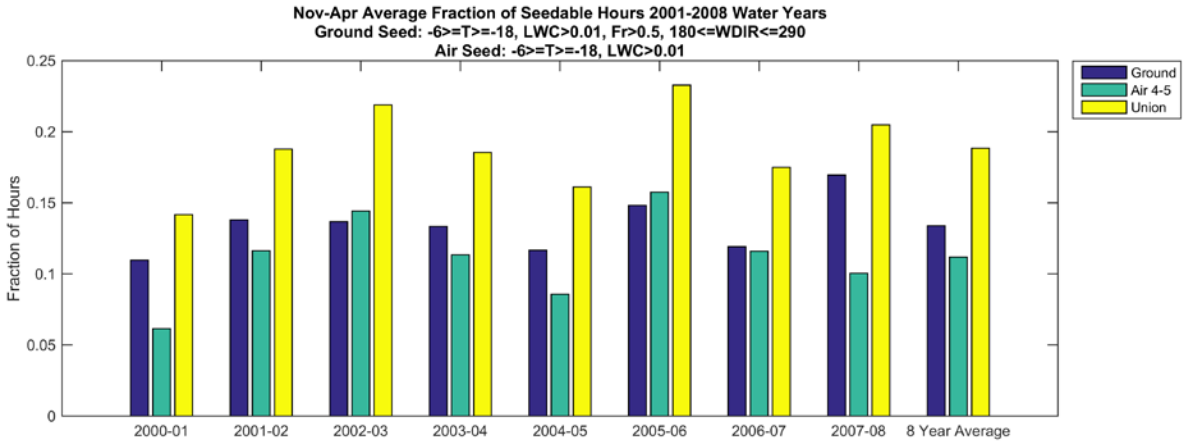

Figure 3.51. Ground (0–1 km AGL; blue) versus airborne (4–5 km MSL; green) seeding opportunities by November–April season (fraction of hours in the season that meet the designated criteria, listed atop the figure), and the 8-year average. The frequency of occurrence of cases from the union of both ground and airborne seeding potential is shown in the yellow bar for each time period.

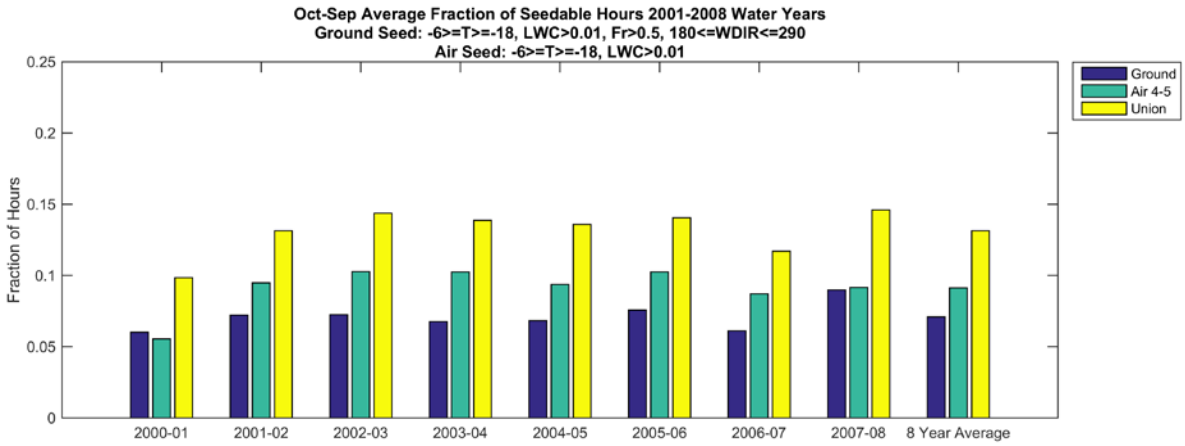

Figure 3.52. As in Figure 3.51, but for the October–September season.

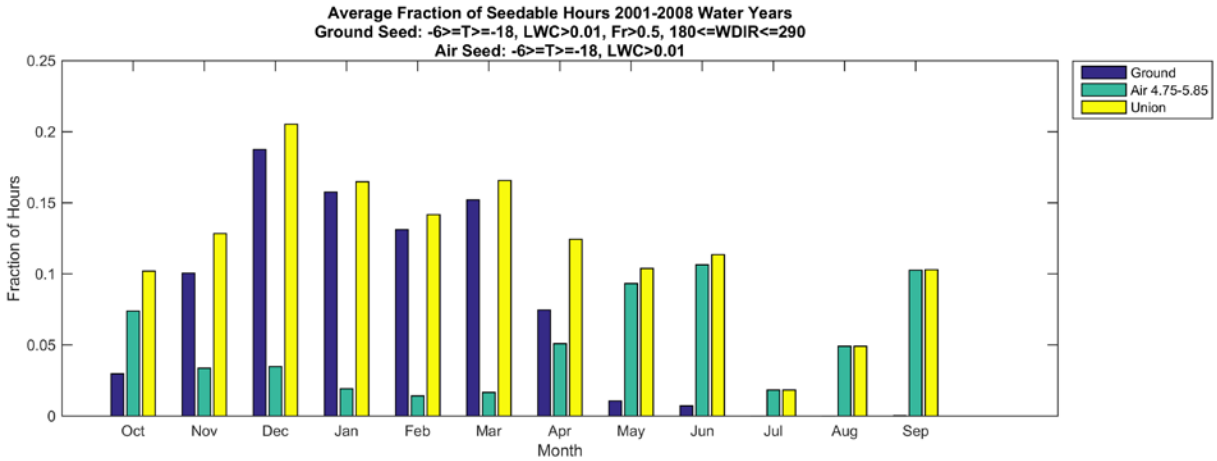

Figure 3.53. As in Figure 3.50, except for airborne seeding from 4.75–5.85 km MSL.

3.4. Seedable Precipitation Calculations

Model precipitation that fell during hours with seedable conditions was totaled throughout the wintertime months and the full water year to determine the total seasonal and annual "seedable precipitation". This can then be compared to the total seasonal precipitation that fell to determine what fraction of the total seasonal precipitation could have been seeded. Note, however, that there may be seedable storms that did not produce precipitation (recall discussion above). Without existing precipitation, it is impossible to quantify the potential impact in a relative sense for those situations. As shown in Table 3.5 and Table 3.6, 68% (46%) of the seasonal (annual) precipitation for the western area was seedable by ground-based seeding, and 42% (41%) by airborne seeding. For ground-based seeding, when including the additional criteria needed to effectively transport AgI over the target area, 56% (38%) of seasonal (annual) precipitation was seedable. Additionally, 17% of the annual precipitation was seedable at the higher airborne level (4.75–5.85 km MSL). The precipitation that fell during seedable periods in the eastern area was substantially less, which is not surprising given the lower relative frequency of seedable periods for ground and airborne seeding as compared to the western area.

An additional precipitation site near the crest of the mountain range was also used for the seasonal and annual seedable precipitation metrics since the model indicated that the maximum precipitation fell along the highest terrain. However, we have no data to verify the model results at this point, or any other location within the modeled precipitation maximum along the crest. It should be noted, however, that Rasmussen et al. (2014) showed good agreement of model results at multiple height levels in the Colorado Rockies, suggesting that the model estimates at higher levels in the Wind Rivers may be reliable.

The results based upon the precipitation totals from the higher terrain portion of the Wind River Range may be more representative than lower elevation SNOTEL sites. The results suggest that total seedable precipitation from this site was generally higher than the lower-elevation SNOTEL site calculations for ground and airborne seeding criteria, and for both seasonal and annual totals. The one exception is for the more strict ground seeding criteria on the eastern side, which was slightly less than the east side calculations using Townsend SNOTEL. Relative to the total (seasonal or annual) precipitation that fell at the crest site, the results were similar (or slightly lower due to this location experiencing substantially higher precipitation than the lower-elevation sites), which indicates a relatively robust fraction of the total precipitation that is seedable for a given slope and type of seeding.

The results also vary by season, as illustrated for the western area analysis in Table 3.7 and Table 3.8**.** The year-to-year variability reflects the interannual variability in the fraction of seasonal hours that are seedable (recall Figure 3.51 and Figure 3.52).

Table 3.5. Seasonal (November–April) 8-year average simulated total precipitation (mm) compared to the seasonal precipitation that fell during ground-seedable ("GS", 0–1 km AGL) time periods versus airborne-seedable ("AS", 4–5 km MSL) times. The percent of the total seasonal precipitation that was seedable is provided in parentheses next to the absolute seedable precipitation. For ground-seeding potential, both the primary criteria (temperature and LWC only) are compared to the scenario with additional criteria included (wind direction and Froude number).

	Precipitation (mm)			
Region & Precip site	**Season Total**	**GS: T+LWC only**	**GS: T+LWC+WDIR+Fr**	**AS: T+LWC only**
West & Big Sandy	386	262 (68%)	218 (56%)	163 (42%)
West & Crest	566	351 (62%)	307 (54%)	246 (43%)
East & Townsend	344	133 (39%)	45 (13%)	83 (24%)
East & Crest	566	187 (33%)	37 (7%)	128 (23%)

Table 3.6. As in Table 3.5, but for the full October–September period, and including the higher airborne layer ("ASH", 4.75–5.85 km MSL).

	Precipitation (mm)				
Region & Precip site	**Annual Total**	**GS: T+LWC only**	**GS: T+LWC+WDIR+Fr**	**AS: T+LWC only**	**ASH: T+LWC only**
West & Big Sandy	613	282 (46%)	233 (38%)	252 (41%)	107 (17%)
West & Crest	977	372 (38%)	322 (33%)	393 (40%)	212 (22%)
East & Townsend	652	177 (27%)	78 (12%)	161 (25%)	86 (13%)
East & Crest	977	222 (23%)	62 (6%)	206 (21%)	111 (11%)

Table 3.7. Seasonal (November–April) total precipitation (mm) for each simulated water year compared to the seasonal precipitation that fell during ground-seedable ("GS", 0–1 km AGL) time periods versus airborne-seedable ("AS", 4–5 km MSL) times based on the western area seeding conditions and Big Sandy precipitation site analysis. The percent of the total seasonal precipitation that was seedable is provided in parentheses next to the absolute seedable precipitation. For ground-seeding potential, both the primary criteria (temperature and LWC only) are compared to the scenario with additional criteria included (wind direction and Froude number).

	Precipitation (mm)			
Water Year	**Season Total**	**GS: T+LWC only**	**GS: T+LWC+WDIR+Fr**	**AS: T+LWC only**
2001	288	174 (60%)	123 (43%)	77 (27%)
2002	316	208 (66%)	178 (56%)	120 (38%)
2003	360	240 (67%)	210 (58%)	136 (38%)
2004	345	246 (71%)	207 (60%)	154 (45%)
2005	401	291 (73%)	230 (57%)	170 (42%)
2006	563	389 (69%)	335 (60%)	305 (54%)
2007	399	255 (64%)	216 (54%)	204 (51%)
2008	412	294 (71%)	247 (60%)	137 (33%)

Table 3.8. As in Table 3.7, but for the full October–September period, and including the higher airborne layer ("ASH", 4.75–5.85 km MSL).

	Precipitation (mm)				
Water Year	**Annual Total**	**GS: T+LWC only**	**GS: T+LWC+WDIR+Fr**	**AS: T+LWC only**	**ASH: T+LWC only**
2001	455	196 (43%)	142 (31%)	119 (26%)	41 (9%)
2002	519	243 (47%)	206 (40%)	209 (40%)	63 (12%)
2003	544	250 (46%)	213 (39%)	197 (36%)	76 (14%)
2004	584	250 (43%)	209 (36%)	233 (40%)	122 (21%)
2005	752	339 (45%)	270 (36%)	365 (49%)	158 (21%)
2006	746	406 (54%)	345 (46%)	377 (51%)	177 (24%)
2007	648	258 (40%)	217 (33%)	266 (41%)	112 (17%)
2008	658	311 (47%)	260 (40%)	250 (38%)	111 (17%)

3.5. Summary

The typical wind regimes were westerly to northwesterly, with some southwesterly events, as well as some easterly events on the eastern slopes of the Wind River Range. However, the spatial mapping analysis revealed that LWC is infrequently located on the eastern slopes of the Wind River Range, and therefore the most frequent seeding opportunities were on the western slopes of the Range.

For the eight-year period analyzed, SNOTEL data showed that the November–April precipitation brings about a half, if not a little more, of the annual precipitation to the Wind River Range region. The model indicated that the precipitation is 20 to 100% higher at the crest as compared to the locations of the SNOTEL sites, but this is difficult to confirm without observational data at those higher elevations. Confirmation of this result would require deployment of additional snow gauges along the crest line. The analysis showed high correlations between nearby SNOTEL sites on the same side of the Wind River Range, while sites on the opposite sides of the Range had weaker correlations. This suggests that precipitation often does not fall on both sides of the Range equally in a given storm or that precipitation on each side of the Range may result from different storm systems. At several SNOTEL sites the model compared quite well with the observations, however aside from that there was a general tendency for the model to overestimate precipitation. This tendency may be related to the model's slightly wet bias, tendency to have stronger wind, and/or slightly different wind direction, as revealed by comparing with the Riverton soundings.

Based on 0–1 km AGL average temperature and LWC criteria, ground seeding had more frequent opportunities than airborne during the November–April wintertime period. When considering the additional criteria for ground-based seeding (wind direction and stability for transporting ground-released AgI into the targeted clouds), airborne seeding potential

at 4–5 km MSL had similar frequencies as ground seeding, with some overlap in the cases between the two layers. A combined airborne and ground program could yield roughly 45% more cases per winter season relative to a ground-based program alone. Nonetheless, from a logistical perspective it is less likely that all airborne "seedable" hours can be seeded, especially with a single aircraft operation, given limited flight on station times. Airborne seeding potential at 4.75–5.85 km MSL was shown to be less feasible with quite low frequencies during the winter months.

The analysis indicated that airborne seeding would be possible outside of the November–April period, and therefore the frequency of seeding opportunities was also evaluated over the full year. The full year analysis was also normalized for when snow occurred in the mountains, and indicated that airborne seeding year-round can provide on average 100 additional hours of opportunities to augment snowfall beyond the number of seedable hours when snow occurred in the November–April period. This suggests the possibility to extend snowpack augmentation activities into the beginning of the runoff season.

Approximately half the time when cloud seeding conditions were present, precipitation occurred over the Wind River Range. This indicates there are some situations with very low precipitation efficiency in which cloud seeding could have potential benefits. Roughly half of the precipitation that fell in a given season was seedable based on ground-seeding criteria being met. Slightly less than half of the precipitation that fell in a given winter season was seedable by airborne seeding.

4. Task 3: Cloud Seeding Modeling

The goal of this task was to quantify the potential impact of cloud seeding on the distribution and amount of precipitation in winter storms by adapting the NCAR cloud seeding forecast system for the Wind River Range to allow the system to be used as a decision support tool for cloud seeding operations in this region.

There were four main efforts conducted as part of this task:

- The RT-FDDA forecast system was set up and run in real time during the 2014-2015 Wind River Range cloud seeding program to provide daily forecasts to assist with operational case-calling decisions.
- The NCAR cloud seeding forecast system was adapted into the RT-FDDA model, tailored for the Wind River Range and run retrospectively for the 2014–2015 season.
- The RT-FDDA model forecasts were compared to observations to evaluate the overall model performance.
- The NCAR cloud seeding forecast system retrospective seasonal results were analyzed.

4.1. Real-time Forecast Model

The WRF model was run in the RT-FDDA modeling framework during the 2014–2015 winter season. This model provided 24-hour forecasts of winds, temperature, liquid water content, and precipitation to aid the forecasters identify seeding opportunities during the operational Wind River Range cloud seeding program. The components of this model are briefly described below, followed by a detailed description of how this model was set up to provide the 2014–2015 real-time forecasts.

4.1.1. WRF Model Description

The WRF numerical modeling system (Klemp et al. 2003, Skamarock 2004, Mikalakes et al. 2004, Barker et al. 2004, Chen and Dudhia 2000) was developed through a collaborative community effort led by NCAR. Key features that made this an excellent system for numerical modeling efforts in this project include being:

- A community model, freely available.
- Characterized by improved numerical stability over steep topography.
- Relatively easy to implement on distributed-memory computer systems.
- Able to modify the physics in the model code to simulate the dispersion and activation of AgI seeding material within the cloud (see Section 3.6.4) and the subsequent microphysical responses leading to precipitation

The WRF model is one of the most widely used public-domain prognostic models in the atmospheric science community. This model was designed to improve forecast quality and investigate meteorological features across scales from turbulence within clouds to global circulations. A number of options are available for boundary layer schemes, cloud and precipitation treatments, and radiative transfer. In-depth descriptions of WRF can be found in published documentation (e.g., Skamarock et al. 2008).

The WRF modeling system is designed around an Eulerian mass coordinate system. It is a fully compressible, nonhydrostatic model with a modified terrain-following (hydrostatic) vertical coordinate to minimize spurious wave activity within the model domain (Skamarock 2004). The numerics are significantly improved over many of the current mesoscale models. The developers determined that using a third order Runga-Kutta solver rather than the leap-frog scheme implemented in the Penn State-NCAR mesoscale model (MM5) and Colorado State Regional Atmospheric Modeling System (RAMS) models would allow for longer time steps, greater numerical stability, and better handling of steep topography. The dynamics include complete Coriolis and curvature terms to facilitate calculations on scales of meters to thousands of kilometers. Second to sixth order advection schemes in both the vertical and horizontal directions are available and scalar variables are conserved. WRF model version 3.4 supports a variety of capabilities, including: real-data and idealized simulations, various lateral boundary conditions, one-way and two-way nesting, and full physics options. Currently, several physics components have been included in WRF, including microphysics, cumulus parameterization, long and short wave radiation, boundary layer turbulence, surface layer, land-surface parameterization, and sub-grid scale diffusion.

There are 21 microphysics packages provided in the current version of WRF. These range from simple warm rain schemes (e.g., Kessler 1969) to moderately sophisticated single-moment schemes that predict the mass of five to six mixed-phase hydrometeor species (e.g., WRF Single Moment 5 and 6 schemes) to more sophisticated multi-moment schemes that predict the mass and number concentration of five to six mixed-phase hydrometer species (e.g., Morrison or Milbrandt schemes; Hong and Pan 1996, Milbrandt and Yau 2005a,b). The Thompson (2004, 2008) scheme is a hybrid parameterization that prognoses two moments of the rain and ice species, while maintaining single-moment prognostic variables for cloud, snow, and graupel species. The hybrid nature of this scheme allows it to run very efficiently, and as such as been widely utilized for real-time forecasting applications. Moreover, this scheme has been shown to perform very well in simulating orographic precipitation (Ikeda et al. 2010, Rasmussen et al. 2011).

4.1.2. RT-FDDA Description

The RT-FDDA system, based on the WRF model, was used in operations to guide forecasters on expected conditions specific to seeding criteria, particularly concerning the existence and persistence of SLW. The RT-FDDA system employs the Advanced Research WRF dynamics core, which is fully compressible and nonhydrostatic with a terrain-following hydrostatic-pressure vertical coordinate (http://www2.mmm.ucar.edu/wrf/users/). The four dimensional data assimilation system employs the Newtonian relaxation based observational nudging technology to continuously assimilate a variety of conventional and non-conventional observation data including: 1) METAR surface observations; 2) MesoWest surface observations; 3) ship/buoy observations; 4) local surface observations; 5) NWS and site rawinsonde observations; 6) NOAA and site vertical profiler observations, 7) National Environmental Satellite, Data, and Information Service (NESDIS) satellite derived winds; and 8) Aircraft Communications Addressing and Reporting System (ACARS) commercial aircraft data (see Figure 4.1). The system was initialized with the Global Forecast System (GFS) forecasting products.

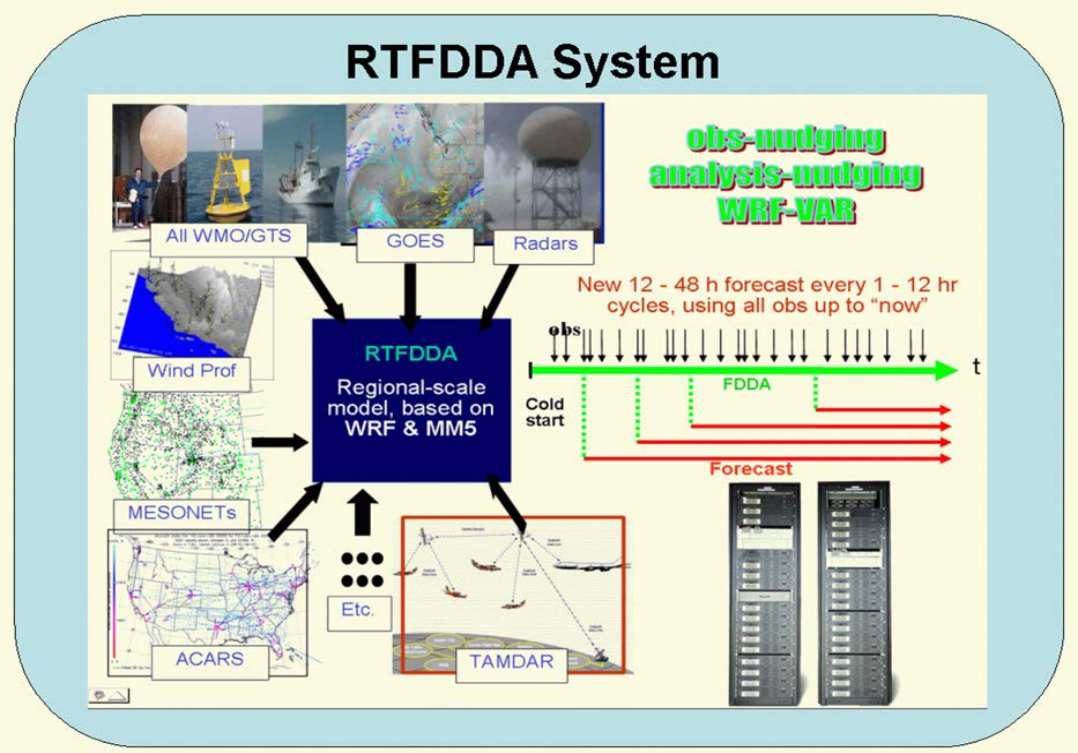

Figure 4.1. Graphical depiction of the RT-FDDA modeling system illustrating the variety of observational data that is assimilated into the forecast system. The WWMPP uses the WRF version of the system to drive the forecast.

The physics parameterizations used include the Thompson bulk cloud microphysics scheme (Thompson et al. 2008), the Yonsei University (YSU) planetary boundary layer (PBL) scheme (Hong et al. 2006), the Monin-Obukhov surface layer scheme (Janjic 1996), the Noah land surface model (Chen and Dudhia 2001), and the Rapid Radiative Transfer Model (RRTM) longwave (Mlawer et al. 1997) and Dudhia shortwave (Dudhia 1989) radiation schemes.

4.1.3. Model set up for real-time 2014-2015 forecasts

The WRF RT-FDDA modeling system used for this project follows the general RT-FDDA procedures shown in Figure 4.1 with similar parameters from the WWMPP. In particular, the RT-FDDA model was set up using WRF version 3.1 to:

- simulate three nested interacting domains as shown in Figure 4.2, consisting of an 18-km grid outer domain (150 x 120 grid points), a 6-km grid domain inside the outer domain (178 x 118 grid points), and a 2-km inner grid domain inside the 6-km grid (238 x 193 grid points) with all domains having 37 vertical levels topped at 50 hPa;
- perform 8 analysis/forecast cycles each day with a cold start at 17 UTC of each Tuesday;

- perform 3-hour observation input and nudging of initial conditions; and
- produce 24-hour forecasts.

Several display features (maps, cross-sections, site locations, etc.) have been customized for this project, including calculating and displaying plume trajectories from individual seeding generators as they proceed towards the target region. A website was dedicated to providing the WRF RT-FDDA model output for forecasters and researchers during the operational seeding season (http://www.ral.ucar.edu/cgi-bin/ugui_wyo?range=wyoming).

The RT-FDDA model forecast system was run between 15 November 2014 and 15 April 2015 to provide 24-hour forecasts tailored for the Wind River Range operational cloud seeding program. WMI forecasters utilized the model data provided on the website (linked above) as part of the forecasting process for identifying cloud seeding opportunities.

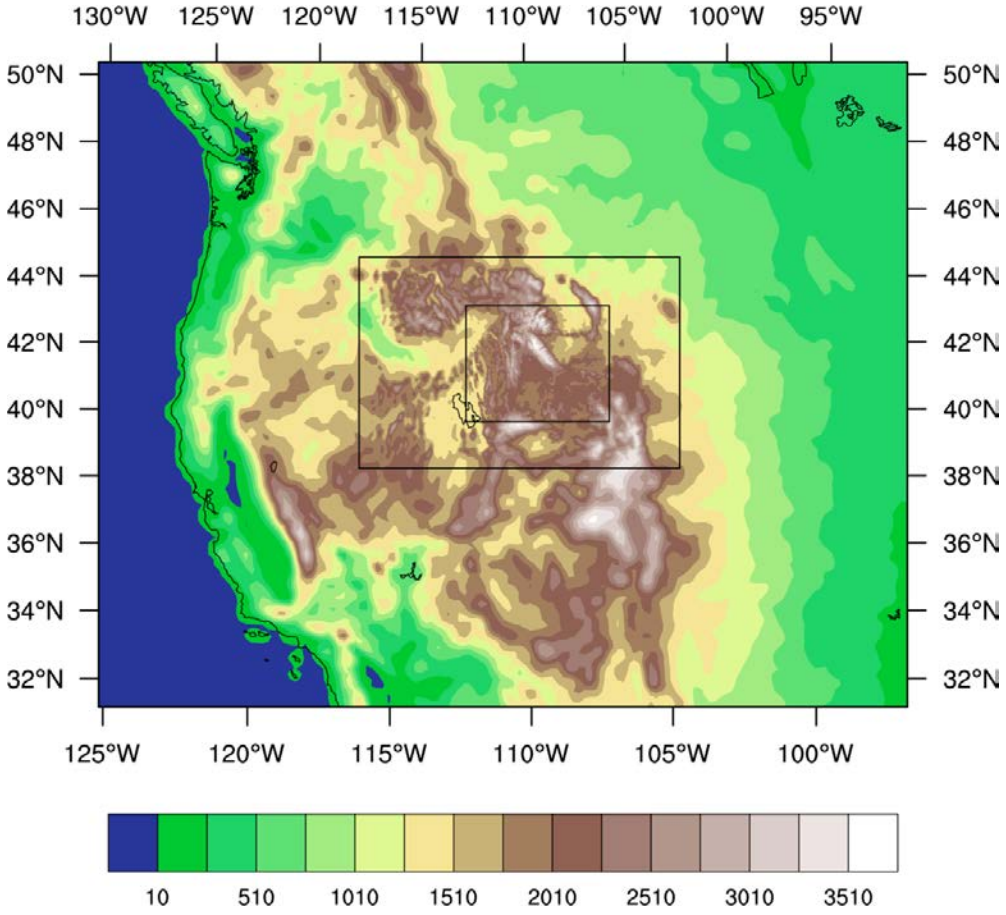

Figure 4.2. Terrain map (elevation color shaded in meters) of the area included in the RT-FDDA outer domain with the location and sizes of the inner domains overlaid in black. The inner most 2-km resolution domain includes the Wind River Range in middle.

4.2. Seeding Forecast Model Development

4.2.1. Overview of system

The NCAR Cloud Seeding Forecast System developed for this project consists of three components: 1) the RT-FDDA WRF forecast model used to perform control and seeding forecasts, 2) the AgI cloud seeding parameterization implemented in the Thompson microphysics scheme simulating the interactions between seeding material and clouds in seeding forecasts, and 3) a cloud seeding case-calling algorithm that determines the suitable seeding technique, location, and timing to be simulated in seeding forecasts.

The general workflow of the cloud seeding forecast system follows these steps:

1) A regular 24-hour forecast is performed by the WRF RT-FDDA forecast model with hourly outputs ("the control forecast").
2) The case-calling algorithm then scans the control forecast output files to identify when, and how many, ground-based and/or airborne seeding cases should be called based on the forecast conditions.
3) Once seeding cases are determined by the case-calling algorithm, a 24-hour "seeding forecast" is launched using the same initial and boundary conditions as the control forecast, while simulating seeding using the AgI cloud seeding parameterization.
4) If the case-calling algorithm did not call any seeding cases, no additional forecasts are run.

This process is repeated for each new control forecast that is simulated in the subsequent cycles. The current experimental cloud seeding forecast system runs with a 6-hour cycle.

4.2.2. Description of seeding parameterization

The AgI cloud seeding parameterization is documented in Xue et al. (2013a). Here we provide a brief description of the coupled model. Figure 4.3 shows the various interactions between AgI particles and hydrometeors in the coupled scheme. The AgI cloud seeding parameterization predicts the AgI nucleation ability of four modes (deposition, condensation-freezing, contact-freezing and immersion-freezing) as functions of temperature, saturation ratios with respect to ice and water, and scavenging of AgI particles by drops and ice crystals following DeMott (1995) and Meyers et al. (1995). The collection of AgI particles by drops and ice through Brownian diffusion, turbulent diffusion, and phoretic effects are parameterized following Caro et al. (2004). In addition to scavenging processes, AgI particles can activate cloud droplets as cloud condensation nuclei (CCN) as they contain a salt complex. The fraction of AgI acting as CCN is a function of water supersaturation ratio. A point source of AgI particles is described by a release rate in kilograms per second and a grid point that indicates the source location. The locations can be fixed points to represent ground-based generators, or they can dynamically change during a simulation to represent a seeding aircraft. The AgI particles are assumed to have a single mode lognormal size distribution. The mean diameter and the geometric standard deviation can be prescribed to match the laboratory measurements of the AgI solution. By tracking the conserved AgI number and mass within different hydrometeors, AgI "precipitation" (wet deposition) is also calculated.

The cloud seeding modeling framework has been used to investigate the microphysical chain of events of glaciogenic seeding and its effect on wintertime orographic clouds under both idealized and realistic conditions (Xue et al. 2013a,b, 2014, 2015a,b). The results indicate that the cloud seeding parameterization can realistically simulate the processes associated with seeding events.

The AgI cloud seeding parameterization was implemented in the Thompson microphysics scheme (Thompson et al. 2008) based on its ability to correctly simulate the SLW in mixed-phase clouds (developed for aircraft icing forecasts). It was shown to accurately estimate snowfall in a high-resolution (4 km grid spacing) eight-year regional climate simulation of orographic snowfall over the Colorado Headwaters region (Ikeda et al. 2010, Rasmussen et al. 2011). These 8-year high-resolution model simulations simulated LWP that agreed with radiometer observations very well through an entire winter season (Ritzman et al. 2015).

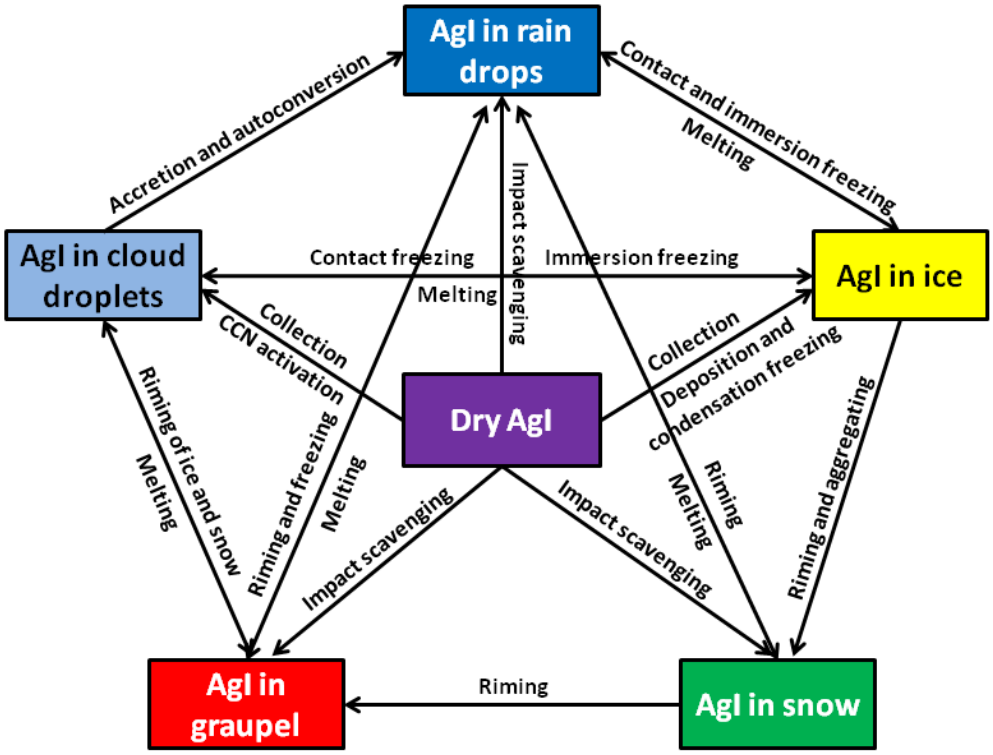

Figure 4.3. AgI-cloud interactions in the seeding model.

4.2.3. Description of the Cloud Seeding Case-calling Algorithm

A seeding case-calling algorithm was developed to enable the real-time cloud seeding forecast system to call seeding cases automatically. The principles of this algorithm are based upon assessing the presence of the basic conditions required for a positive cloud seeding effect. These basic conditions have been categorized into two sets of criteria: microphysical and dispersion. If both sets of criteria were met for either a ground or airborne case for the given target region, a process to define the case times was called. This entire process, which is further explained in the following sections, was executed to determine the suitability of both ground and airborne seeding separately for each of two target regions (west slope and east slope; Figure 4.4).

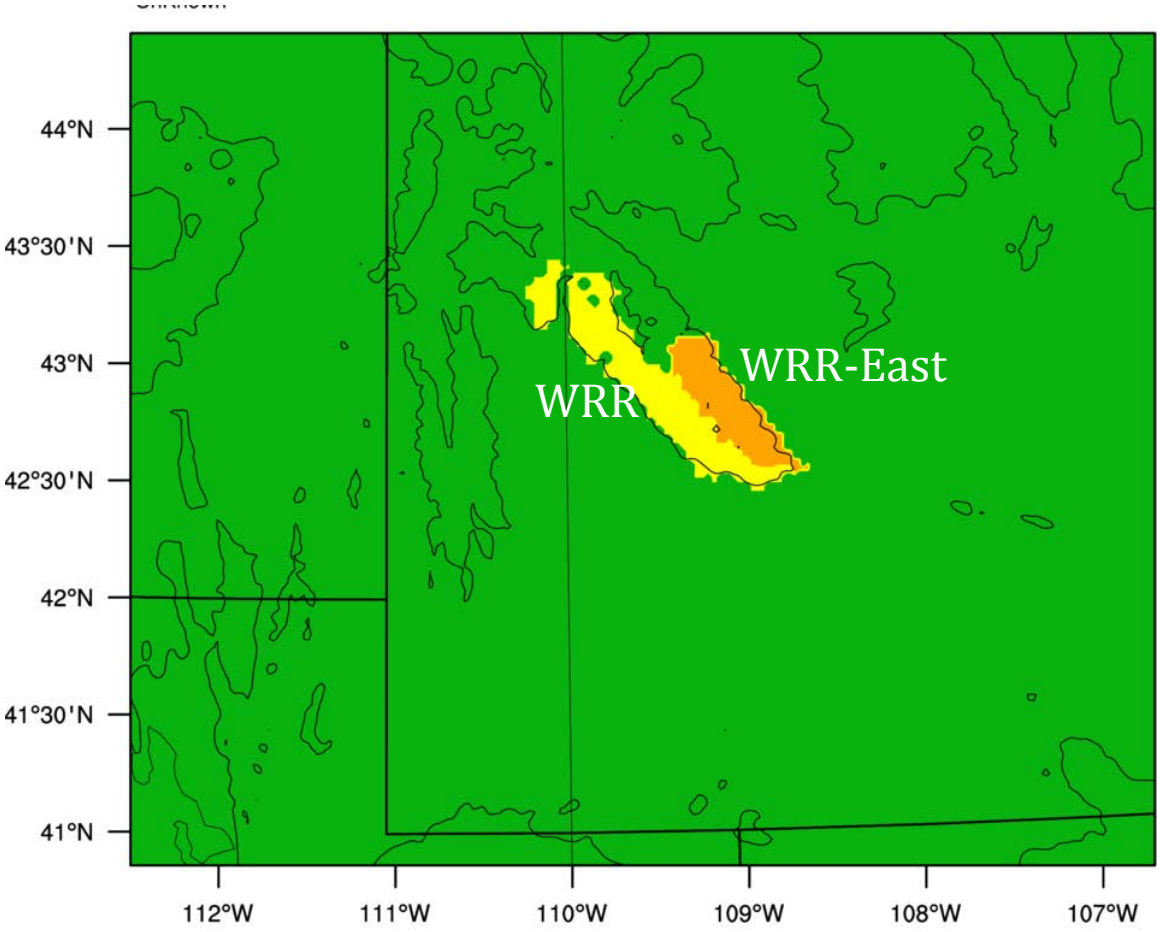

Figure 4.4. Map of seeding condition assessment areas for the Wind River Range: yellow for the west slope (WRR) and orange for the east slope area (WRR-East). Topographical contours are in thin black and state borders are in thick black lines.

Microphysical Criteria

The microphysical criteria represent all of the physical conditions inside the cloud that are needed for a positive cloud seeding effect if AgI were introduced into that cloud. Namely, the presence of SLW and/or supersaturation with respect to ice (S_i), and an appropriate temperature (T) for AgI nucleation. Moreover, the liquid water to total condensate ratio (LWR) is also used as an indication of the liquid water production rate in a mixed-phase environment. If this ratio is close to unity, almost all of the condensate is water, which will be an ideal condition for seeding if all other criteria are met. When it is close to zero, the ice particles dominate the environment.

The algorithm assesses conditions over the prescribed target regions using the output from the control forecast run following the flowchart depicted in Figure 4.5. The conditions are slightly different for ground-based versus airborne seeding, given that airborne AgI is released above the surface and thus optimal microphysical conditions would be above the surface, whereas ground-based criteria assess the microphysical conditions closer to the ground surface. Therefore, ground-based seeding criteria are assessed below 1000 m AGL and between 3500 and 4500 MSL or 4000 and 5000 m MSL for airborne seeding. Each of

the microphysical criteria are assessed by determining the area of each target region that meets each criterion, and then requiring a minimum fraction of that area be met in order for that criterion to be fully satisfied. For example, ground-based seeding cases require that greater than 50% of the target region have LWP greater than 0.01 mm (Figure 4.5). There is also a weighting applied to the microphysical criteria, such that all criteria are mandatory fields except LWP for the microphysical criteria to be determined as sufficient. If the microphysical criteria are met (a score greater than 7), then the algorithm moves on to determine if dispersion criteria are met.

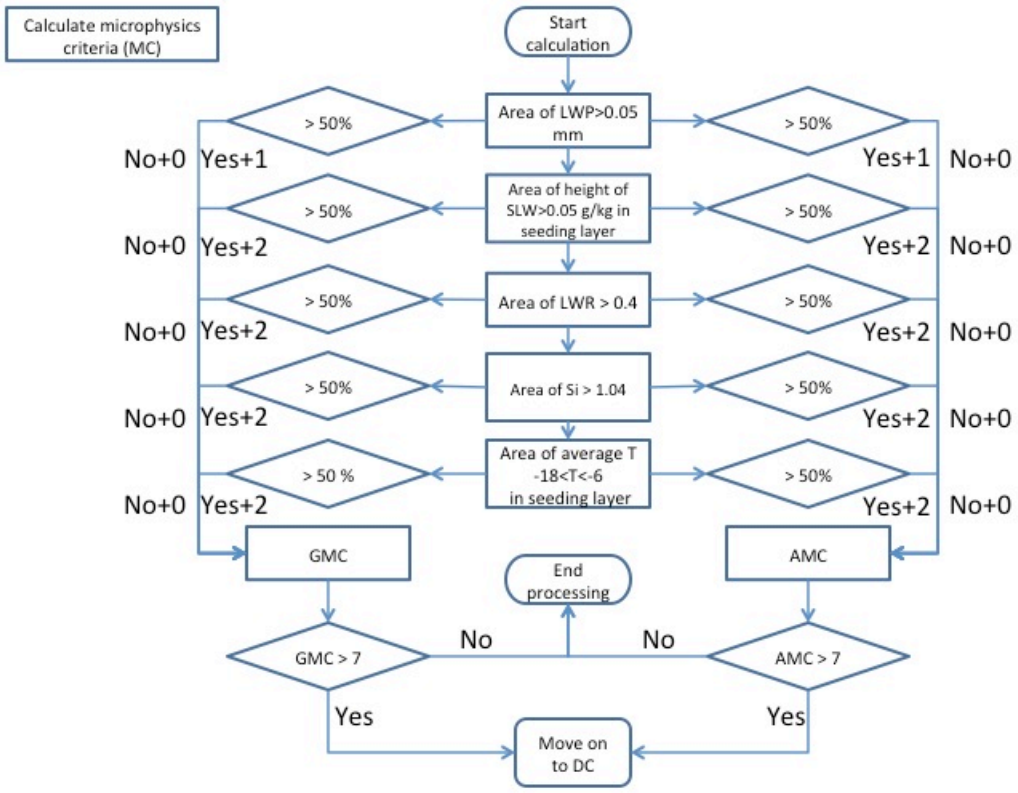

Figure 4.5. Flowchart detailing the seeding case-calling algorithm microphysical criteria. The left side details the ground seeding criteria decision process (for the 0–1 km AGL seeding layer), and the right side details the airborne seeding criteria process (for both the 3.5–4.5 km MSL or 4–5 km MSL seeding layers). GMC is Ground Microphysical Criteria, AMC is Airborne Microphysical Criteria, DC is Dispersion Criteria. The area assessed is defined on map in Figure 4.4.

Dispersion Criteria

The dispersion criteria represents the conditions that would allow the released AgI from either ground or airborne seeding to be transported into the target region that contains the appropriate microphysical criteria for a positive seeding effect. Basic conditions assessed as part of the dispersion criteria are often wind speed and wind direction. In addition for ground seeding, stability parameters should also be assessed to ensure the environment is unstable enough to allow vertical dispersion of the AgI released from the ground. For this

initial implementation of the case-calling algorithm in the Wind River Range, only the microphysical criteria were assessed for ground-based seeding. In a secondary run of the case-calling algorithm, the ground-based dispersion criteria were implemented to determine how many cases were eliminated due to those additional criteria. The ground-based seeding dispersion criteria are detailed in a flowchart in Figure 4.6 and Table 4.1–Table 4.3.

For airborne seeding, wind direction was the only dispersion criterion assessed, which was done by averaging over each target region. For the airborne dispersion (wind direction) criterion to be met, the average wind direction must be between 180 and300 degrees for west slope seeding and 60 to 120 degrees for east slope seeding. .

If the dispersion criteria are met, then the algorithm moves on to define the times for the cases being called. Dispersion criteria are only assessed if the microphysical criteria for a given target region (ground or airborne separately) are met, so once dispersion criteria are met, both sets of basic conditions assessed by the algorithm are considered sufficient for seeding.

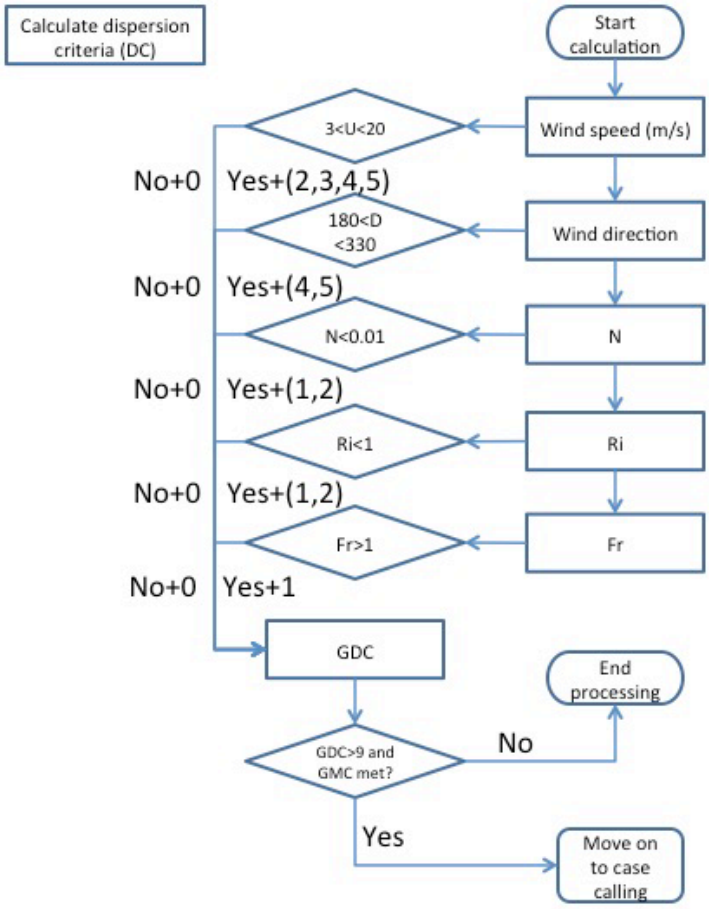

Figure 4.6. Flow chart of the ground seeding dispersion criteria (GDC). The weighting factors for the weighted criteria are detailed in Table 4.1–Table 4.3.

Table 4.1. Wind speed (U) weighting for ground-based dispersion criteria depending on wind speed ranges. There is no weighting factor of 1 assigned for this criterion. Default weighting is zero.

Weighting factor	Average Wind Speed (U) Range (m/s)
2	U < 2 or 16 <= U <20
3	2 <= U < 4 or 13 <= U < 16
4	4 <= U < 7 or 10 <= U < 13
5	7 <= U < 10

Table 4.2. Wind direction (D) weighting for ground-based dispersion criteria depending on wind direction ranges for each target region. There is no weighting factor of 1, 2, or 3 assigned for this criterion. Default weighting is zero.

Weighting factor	WRR	WRR-E
4	180 <= D < 210 or 240 < D <=300	20 < D <= 45 or 90 < D <=115
5	210 <= D <=240	45 <= D <= 90

Table 4.3. Stability parameter weights for ground-based dispersion criteria depending on values of stability indices. Default weighting is zero.

Weighting factor	Stability index range
Brunt Vaisala Frequency (N^2)	
1	4.9e-5 < N^2 <= 1e-4
2	N^2 <= 4.9e-5
Richardson Number (Ri)	
1	0.25 <= Ri < 1
2	Ri < 0.25

Defining the Case Times

Once both microphysical and dispersion criteria are met for a given target region, for either ground or airborne seeding, the algorithm needs to define the time periods the cases should be called for. The strategy for calling cases differs for ground (Figure 4.7–Figure 4.8) versus airborne seeding. The essential process, however, follows a similar method in which at every hourly time step the algorithm assesses whether the microphysical and dispersion criteria (hereafter "core criteria") are met within a moving time window.

For ground-based seeding, there was no limit on the duration of time the ground generators could be run for, however an arbitrary minimum time window was defined as 3 hours. Thus, the algorithm required that within a 3-hour window, two-thirds of the hourly time steps had the core criteria met (Figure 4.7). Once that condition was met, (starting at

hour 3 in the control simulation), the case start time would be defined as the beginning of that current 3-hour window. If conditions continued longer than within that 3-hour window, a longer case would be called because the 3-hour window continued to move forward until the two-thirds rule was not met, at which time it would define the end time of the ground seeding case. Since there was no limit to the duration for a ground seeding case, a case merging strategy was also developed and implemented to avoid short (<2 hour) breaks in the ground seeding cases (Figure 4.8). This strategy starts from the end of the 24-hour period of assessment and works backward to assess if there are any breaks between ground seeding cases of less than 2 hours. If so, it merges those two cases together, and continues backward to the beginning of the forecast assessment period.

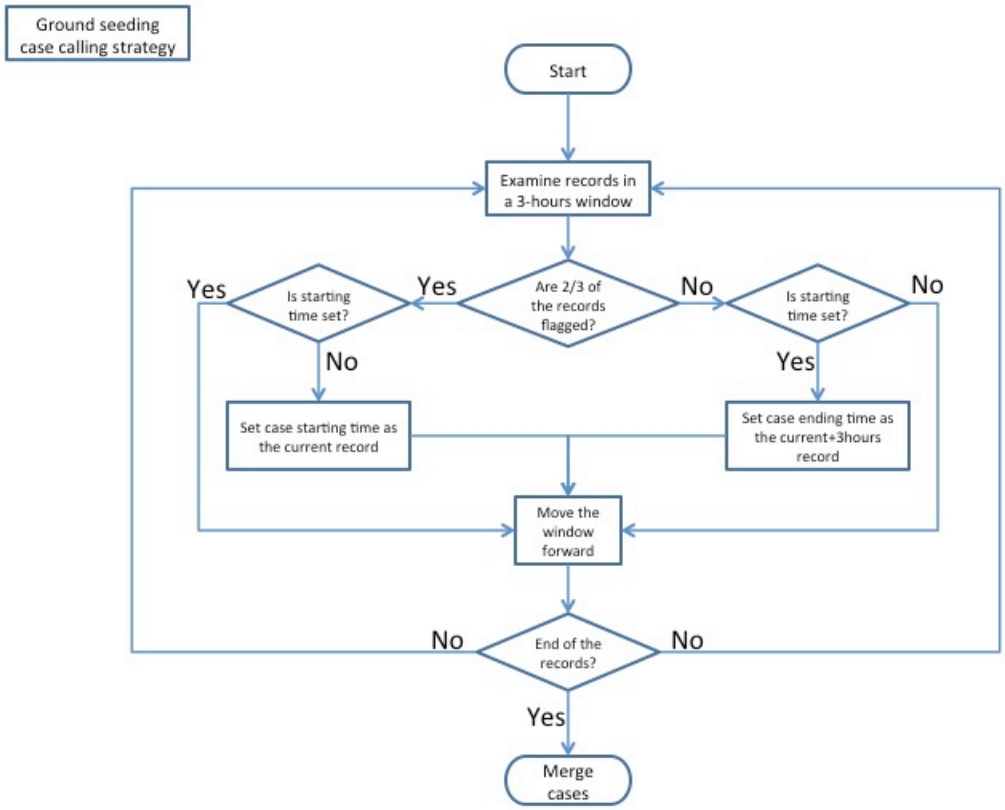

Figure 4.7. Flowchart depicting the ground seeding case calling strategy.

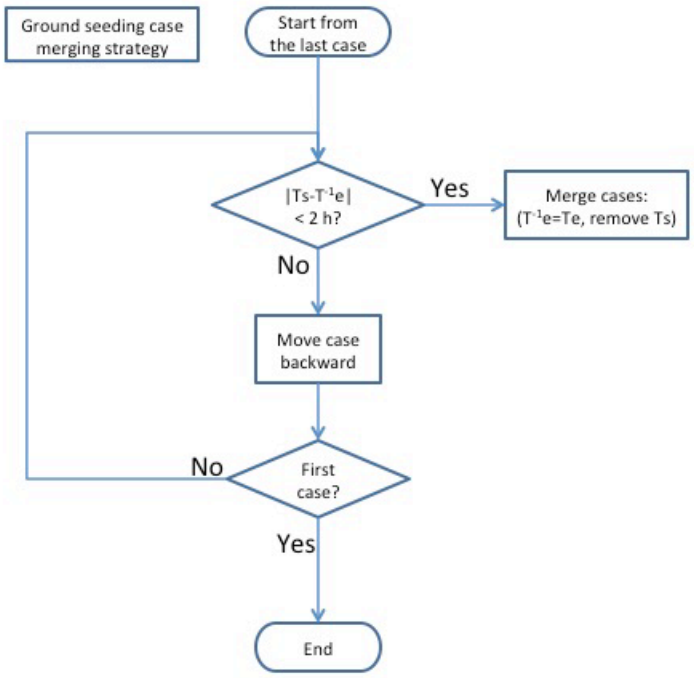

Figure 4.8. Flowchart depicting the ground seeding case merging strategy. Ts is the current case start time, and $T^{-1}e$ is the end time of the previous case.

For airborne seeding, a flight time limit of 2 hours was imposed on the algorithm. The algorithm assesses a broad window of time that airborne seeding is possible (following the ground seeding case calling method shown in Figure 4.7 and Figure 4.8) and then identifies the best 2-hour period within that window to call airborne seeding. The best 2-hour period is determined as having the highest total score from the microphysical criteria.

4.2.4. Model set up for retrospective implementation of seeding forecast system

A dedicated workstation (mizu) was purchased to run the RT-FDDA forecast system exclusively for this project. Mizu consists of one node with 32 cores and 128 GB memory space. A RAID system of 15 TB was mounted to mizu to host most of the model forecast and analysis data. The RT-FDDA system was upgraded for this project to WRF version 3.5.1 as well as changed to utilize the Mellor-Yamada-Janjic (MYJ) PBL scheme (Janjic 2002). This new RT-FDDA WRF v3.5.1 forecast system was run on mizu parallel to the operational version (RT-FDDA WRF v3.1, which ran on a different, older cluster) in real time from 15 November 2014 to 15 April 2015 to test the performance and stability of the new machine. After many tests of different configurations, the new system was set to use 24 cores to perform a 24-hour forecast ("control forecast" without simulated seeding) with a 3-hour cycle. When the seeding forecasts are to be simulated in addition to the control forecasts, the cycle frequency has to be extended to 6 hours to allow both the control and seeding forecasts to finish running before the next cycle begins.

The AgI cloud seeding parameterization, previously run with WRF v3.4.1, was adapted into the RT-FDDA WRF v3.5.1. The case-calling algorithm was also implemented to assess conditions in two areas over the Wind River Range: western (WRR) and eastern (WRR-E) slopes (recall Figure 4.4). The WRR area was designed to evaluate the seeding conditions for the existing generators on the western slope of the Wind River Range while the WRR-E area was evaluated under the upslope easterly wind conditions for the single generator on the eastern side of the Range (Enterprise). The case-calling algorithm evaluated seeding conditions for ground generators, as well as for aircraft seeding at both lower and higher altitudes. However, only the ground-seeding cases determined by the case-calling algorithm were set to trigger the seeding simulations by the RT-FDDA in real time since those are the only existing seeding facilities. The statistics from when the model called airborne seeding cases was only used to evaluate the potential for aircraft seeding in the Wind River Range.

The RT-FDDA forecast system has a 6-hour analysis section which serves as the spin-up for the actual 24-hour forecast. Therefore, the case-calling algorithm scans all the 24 hours of forecast output for appropriate seeding conditions. After the cloud seeding parameterization and the case-calling algorithm were implemented with RT-FDDA, the complete cloud seeding forecast system was tested on mizu in a "real-time" mode with a 6-hour cycle while being run retrospectively for the 2014–2015 season.

From this first retrospective trial of the cloud seeding forecast system, all of the control forecasts were correctly run by the system. The case-calling algorithm ran successfully and identified ground and airborne seeding cases for both the WRR and WRR-E areas. However, the seeding forecasts were not correctly simulated during this first trial. It was determined the problem was due to the fact that the RT-FDDA only cold starts once a week. This means that the model is continuously run for a week in between two cold starts. Therefore, the case-calling algorithm-determined seeding case periods that were originally relative to the 24-hour forecast were not correctly timed in the continuous simulation. The case-calling algorithm and the cloud seeding parameterization were then modified to account for this feature after the first failure of the "real-time" test.

The second trial of the retrospective simulations of all seeding forecasts was successful after modifications to fix the bug identified above were implemented. The case-calling algorithm performance (compared to cases that were actually seeded by the WMI forecasters) and the statistics of case-calling algorithm-determined seeding cases are summarized in Section 4.3.2.

4.3. Model Performance Evaluation

4.3.1. Forecast model evaluation

The WRF RT-FDDA forecast data were evaluated using SNOTEL data, soundings launched at Pinedale, WY (for select days only), and radiometer data collected at Boulder, WY.

Figure 4.9 is a schematic drawing of the WRF RT-FDDA forecast cycles that were run from 14 November 2014 through 15 April 2015. A 24-hour forecast was made from each of the

four forecast cycles starting from 00 UTC each day, producing hourly outputs. To examine the forecast performance, 1–6 hour, 7–12 hour, and 13–18 hour forecasts from each of the four cycles were patched together to form three realizations of 24-hour forecasts (hereafter F1–6, F7–12, and F12–18). By analyzing forecast data from the same lead time in each forecast cycle, the potential impact on forecast performance associated with the length of time from the model initialization time is reduced. The model spin-up period is thought to be ~3 hours. The first couple of hours of the first forecast block (F1–6) are in the spin-up period. However, it will be shown later that there was no substantial difference in the forecast performance between the three forecast blocks.

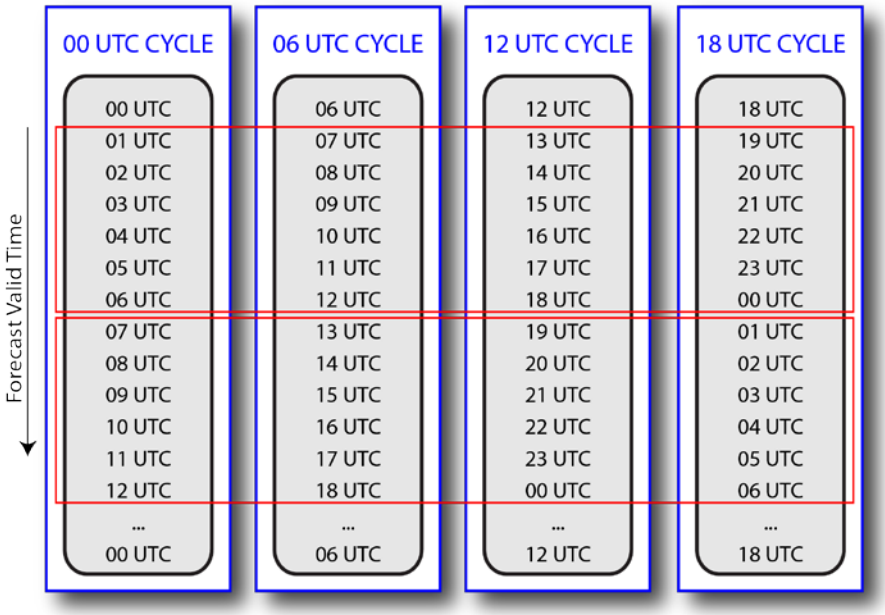

Figure 4.9. A schematic drawing of daily RT-FDDA forecast cycles implemented during the 2014–2015 winter season. Red rectangles indicate two of the three six-hour blocks of RT-FDDA data described in the main text. The upper block is F1–6, and the lower block is for F7–12. It is not shown on the schematic, but the third block immediately follows the second block from hours 13 through 18.

SNOTEL Data Comparison

The WRF RT-FDDA precipitation forecasts were evaluated using daily and seasonal total precipitation from 15 SNOTEL sites in the Wind River Range region (Figure 3.1). The seasonal precipitation accumulation was computed for a period from 15 November 2014 to 15 April 2015.

The RT-FDDA data evaluated in this study are from the innermost nest of the model domain with a horizontal grid spacing of 2 km. The model precipitation at each SNOTEL site was determined by taking an inverse-distance weighted average of grid cell values from the four closest model grid cells to the SNOTEL site. Days were omitted from the evaluation dataset when any of the forecast cycle was missing and therefore prevented the formation of a complete 24-hour forecast. This resulted in 7 days omitted from evaluating the F1–6 and 12 days from the F7–12 and F13–18 hour forecast blocks.

Figure 4.10 shows a spatial distribution of model bias in seasonal precipitation at each SNOTEL site from the second forecast block (F7–12). The model shows a tendency to over-

predict precipitation nearly at all sites except at Gunsight Pass. However, the bias is relatively smaller (<65 mm or <30% of observed amount) at sites on the eastern slopes than those on the western slopes where it was up to 140 mm (or 65%). Similar results were seen using the other two forecast blocks. Note that the model estimate is higher than the SNOTEL data. Since SNOTEL data are impacted by wind undercatch, some degree of model over-estimate is expected.

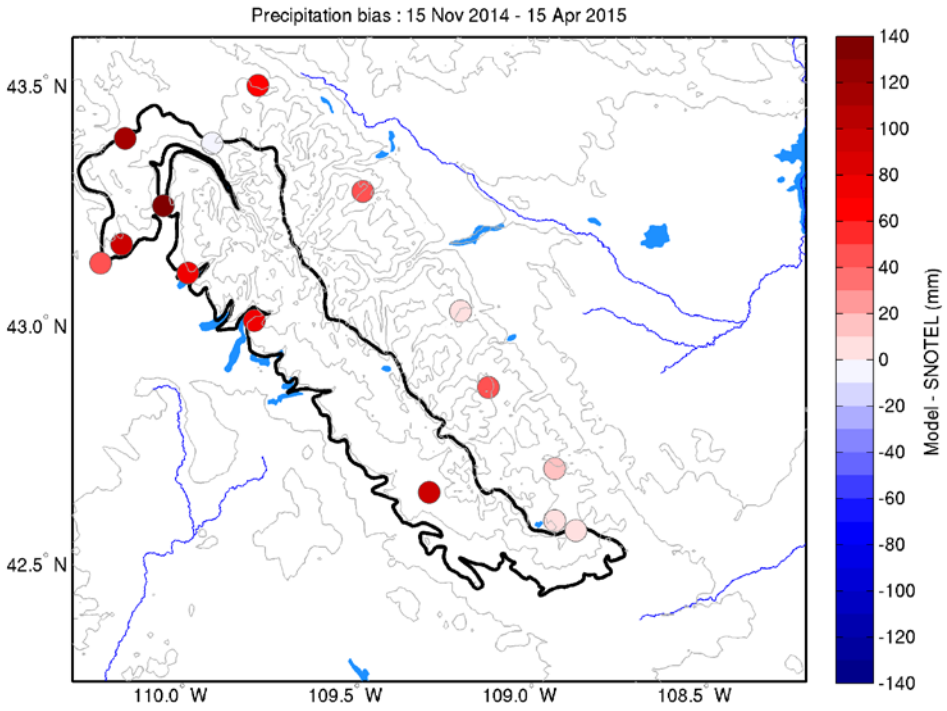

Figure 4.10. Seasonal precipitation bias at SNOTEL sites from 15 November 2014 to 15 April 2015 based on the second forecast block (F7–12).

When the amount of precipitation is averaged over the 15 SNOTEL sites, the seasonal precipitation amount and bias are similar between the three forecast blocks (Table 4.4). The bias indeed suggests an improvement with time (using later forecast blocks), but the correlation coefficient of daily precipitation between the model and observations is the lowest for the third forecast block (note that the difference is not statistically significant).

Table 4.4. Seasonal precipitation from 15 November 2014 to 15 April 2015, seasonal precipitation bias in absolute amount and percentage, and correlation coefficient between the predicted and observed daily precipitation corresponding to each of the three forecast blocks. Values are based on the model and observational data averaged over the 15 SNOTEL sites.

	Seasonal Precipitation (std)		Bias		Daily precipitation corr. coef.
Forecast hours	RT-FDDA (mm)	SNOTEL (mm)	Model – Obs. (mm)	(Mod – Obs)/Obs (%)	
F1–6	261.9 (64.7)	207.4 (45.0)	57.5	27.7	0.80
F7–12	256.4 (59.4)	202.4 (42.9)	54.0	26.7	0.80
F13–18	250.2 (59.7)	201.9 (42.8)	48.3	23.9	0.77

Time history comparisons of precipitation accumulation and daily precipitation show when the discrepancy between the model and observations occurred (Figure 4.11). The model predicted each event fairly well even though the event total amount did not always correspond with the observations. In order to understand the bias in more detail, time series plots from the individual SNOTEL sites (not shown) were examined. They revealed that the model was particularly too aggressive in producing precipitation from some relatively large storms on the western slopes of the Wind River Range, consistent with what was shown in Figure 4.10. The agreement was substantially better for the sites on the eastern slopes in those cases. Storms on 30 November 2014 and 6 January 2015 are a couple of examples of such cases. The bias from these few large storms indeed affected the mean bias, however a substantial overestimate of precipitation by the model also occurred in a weaker storm on 24–25 March 2015.

In some cases, there was very little or no precipitation observed on the western slopes and precipitation was mostly measured on the eastern slopes. However, the model predicted precipitation evenly over both sides of the Range. An example of such a case is illustrated by a storm on 9 April 2015 (last precipitation peak in lower panels of Figure 4.11). The model correctly forecasted precipitation with no significant bias on the eastern slopes, but it generated large snowfall on the western slopes. We will investigate these biases later using the rawinsonde observations from Pinedale.

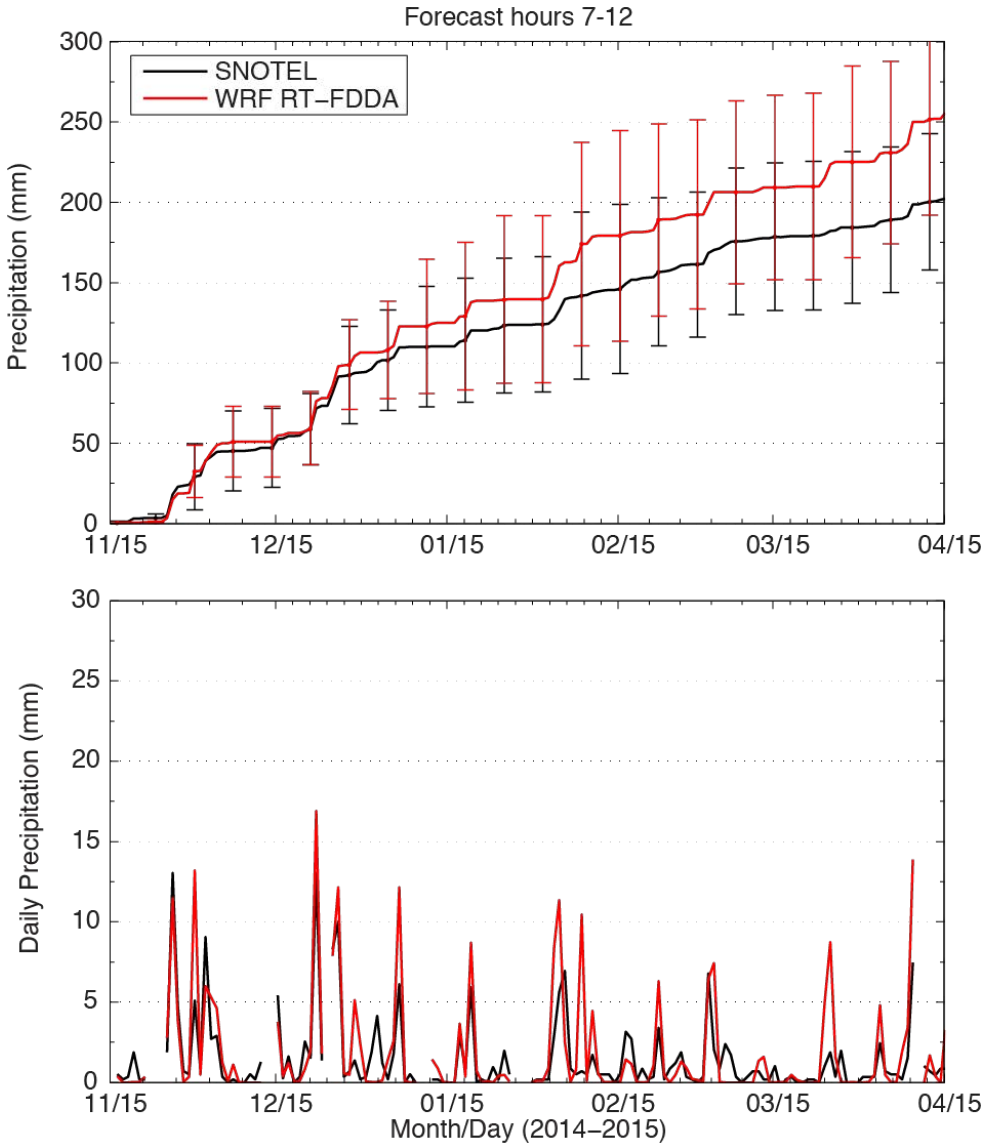

Figure 4.11. Time history of precipitation accumulation (top panels) and daily precipitation (bottom panels) averaged over the 15 SNOTEL sites from the F7–12 RT-FDDA forecasts and observations. The vertical bars in the top panels indicate one standard deviation from the average precipitation.

Pinedale sounding data comparison

To examine the model ability to accurately forecast atmospheric conditions, atmospheric soundings launched from Pinedale were compared to the RT-FDDA forecast. Data values based on the inverse-distance weighted average from four closest grid cell from the sounding site were examined. 18 soundings were launched on precipitating days targeted for cloud seeding operations during the 2014–2015 winter season.

The following quantities were determined from the model and observation data:

- 700 hPa geopotential height
- 700 hPa dry bulb temperature
- 700 hPa dew point temperature

- 700 hPa water vapor mixing ratio
- Precipitable water
- 700 hPa wind speed and direction
- Square of the Brunt-Vaisala frequency

The atmospheric quantities at 700 hPa were found by linear interpolation from the forecast and observational data. Definitions of these quantities are described in Section 3.1.2.

Additionally, the following stability quantities were also calculated and compared against the Pinedale sounding data:

- Froude number
- Richardson number

As previously described in Section 3.1.2, Froude number expresses the ability of oncoming airflow to go over a mountain barrier. The is flow blocked by the barrier when Fr < 1. The flow will freely go over the barrier (unblocked) when Fr > 1. Froude number (Fr) was computed from,

$$Fr = \frac{U/h}{N}$$

where U is the average wind speed (m s^{-1}) perpendicular to the mountain barrier over a depth of h (in m), and N is an average of the Brunt-Vaisala frequency over the same depth (recall Section 3.1.2). In this case, h was 1211 m—the difference between the average elevation of the Wind River Range (3200 – 3600 m) and the elevation at Pinedale (2189 m MSL).

Richardson number indicates dynamic stability. Richardson number is found from

$$Ri = \frac{N^2}{\left(\frac{\partial U}{\partial z}\right)^2 + \left(\frac{\partial V}{\partial z}\right)^2},$$

where N^2 is the square of the Brunt-Vaisala frequency (s^{-2}), z is height (m), and U, and V are zonal and meridional components of wind (m s^{-2}), respectively (AMS Glossary). When Ri is less than the critical Richardson number (~0.25), the airflow is dynamically unstable and turbulent forces overpower stabilizing buoyant forces.

Richardson number and N^2 were computed by first interpolating input variables from both model data and observations at heights from 50 m AGL to 1500 m AGL at every 100 meters and then averaged over the reference depth to reduce noise.

Figure 4.12 shows a set of scatter plots of key variables from the observations and the model. There was no significant difference in the results from the three forecast blocks. The 700 hPa dew point temperature, water vapor mixing ratio (Qv), and precipitable water (PWAT) from the model and observations agree fairly well except for a few instances showing negative biases. In general, the model shows a slight cold bias, which is ~2 °C on

average for these 18 soundings. Whether this bias is systematic in the model or just representative of this sample of cases cannot be determined without having regularly scheduled sounding data in this region.

In terms of wind, the model tends to overestimate wind speed, especially for those precipitation events with relatively strong wind. Mean absolute bias was < 2 m s^{-1}, but the difference was as large as 10 m s^{-1} for the highest wind cases. The observations indicate that most of the 18 soundings measured wind directions between 220 and 290 degrees at 700 hPa. For those cases (with winds in the 220–290 degree range), the model predicted wind direction close to the observations. However, there is a slight bias of 18 degrees in these cases, indicating that the model winds tend to be rotated by this amount compared to the observations.

Wind speed and direction biases impact airflow interactions with local terrain and resulting orographic precipitation. A close look at wind speed and direction as well as precipitation on the days with sounding data revealed that the cases with the highest winds were the cases that the model predicted too much precipitation (see previous section). Similarly, when precipitation was too little in the model, wind speed was also less than the observations. No systematic pattern emerged from the wind direction difference and precipitation from this small sample of soundings.

In general, both the model and observations indicated Froude number of <1 (i.e. blocked flow) for these 18 sounding cases. This partly explains why the SNOTEL daily precipitation from sites on the western and eastern slopes of the Wind River Range was not well correlated. The scatter plot also shows that the model predicted higher Froude numbers than the observations, which is directly related to the high wind bias discussed above. The Froude number bias also gives possible evidence for the model-predicted precipitation being too aggressive. In particular, cases whose model-observation data points are notably away from the one-to-one line were also the storms with strong winds and the model indicated too much precipitation and larger wind speed. Another reason for the lack of the correlation of precipitation between western and eastern slopes is the fact that the Pinedale sounding data represents westerly storms that impact the western slopes more than the eastern slope (which receives precipitation from easterly events).

The square of the Brunt-Vaisala frequency (N^2) from the model and observations agree well. Richardson number from model and observations matched well for values < 1. However, the model predicted higher values for cases >1. Richardson number is sensitive to the discrepancy in wind gradient (in the vertical direction) and stability between the model and observations. Thus the bias is understandable given the differences we have seen in the wind speed and direction.

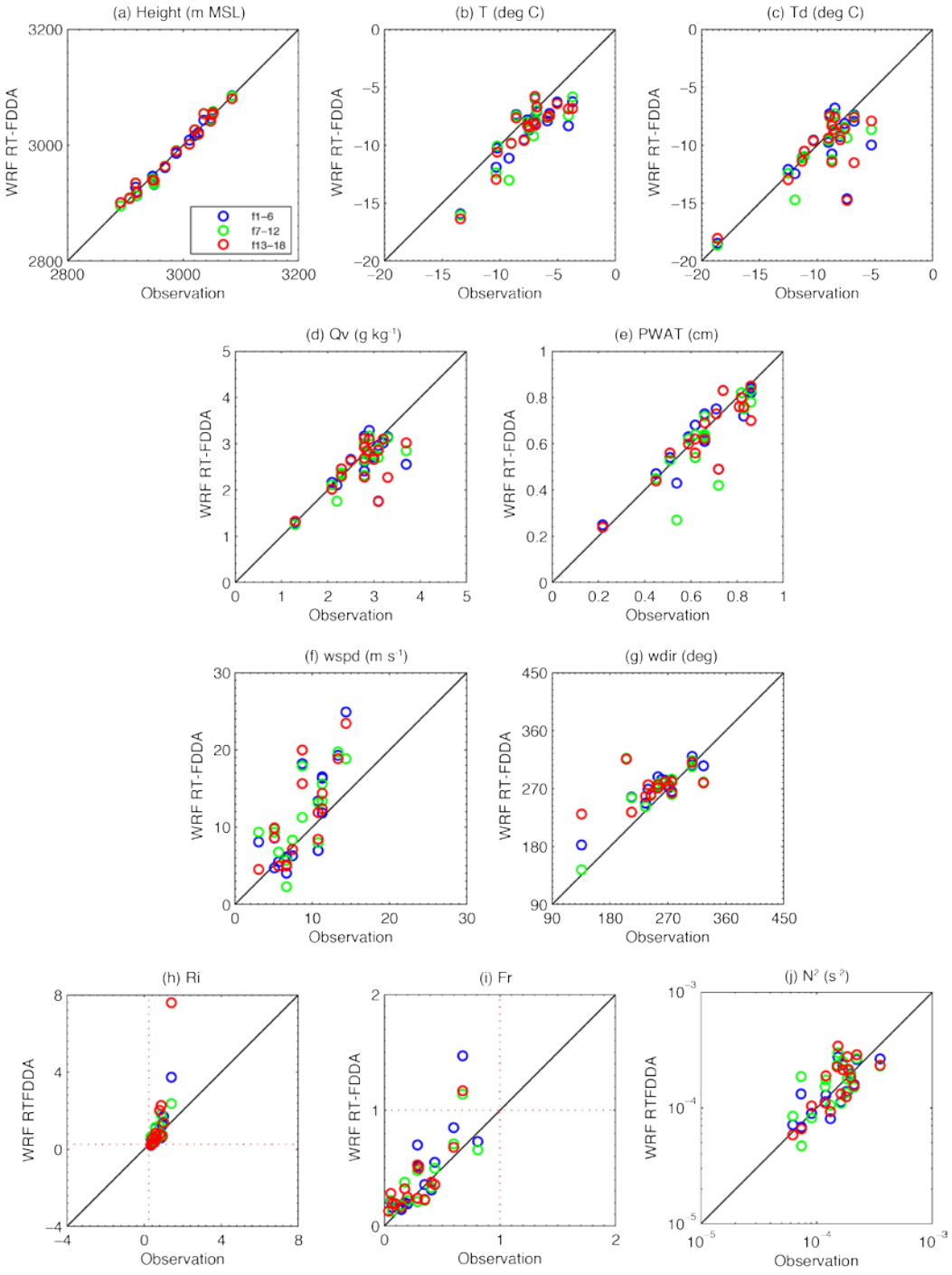

Figure 4.12. (a) Geopotential height, (b) dry-bulb temperature, (c) dew point temperature, (d) water vapor mixing ratio, (e) precipitable water, (f) wind speed, (g) wind direction at 700 hPa level from Saratoga sounding data and RT-FDDA. (h) Bulk Richardson number, (i) Froude number, and (j) squared of Brunt-Vaisala frequency. Red lines in (h) are a critical Richardson number of 0.25 (<0.25 indicates where flow is unstable/turbulent). Red lines in (i) are Froude number of 1 (Fr > 1 indicates flow that can go over the mountain barrier). Data points are color coded by forecast blocks; blue circles are for the first (F1–6), green for the second (F7–12), and red for the third forecast block (F13–18).

Radiometer data comparison

The radiometer located in Boulder, Wyoming was used by WMI forecasters to identify opportunities for cloud seeding, at least for the western slope of the Wind River Range. The radiometer measurements of LWP have been compared with LWP extracted from the RT-FDDA forecast model output along the same viewing angle paths. The measurements have been compared to the forecast model LWP using the F1-6 and F6-12 output for each of the western slope seeding cases called by WMI (hereafter, the operational cases). The modeled LWP at each forecast period was also been compared to the radiometer observations for each of the seeding forecast model algorithm cases called (hereafter, the model cases, described in Section 4.3.2).

Operational Cases

In the eleven west slope operational cases, the model generally under-predicted the LWP, regardless of the forecast hour period being compared (Figure 4.13-Figure 4.15). Both forecast period blocks appear to have similar representations of the LWP for the most operational cases. Both forecast blocks also seemed to get the general values of LWP for most of the operational cases, except the March 3 case at 0341 UTC, which the F1–6 model really under-forecast compared to the observations from the radiometer, but the F7–12 model did better at.

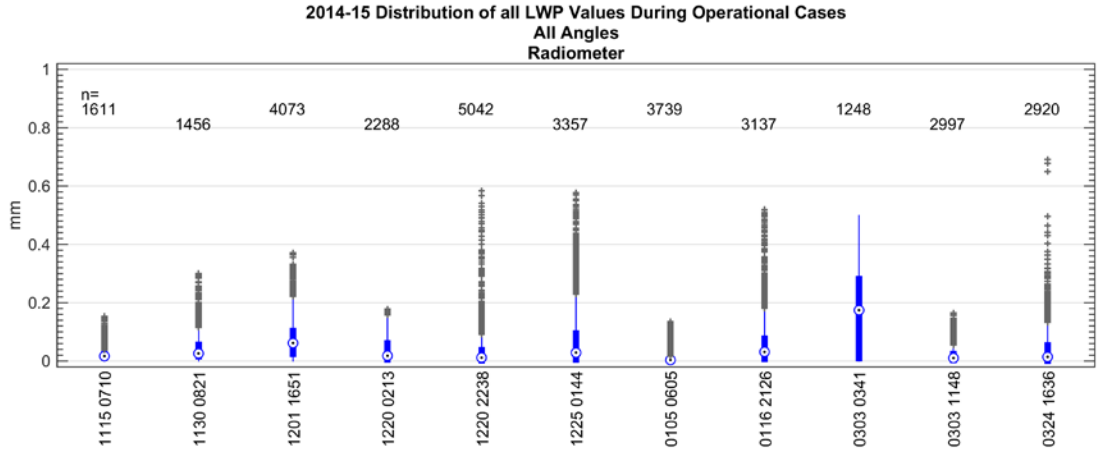

Figure 4.13. Box and whisker plots of radiometer-observed LWP values from the west slope operational cases. Measurements are roughly every minute, resulting in the large sample sizes and relatively high numbers of outlying points (denoted by the gray '+' symbols).

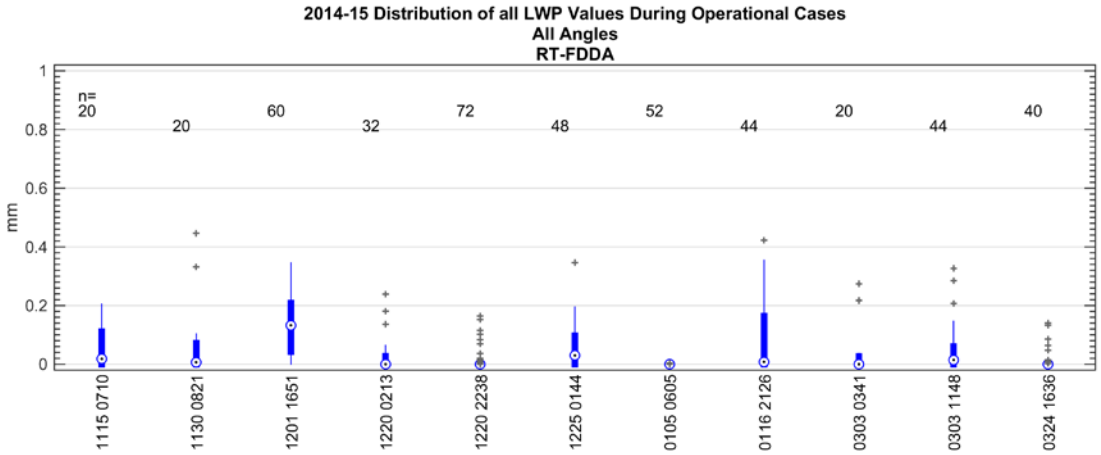

Figure 4.14. Box and whisker plots of model values of LWP from RT-FDDA forecast hours 1-6 concatenated together for the west slope operational cases. Model output is available every hour.

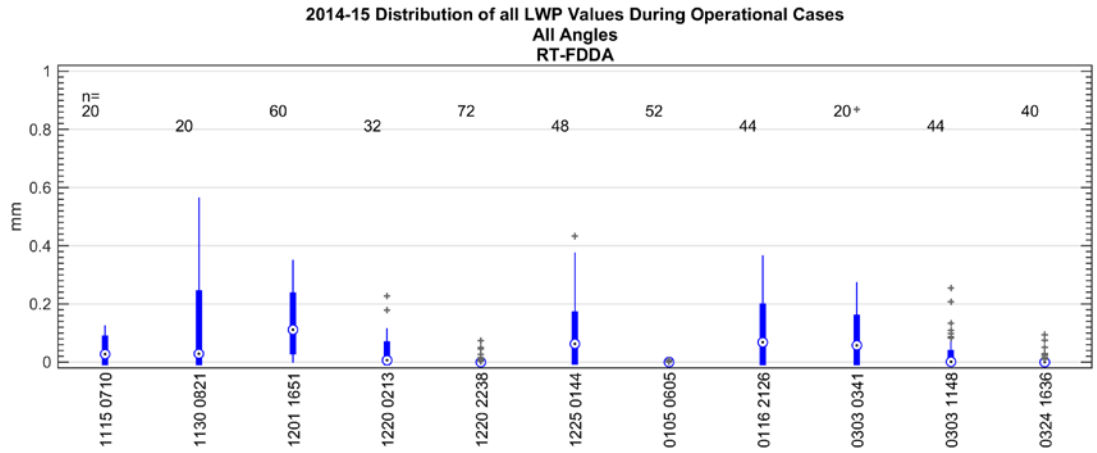

Figure 4.15. Box and whisker plots of model values of LWP from RT-FDDA forecast hours 7-12 concatenated together for the west slope operational cases. Model output is available every hour.

Histograms showing the modeled maximum and mean LWP during the west slope operational cases along the various viewing angles compared to those measured by the radiometer also reinforce the results of the boxplots above (shown in Figure 4.16–Figure 4.17 for the F7–12 forecast block only). The model typically underpredicts the maximum LWP compared to what was observed by the radiometer in the operational cases; however it does a better job representing the mean LWP in those cases (Figure 4.16–Figure 4.17).

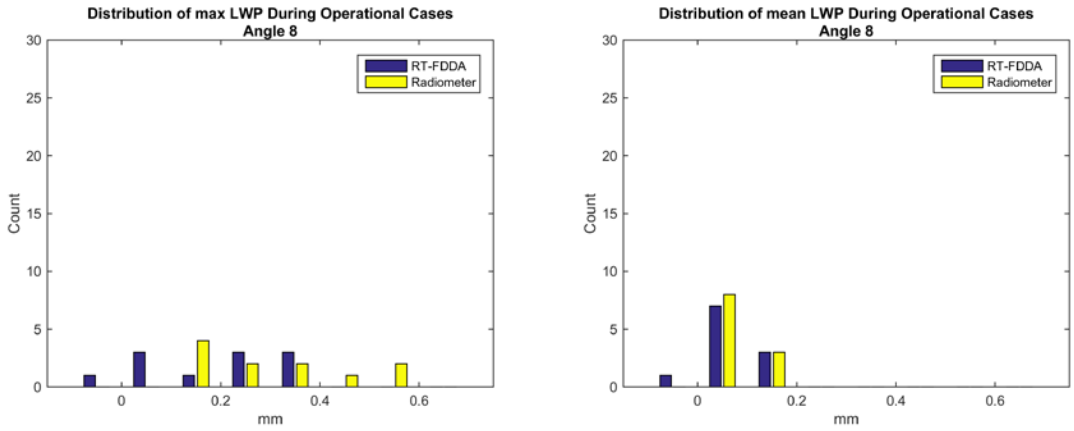

Figure 4.16. Histogram of modeled maximum LWP (left) and mean LWP (right) during the operational cases as simulated/measured along the angle 8 viewing path from the F7–12 model period (blue) compared to radiometer-observed values (yellow).

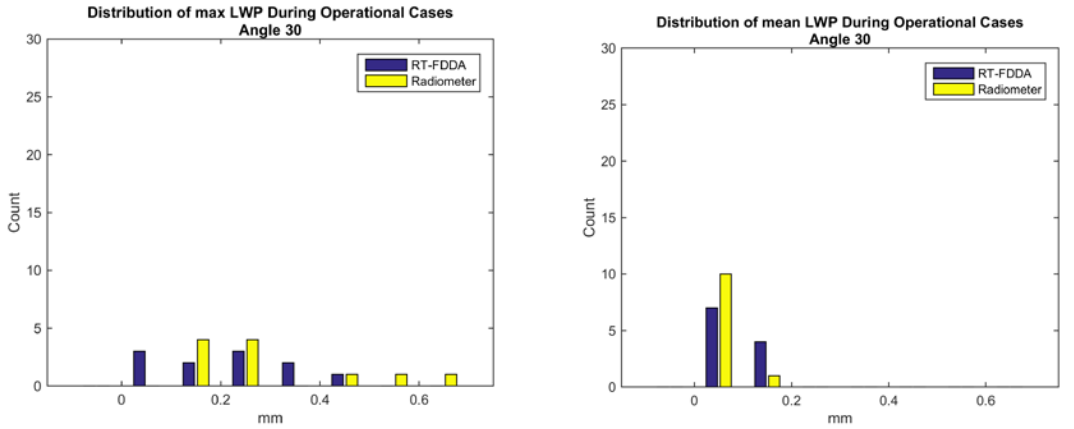

Figure 4.17. Histogram of modeled maximum LWP (left) and mean LWP (right) during the operational cases as simulated/measured along the angle 30 viewing path from the F7–12 model period (blue) compared to radiometer-observed values (yellow).

Model Cases

As described below (in Section 4.3.2), the case-calling algorithm defined several seeding cases. Histograms of the maximum and mean LWP during the model cases indicated generally good comparison of the model to the radiometer values of LWP, although the model tended to have more frequent instances of near zero LWP than observed by the radiometer (Figure 4.18–Figure 4.19).

These histograms indicate that the model cases have a higher frequency of having maximum LWP be zero (or very near zero) compared to the operational cases *along the viewing path of the radiometer*, based on both the modeled LWP and radiometer observations. This is likely because the model case-calling algorithm is assessing the presence of LWP over a broad area and not just along the single path where the radiometer is viewing, whereas the operational cases were being called based on when the radiometer observed non-zero LWP. Nonetheless, the comparison of the modeled LWP and

radiometer-observed LWP for these model cases is quite good, both in maximum and mean LWP during the model case seeding periods.

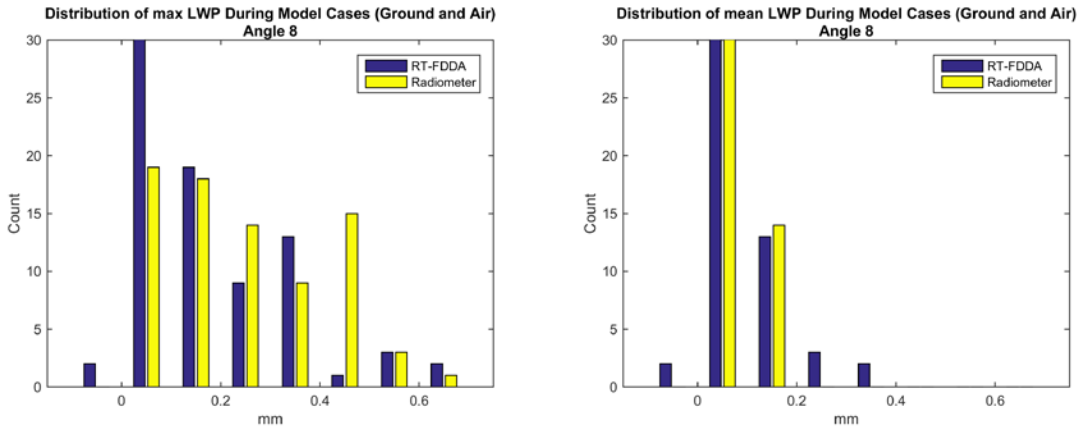

Figure 4.18. Histogram of modeled maximum LWP (left) and mean LWP (right) during the model cases as simulated/measured along the angle 8 viewing path from the F7–12 model period (blue) compared to for the radiometer-observed values (yellow).

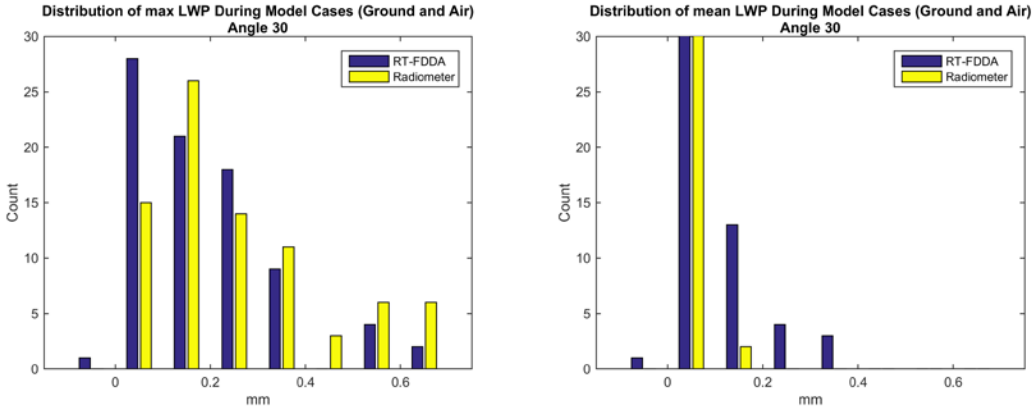

Figure 4.19. Histogram of modeled maximum LWP (left) and mean LWP (right) during the model cases as simulated/measured along the angle 30 viewing path from the F7–12 model period (blue) compared to for the radiometer-observed values (yellow).

4.3.2. Case-calling algorithm performance

The RT-FDDA cloud seeding forecast system simulated 609 forecasts (cycles) from 14 November 2014 1800 UTC to 15 April 2015 1800 UTC (some forecasts were incomplete having less than 24 hours of data). Among these 609 forecasts, 152 were identified by the case-calling algorithm to have suitable conditions for ground seeding in the WRR area, while only 36 forecasts were identified for WRR-E area. Very few 24-hour forecasts cycles were found to have more than one seeding case in the 24-hour forecast period for WRR. The average duration of these case-calling algorithm-identified ground-seeding cases are 9.3 and 7.5 hours for WRR and WRR-E respectively (Table 4.5). The case-calling algorithm

also identified 139 and 80 airborne seeding cases at regular (AS) and high altitudes (ASH) in WRR area (Table 4.5). Due to the prevailing westerly wind above the Wind River Range, very few airborne seeding cases were identified in WRR-E area. The average duration of the airborne seeding cases is similar to, but slightly shorter than, the ground-seeding cases.

Table 4.5. Results of the initial implementation of the case-calling algorithm from the 2014-2015 retrospective real-time test: number of forecasts with seeding cases called, numbers and average duration of seeding cases called by the forecast model for both the WRR and WRR-E regions and for ground (GS) and airborne seeding (AS, ASH). Note that due to forecast cycle overlap these metrics have some case duplication included. The numbers and average duration of *unique* seeding cases called by the forecast model, where cycle duplication has been removed, are shown as well as the numbers and average duration of operational cases. The number of cases in common between the unique-called model cases and operational cases is listed in the bottom row. Table entries that are not applicable are marked as '--'.

	WRR			WRR-E		
	GS	**AS**	**ASH**	**GS**	**AS**	**ASH**
# Forecast cycles	152	114	65	36	2	0
# Cases	157	139	80	36	2	0
Avg time/case (h)	9.3	8.6	7.3	7.5	5	--
# Unique cases	40	31	16	15	1	0
# Avg unique time (h)	13.4	13.2	13.1	8.2	6	--
# Operational cases	11	--	--	9	--	--
Avg Ops case time (h)	10.1	--	--	8.9	--	--
# Common cases	10	--	--	5	--	--

Since the RT-FDDA forecast was cycled every 6 hours, the 24-hour forecast periods overlap. Therefore, a seeding period (> 6 hours) that is consistently forecast from one cycle to the next will be identified by more than one forecast cycle. This results in a duplication of seeding cases when considering metrics based on all cycles separately. In order to remove this duplication, we use an objective algorithm that combines cases that had common "absolute" times (in UTC) into one single case based on if there is any overlap (including as little as common end and/or start times; see Figure 4.20). After such duplication is removed, the number of unique ground seeding cases (or periods) dropped to 40 for WRR, and 15 for WRR-E (Table 4.5). The number of unique airborne cases for WRR also reduced to 31 and 16 in regular (AS) and high altitudes (ASH) respectively. The average ground seeding period increased to 13 hours for WRR and 8 hours for WRR-E.

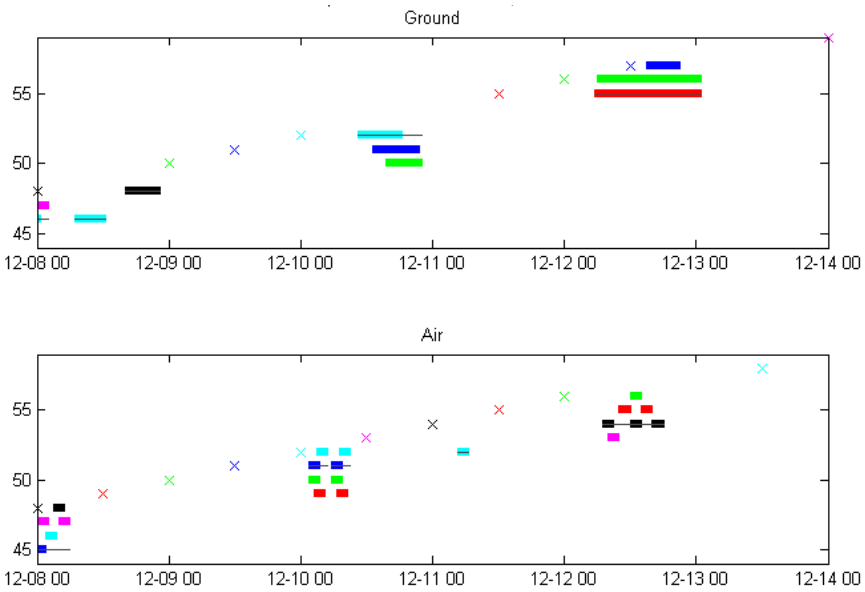

Figure 4.20. Visual depiction of cases called from various forecast initializations in UTC time. Each row is represented by its own color and represents a different forecast initialization (i.e. the vertical axis represents the forecast period "number" sequentially in time) with an 'x' of the same color denoting the forecast initialization time. The absolute time (in UTC) is shown on the horizontal axis. The length of the colored bar represents the length of the seeding case for the given forecast cycle, and a thin black line is overlaid to highlight the combined case times (one per group of overlapping cases). Ground cases are in the top panel and airborne cases in the bottom panel.

During the 2014–2015 winter season, 11 and 9 ground seeding cases were called and operated by WMI in the WRR and WRR-E areas respectively. The average operational periods were 10 hours for WRR and 9 hours for WRR-E cases. Among all 11 WRR operational seeding cases, only one case (on 5 January 2015) was not identified by the case-calling algorithm. In the WRR-E region, 5 out of the 9 cases were identified by the case-calling algorithm. Overall, the case-calling algorithm performed reasonably well compared to the model-identified cases, although it identified more seeding opportunities than the WMI forecasters, likely due to the fact that this initial implementation did not include dispersion criteria. The results of the algorithm once dispersion criteria were implemented are presented below in Section 4.4 (see Table 4.10).

4.4. Analysis of Simulated Seeding Effects from the Season

As discussed in the previous section, the same absolute seeding cases may be simulated in multiple retrospective seeding forecast cycles (previously referred to as case duplication). To gain a representative seasonal simulated seeding effect, accumulations of 6-hour precipitation were concatenated to form a continuous and non-overlapping time series since the RT-FDDA has a 6-hour cycle, as described in Section 4.3.1. The F0–6, F6–12, F12–18 and F18–24 6-hourly accumulation time series were extracted from both the control and seeding forecasts. The summation of each series gives the total forecast precipitation over the entire season. The seasonal simulated seeding effect was then calculated by

subtracting the total precipitation of control forecasts from that of seeding forecast. Figure 4.21 shows the seasonal simulated seeding effect on precipitation (in mm) for the four 6-hourly forecast blocks. These results do vary slightly based upon which forecast block is utilized, but show that over the entire season the simulated seeding enhancements on precipitation fall over the Wind River Range, the primary target area.

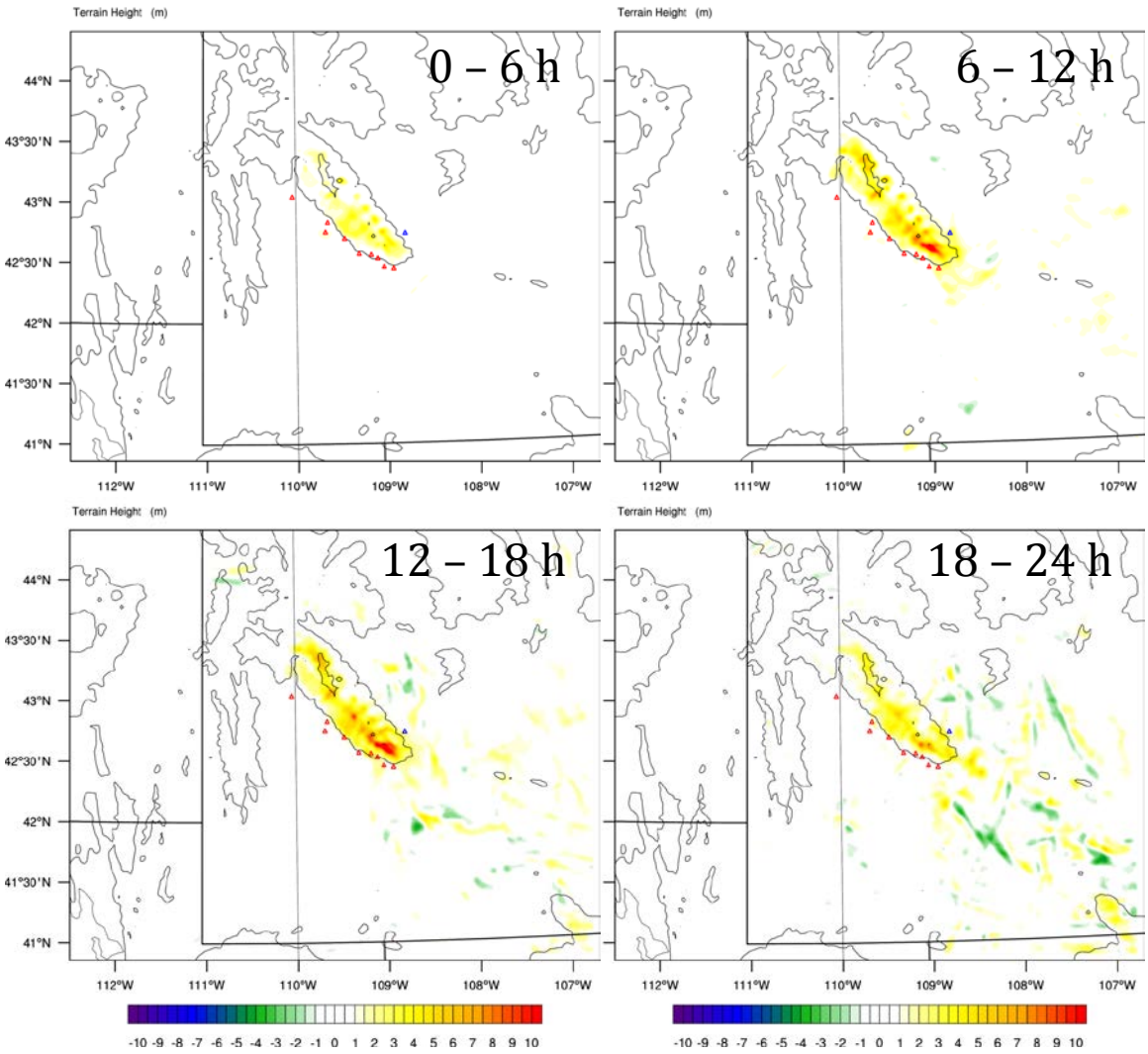

Figure 4.21. Seasonal simulated seeding effect (change in precipitation) in mm based on total precipitation calculated by the four 6-hourly forecast blocks.

The qualitative results of the simulated seeding effects are listed in Table 4.6–Table 4.9 for the four forecast blocks. The total control precipitation forecast over the season, the absolute simulated seeding effect, and the relative simulated seeding effect (relative to the total seasonal forecast precipitation) were calculated over the entire domain, the Big Horn basin, the North Platte basin, and the Green River basin (as shown in Figure 4.22). Furthermore, the simulated seeding effects above 8000 feet in these watersheds that

intersect the Wind River Range (as shown in Figure 4.23) are calculated as well. The latter values are considered the simulated snowpack enhancement that can survive the entire winter. The results indicate that the ground-based seeding simulated in the model over the entire season had a very small effect (<1% relative to the total seasonal precipitation, in most cases). In an absolute sense, the Green River and Bighorn River basins receive the most additional precipitation, split nearly equally in most forecast blocks.

Table 4.6. The control precipitation (acre feet), the absolute simulated seeding effect (acre feet), and the relative simulated seeding effect (%) relative to the total seasonal control forecast precipitation based on the F0-6 forecast block.

F0–-6	Domain	Big Horn	Green	N. Platte	WRR Big Horn	WRR Green	WRR N. Platte
Total Seasonal Precip (AF)	26587998	2988610	4939486	873482	1328477	1660017	131258
Simulated Seed Effect (AF)	9044	3724	3541	1022	2995	2791	406
% SE	0.03	0.12	0.07	0.12	0.23	0.17	0.31

Table 4.7. Same as Table 4.6 but for the F6–12 forecast block.

F6–-12	Domain	Big Horn	Green	N. Platte	WRR Big Horn	WRR Green	WRR N. Platte
Total Seasonal Precip (AF)	26530914	3068335	4826546	865369	1341729	1619256	135896
Simulated Seed Effect (AF)	28903	10401	8065	4630	6361	5289	1310
% SE	0.11	0.34	0.17	0.54	0.47	0.33	0.96

Table 4.8. Same as Table 4.6 but for the F12–18 forecast block.

F12–-18	Domain	Big Horn	Green	N. Platte	WRR Big Horn	WRR Green	WRR N. Platte
Total Seasonal Precip (AF)	27120096	3178884	4835856	938944	1361536	1584449	137313
Simulated Seed Effect (AF)	32940	10140	10435	5785	6600	6200	1525
% SE	0.12	0.32	0.22	0.62	0.48	0.39	1.11

Table 4.9. Same as Table 4.6 but for the F18–24 forecast block.

F18-–24	Domain	Big Horn	Green	N. Platte	WRR Big Horn	WRR Green	WRR N. Platte
Total Seasonal Precip (AF)	27517652	3320714	4869534	1001317	1358837	1589070	139543
Simulated Seed Effect (AF)	25520	5735	8386	3887	4434	4358	1221
% SE	0.09	0.17	0.17	0.39	0.33	0.27	0.88

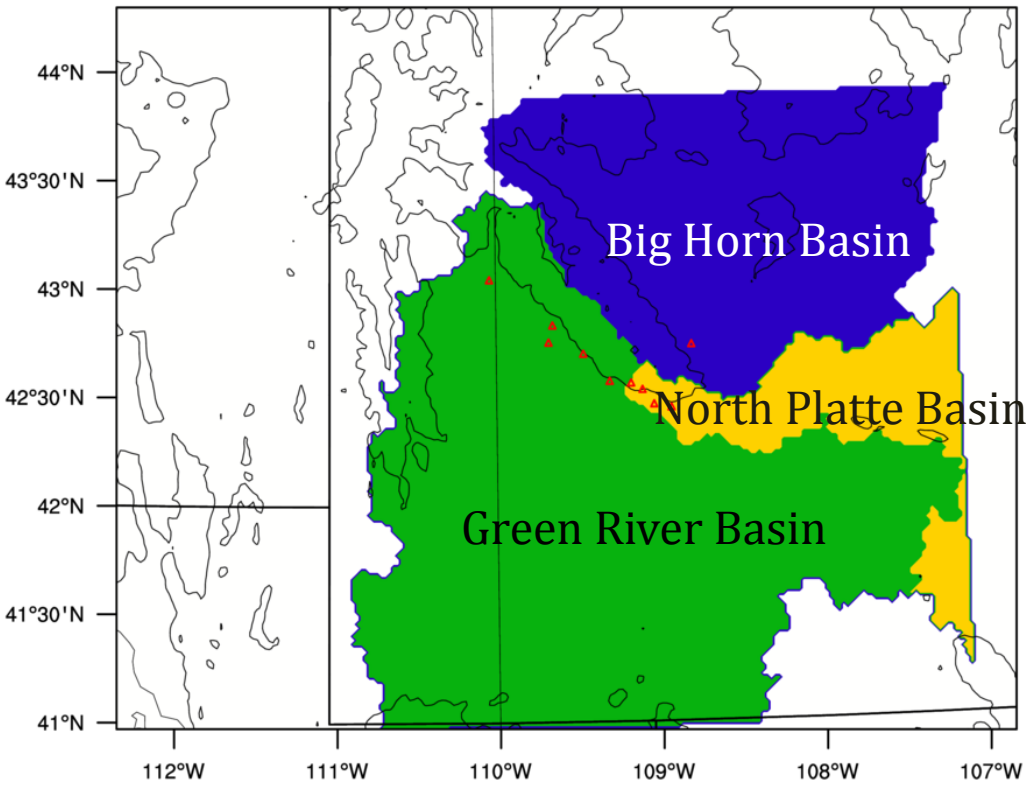

Figure 4.22. Map of watersheds over which the simulated seeding effects are calculated.

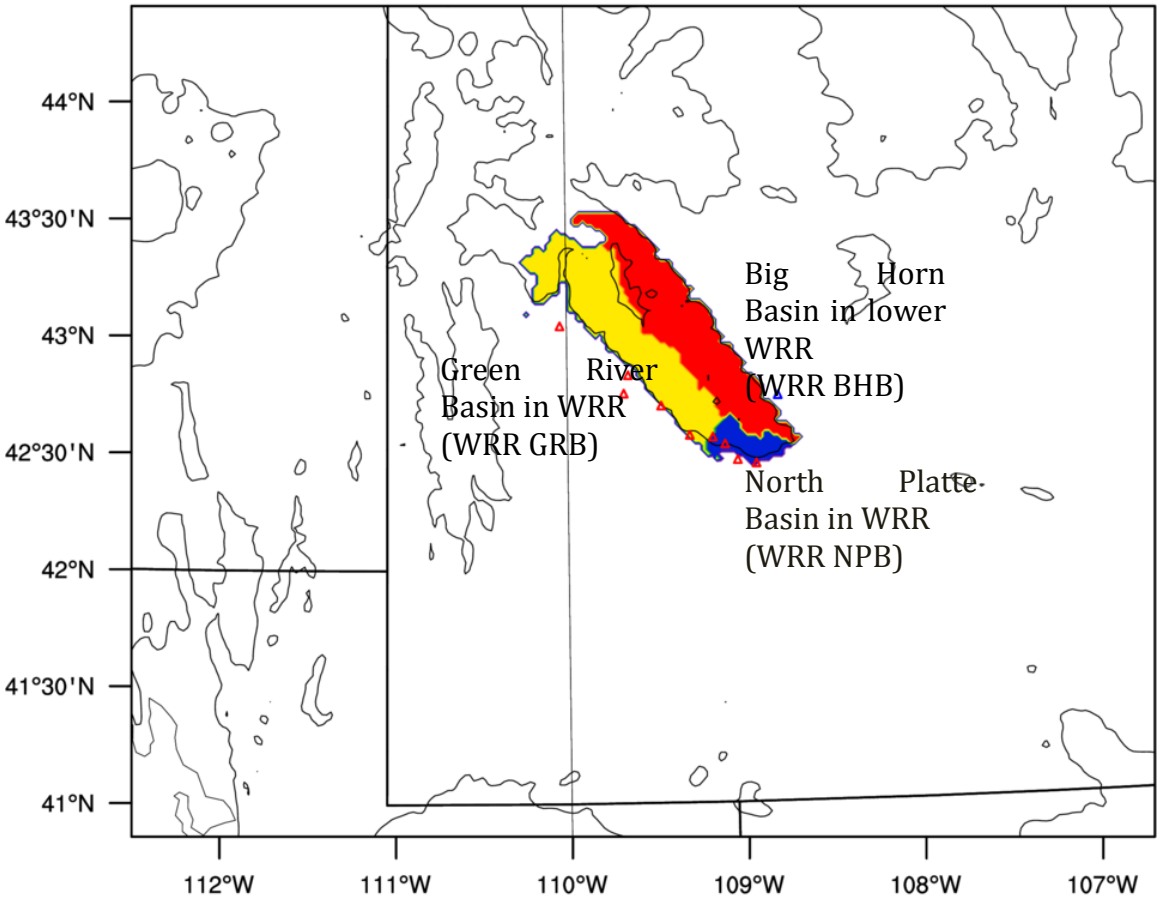

Figure 4.23. The map of watersheds intersecting the Wind River Range above 8000 feet over which the simulated seeding effects are calculated.

Given that the seasonal simulated seeding effect is rather small in the Wind River Range, the following presents analysis to reveal why this is the case.

The Green River Basin is a plateau in between two high mountain ranges (Wyoming Range and Wind River Range). The geographic layout leads to very stable air within the basin. Figure 4.24 shows the Probability Density Function (PDF) of the stability index (square of the Brunt Vaisala frequency; BN2) and the Froude number (Fr) below 1 km for all the seeding forecasts (forecasts with seeding cases called based on microphysical criteria). Obviously, the atmosphere in the lower levels is relatively stable (BN2> 1e−4) most of the forecast time (~90% of the time) over WRR and WRR-E areas. As a result, the Fr is less than unity (indicating potential blocking of the flow) 70% of the time. This indicates that the AgI plumes released from the generators at the foothills of the Wind River Range are blocked or have difficulty getting over the mountain. Therefore, the impacts of AgI released from ground-based generators on cloud and precipitation may be very limited.

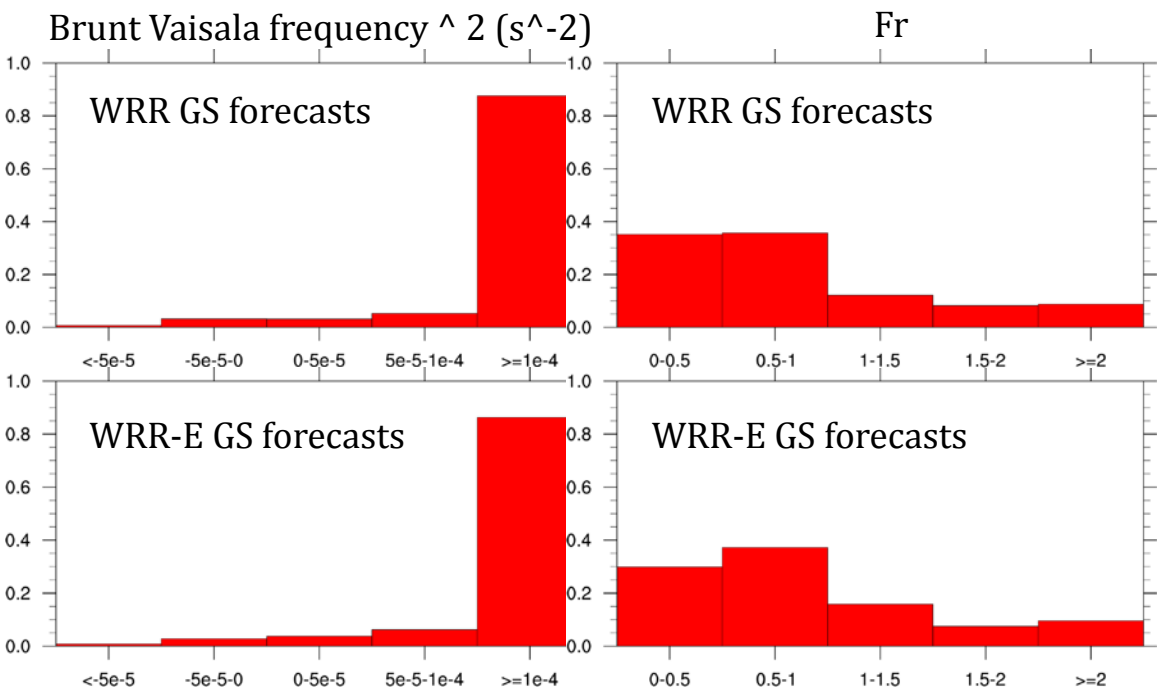

Figure 4.24. PDF of BN2 and Fr of forecast having WRR and WRR-E ground seeding cases determined by the case-calling algorithm.

When the dispersion criteria—BN2, Fr, Ri (bulk Richardson number)—are considered in the case-calling algorithm for ground-based seeding, the numbers of seeding forecasts and seeding cases were reduced in both WRR and WRR-E areas (see Table 4.10 for details). Overall, the total numbers of unique cases called by the case-calling algorithm were similar to the total cases identified by WMI forecasters, however there were fewer cases in common. Some reasons for the discrepancy in identified cases could be due to the fact that the WMI forecasters utilized the real-time model forecasts run with an older version of WRF that included some different physics options (i.e. v3.1 versus v3.5.1 and YSU versus MYJ PBL scheme) than what was used for the retrospective simulations on which the case-calling algorithm was run. Therefore, these two forecast realizations may vary.

Table 4.10. Case-calling algorithm case statistics for ground-based seeding when dispersion criteria are considered.

With dispersion criteria	WRR GS	WRR-E GS
# Forecasts	51	4
# Cases	54	4
Avg time/case (h)	6.5	5.5
# Unique cases	17	3
Avg Unique time (h)	9.1	6.0
# Common cases (with ops)	5	2

The seasonal simulated seeding effects for the storms called by the case-calling algorithm using dispersion criteria (recall Table 4.10) and simulated by the seeding forecast model are shown in Table 4.11-Table 4.14. Similar to that shown above, the results indicate that the ground-based seeding simulated in the model had a very small effect (<1%) relative to the total *seedable* precipitation over the season. In an absolute sense, the Green River and Bighorn River basins still received the most additional precipitation, split nearly equally in most forecast blocks.

Table 4.11. The control precipitation during seeded periods (acre feet), the absolute simulated seeding effect (acre feet), and the relative simulated seeding effect (%) relative to the total seasonal control forecast precipitation during seeded periods based on the F0-6 forecast block.

F0-6	Domain	Big Horn	Green	N. Platte	WRR Big Horn	WRR Green	WRR N. Platte
Total Seasonal Precip during seeding (AF)	6065724	626901	1172211	176777	322881	443821	31147
Simulated Seed Effect (AF)	3596	1335	1277	625	798	1035	130
% SE relative to seeded periods	0.06	0.21	0.11	0.35	0.25	0.23	0.42

Table 4.12. Same as Table 4.11, but for the F6-12 forecast block.

F6-12	Domain	Big Horn	Green	N. Platte	WRR Big Horn	WRR Green	WRR N. Platte
Total Seasonal Precip during seeding (AF)	5588288	580371	937112	152419	321646	386484	31732
Simulated Seed Effect (AF)	17727	5758	4264	3382	2581	2894	735
% SE relative to seeded periods	0.32	0.99	0.46	2.22	0.8	0.75	2.32

Table 4.13. Same as Table 4.11, but for the F12-18 forecast block.

F12-18	Domain	Big Horn	Green	N. Platte	WRR Big Horn	WRR Green	WRR N. Platte
Total Seasonal Precip during seeding (AF)	5598022	596159	986512	137853	339077	406646	28863
Simulated Seed Effect (AF)	17536	4902	5515	3589	2510	3213	891
% SE relative to seeded periods	0.31	0.82	0.56	2.6	0.74	0.79	3.09

Table 4.14. Same as Table 4.11, but for the F18-24 forecast block.

F18-24	Domain	Big Horn	Green	N. Platte	WRR Big Horn	WRR Green	WRR N. Platte
Total Seasonal Precip during seeding (AF)	5421200	783095	973463	199087	315953	360976	30883
Simulated Seed Effect (AF)	10558	1856	3638	2143	2083	1734	655
% SE relative to seeded periods	0.19	0.24	0.37	1.08	0.66	0.48	2.12

Individual Forecast Simulations

The stability analysis demonstrates that the impact on precipitation due to ground seeding can be limited when a stable atmosphere prevails in the Wind River Range. Both climatology and case-calling algorithm results showed that there is good potential for airborne seeding in the Wind River Range. Six forecasts were chosen to show the comparisons between ground seeding and airborne seeding. Within the 6 cases, two have good simulated ground seeding effects (20 December 2014 and 16 January 2015), two have null or very weak simulated ground seeding effects (20 November 2014 and 29 November 2014), and two are operational cases also with very weak simulated ground seeding effects (30 November 2014 and 24 March 2015). The flight track is assumed to be parallel to the Wind River Range and at 4000 m MSL height (Figure 4.25). The ground and airborne seeding cases called by the case-calling algorithm are listed in Table 4.15 for these 6 forecasts. For the 20 December and 16 January forecasts, two 2-hour airborne seeding cases were simulated while one airborne seeding case was simulated for each of the rest of the cases. The seeding rate for airborne case is set to 2 kg h^{-1} (based on Idaho Power airborne seeding operational data).

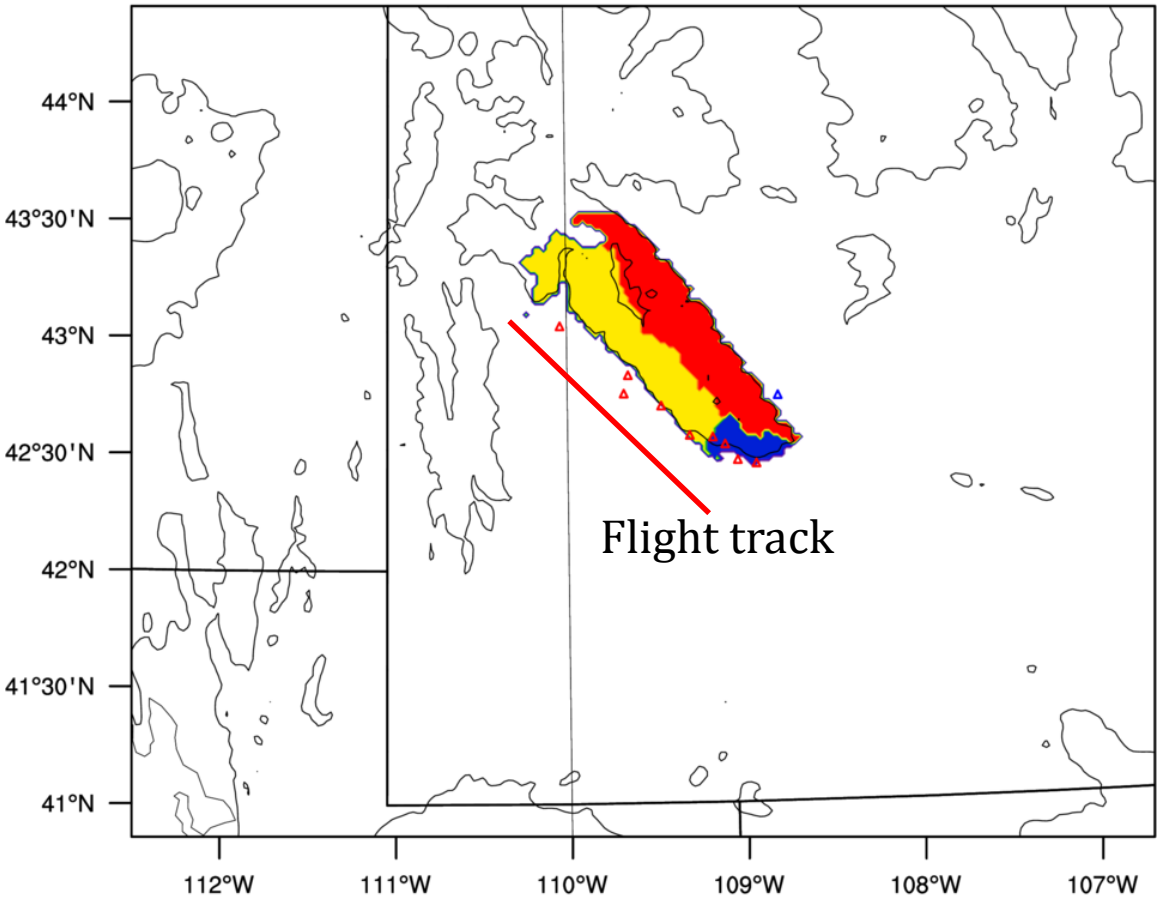

Figure 4.25. Map showing the simulated flight track (red line).

Table 4.15. Ground and airborne seeding cases called by the case-calling algorithm for the six selected forecasts (MMDDHH in UTC).

	WRR GS	WRR AS
20 Dec 2014	122000 to 122100	122007 to 122009 and 122020 to 122022
16 Jan 2015	011616 to 011710	011619 to 011621 and 011701 to 011703
20 Nov 2014	112023 to 112106	112100 to 112102
29 Nov 2014	112907 to 113000	112914 to 112916
30 Nov 2014	113000 to 113006	113000 to 113002
24 Mar 2015	032420 to 032503	032422 to 032500

The simulated seeding effects from the ground and airborne seeding cases for these 6 forecasts are listed in Table 4.16-Table 4.21. The average LWP during the forecast time is plotted for each forecast in Figure 4.26. Note that all cases except one had notable liquid water over the majority of the Range.

Figure 4.27-Figure 4.28 show the AgI concentrations during the seeding period at low and high levels (below 1 km AGL and from 3.5 to 4.5 km MSL) for ground seeding cases. The corresponding plots for airborne cases are shown in Figure 4.30-Figure 4.31. The simulated seeding effects of the ground seeding and airborne seeding are plotted in Figure 4.29 and Figure 4.32.

These results indicated that the AgI plumes from the ground generators had a tendency to be blocked and as a result go around the Wind River Range due to the low Fr in three of the six forecasts (20 December, 16 January, and 20 November). Even when the AgI plumes got over the Range in the other three forecasts, the concentrations of AgI below 1 km AGL from these ground-seeding cases were similar to those from the airborne seeding cases (Figure 4.27, Figure 4.30), indicating the airborne seeding effectively seeded the ground-seeding (surface) layer. However, the airborne seeding generated a much a higher concentration of AgI between 3.5 and 4.5 km compared to the ground-seeding cases. The larger coverage (both horizontally and vertically) and higher concentrations of the AgI plumes from the airborne seeding depleted more liquid water and generated more precipitation on the ground than the ground seeding cases in all of these simulations except for the 20 December forecast (Table 4.16–Table 4.21 and Figure 4.29 and Figure 4.32). For this specific case, the ground and airborne seeding simulations impacted different areas of the Range, such that simulated ground-based seeding produced a positive seeding effect in the northern portion of the Range where there was notable LWP, while simulated airborne seeding did not impact this area given that the AgI plume dispersed more over the southern portion of the Range (Figure 4.26–Figure 4.32). The two methods combined, in this case in particular, would have possibly produced a much broader, and therefore larger, simulated seeding impact in the region.

The limited vertical dispersion of AgI from the ground generators could be in part due to the relatively coarse resolution of the model (2 km), which does not fully resolve terrain-induced eddies that enhance vertical dispersion. Future studies should evaluate this possibility using Large Eddy Simulations.

Table 4.16. Simulated seeding effects of 20 December 2014 forecast. Total forecast control precipitation (acre feet), ground seeding (GS) and airborne seeding (AS) simulated seeding effect (SE) in acre feet (AF) and relative (%) to control precipitation for the given storm.

	Domain	Big Horn	Green	N. Platte	WRR Big Horn	WRR Green	WRR N. Platte
Control	429496	6026	23679	1643	5620	11322	424
GS SE (af)	1945	573	1175	47	578	1139	33
GS SE (%)	0.45	9.5	4.96	2.86	10.28	10.06	7.72
AS SE (af)	1436	312	945	190	315	819	112
AS SE (%)	0.33	5.18	3.99	11.58	5.6	7.24	26.51

Table 4.17. Same as Table 4.16, but for 16 January 2015 forecast.

	Domain	Big Horn	Green	N. Platte	WRR Big Horn	WRR Green	WRR N. Platte
Control	298679	17164	34658	4262	16047	20170	878
GS SE (af)	1290	406	836	63	411	726	49
GS SE (%)	0.43	2.37	2.41	1.48	2.56	3.6	5.62
AS SE (af)	3748	1321	1835	809	1317	1690	492
AS SE (%)	1.25	7.7	5.29	18.98	8.21	8.38	56.06

Table 4.18. Same as Table 4.16, but for 20 November 2014 forecast.

	Domain	Big Horn	Green	N. Platte	WRR Big Horn	WRR Green	WRR N. Platte
Control	47474	614	9105	179	607	2515	34
GS SE (af)	-2	-2	6	0	-2	3	0
GS SE (%)	0	-0.26	0.07	0.27	-0.34	0.12	0.3
AS SE (af)	423	21	407	6	21	239	6
AS SE (%)	0.89	3.35	4.47	3.23	3.4	9.48	16.56

Table 4.19. Same as Table 4.16, but for 29 November 2014 forecast.

	Domain	Big Horn	Green	N. Platte	WRR Big Horn	WRR Green	WRR N. Platte
Control	1447012	163410	225276	14604	102581	121370	3818
GS SE (af)	368	200	86	5	200	80	5
GS SE (%)	0.03	0.12	0.04	0.03	0.19	0.07	0.14
AS SE (af)	4855	4510	87	342	3690	115	1
AS SE (%)	0.34	2.76	0.04	2.34	3.6	0.09	0.04

Table 4.20. Same as Table 4.16, but for 30 November 2014 forecast.

	Domain	Big Horn	Green	N. Platte	WRR Big Horn	WRR Green	WRR N. Platte
Control	1911246	239292	348216	22260	154808	185067	5822
GS SE (af)	2082	306	33	445	18	11	9
GS SE (%)	0.11	0.13	0.01	2	0.01	0.01	0.15
AS SE (af)	2581	2142	1	68	1559	-17	0
AS SE (%)	0.14	0.9	0	0.3	1.01	-0.01	-0.01

Table 4.21. Same as Table 4.16, but for 24 March 2015 forecast.

	Domain	Big Horn	Green	N. Platte	WRR Big Horn	WRR Green	WRR N. Platte
Control	1180990	119524	224155	35385	71416	95061	6791
GS SE (af)	94	42	42	26	39	62	3
GS SE (%)	0.01	0.04	0.02	0.07	0.05	0.07	0.04
AS SE (af)	1375	823	393	226	873	484	133
AS SE (%)	0.12	0.69	0.18	0.64	1.22	0.51	1.96

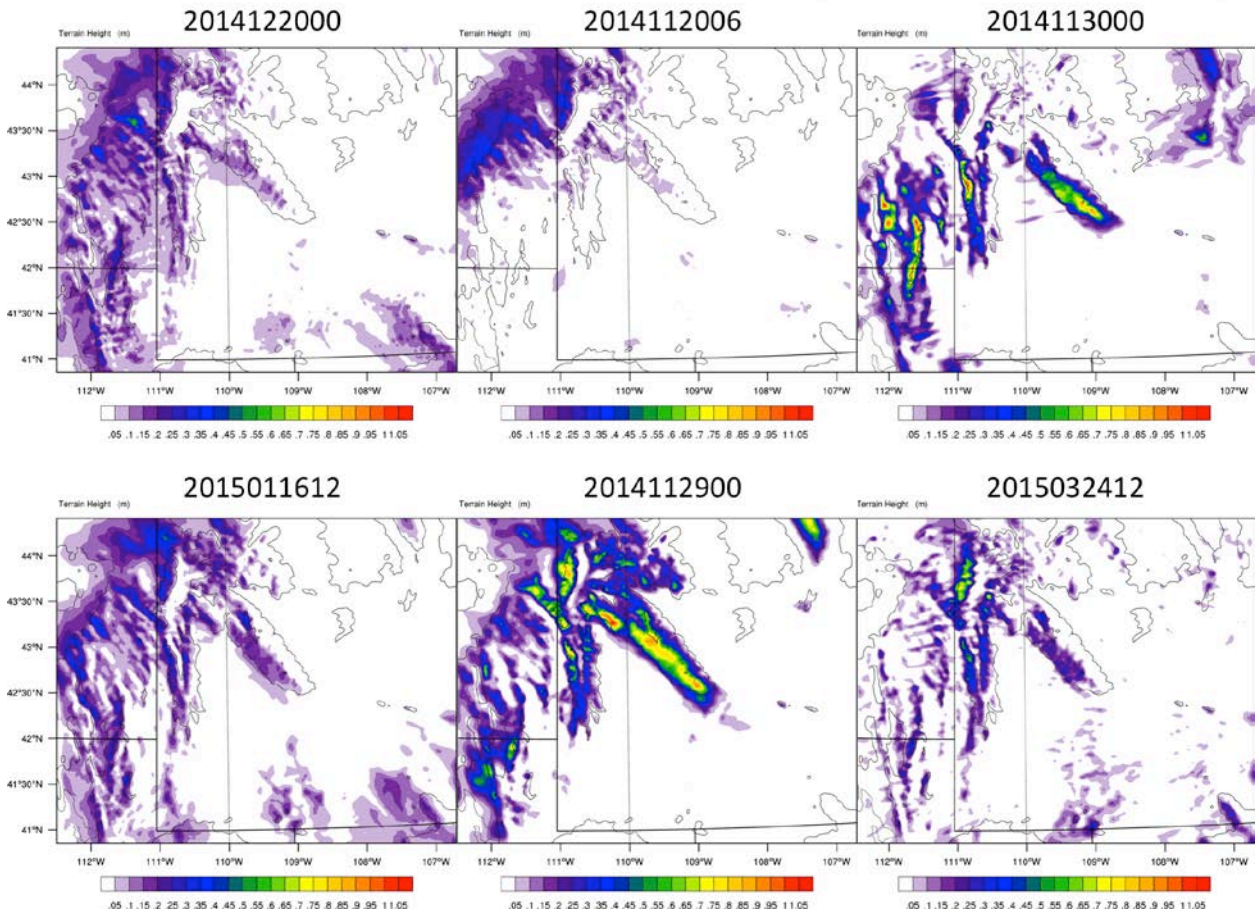

Figure 4.26. Averaged LWP in mm for each forecast (YYYYMMDDHH).

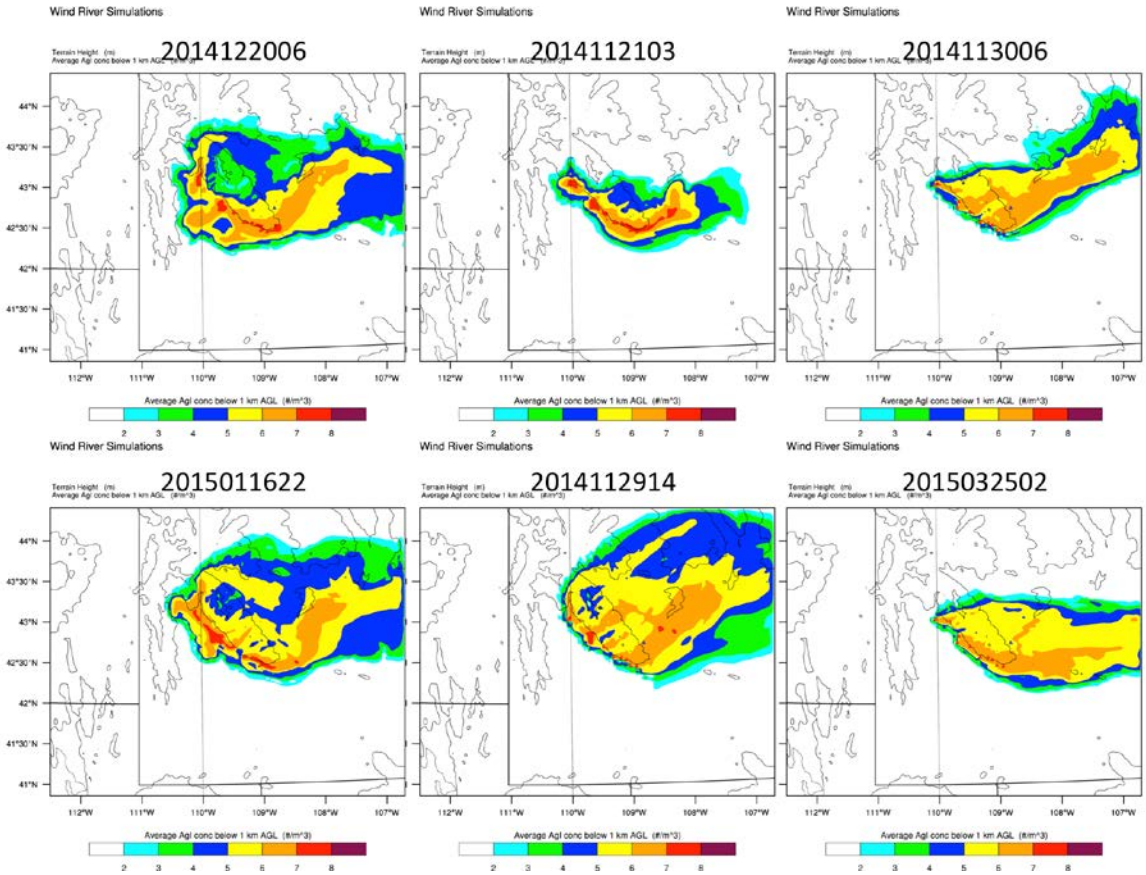

Figure 4.27. Averaged AgI concentration in Log10(#/m^-3) below 1 km AGL at hour 6 of the seeding time for the ground seeding cases.

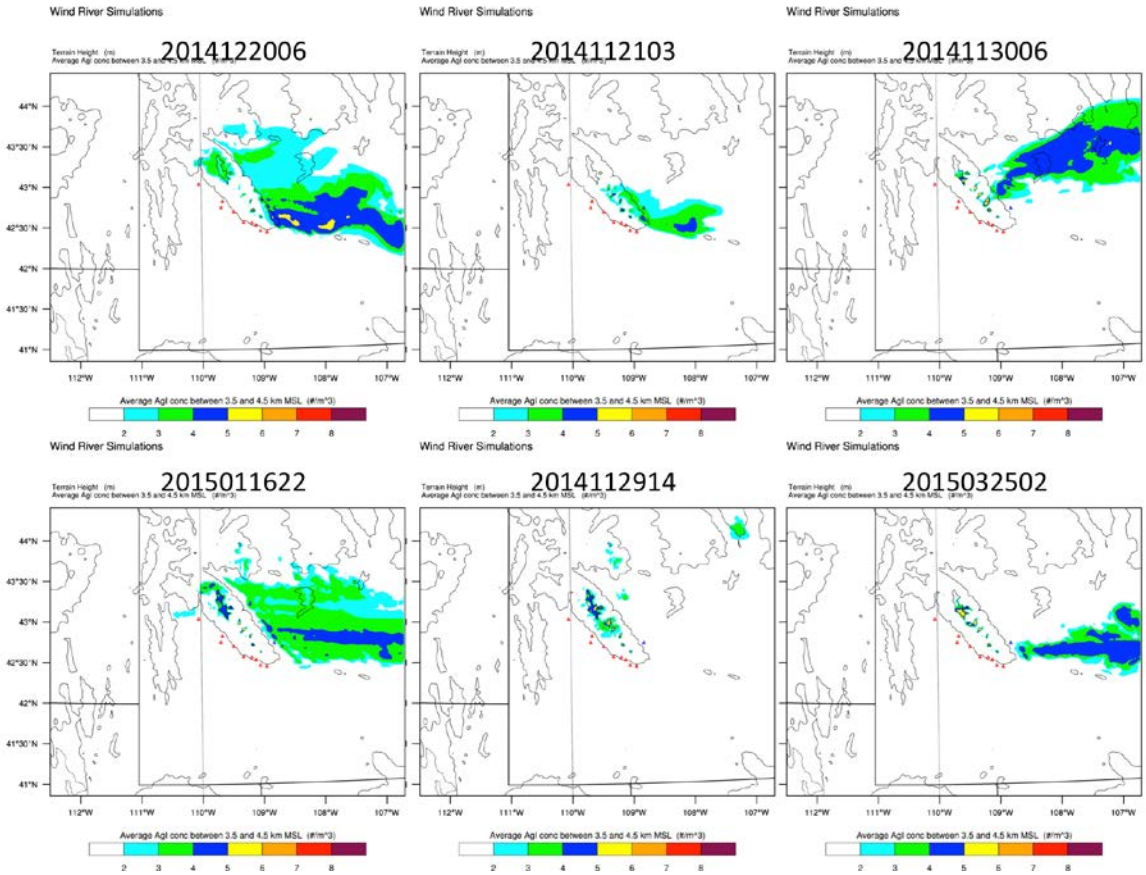

Figure 4.28. Averaged AgI concentration in Log10(#/m^-3) between 3.5 and 4.5 km MSL at hour 6 of the seeding time for the ground seeding cases.

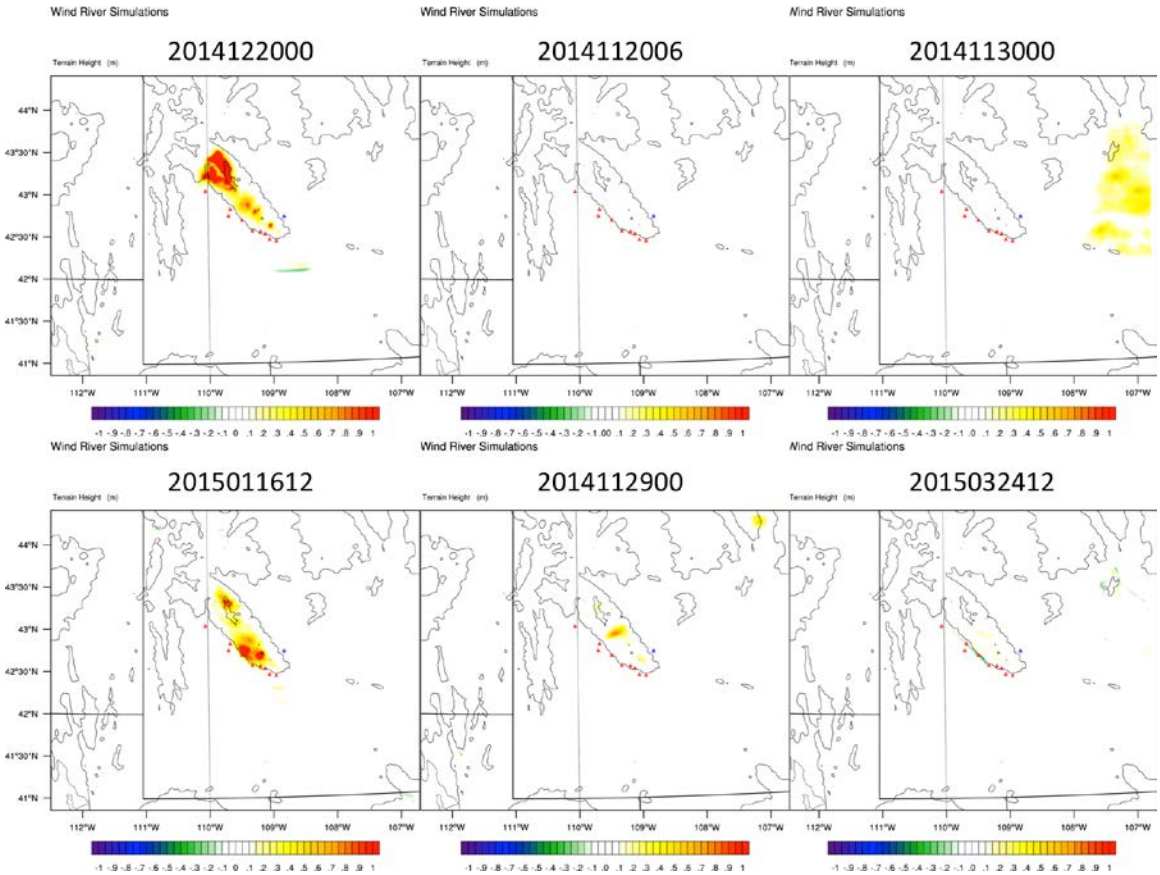

Figure 4.29. Maps of the simulated seeding effect (mm) at the end of the forecast for ground seeding cases.

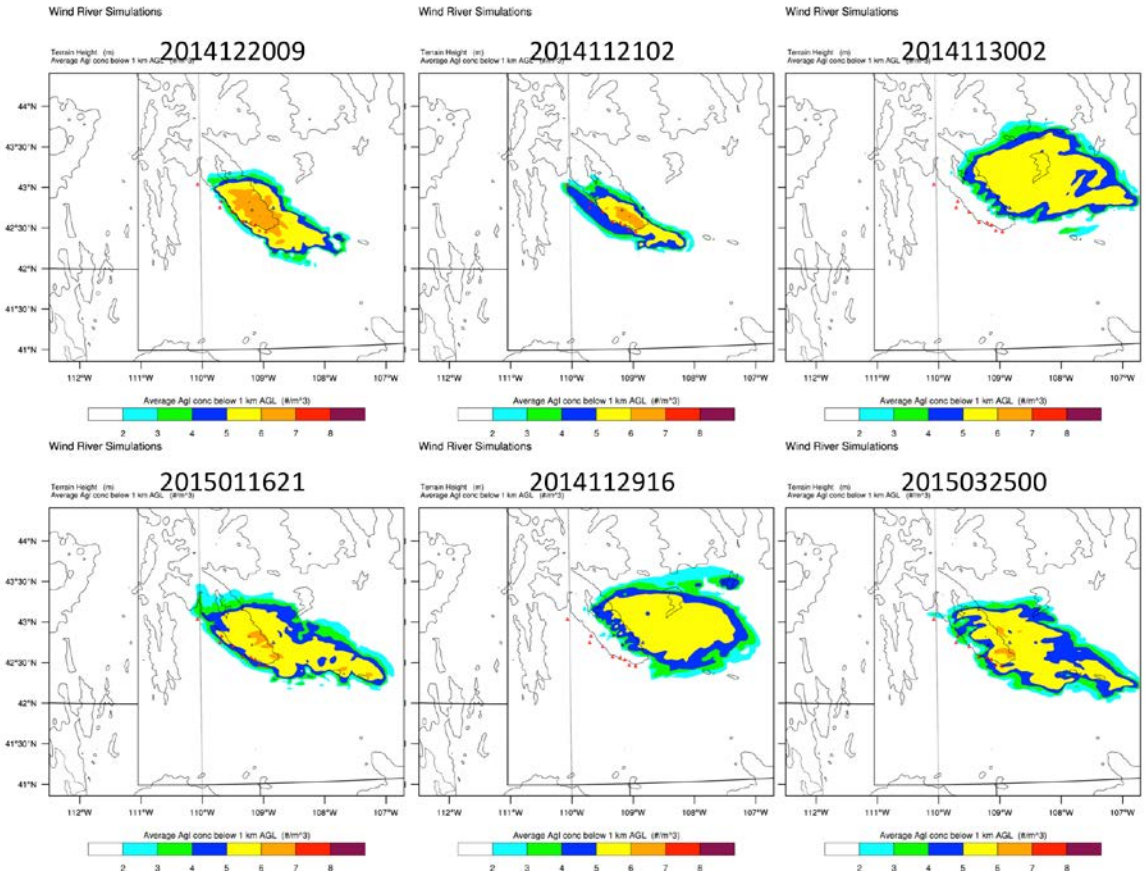

Figure 4.30. Same as Figure 4.27, but for the time at the end of the first airborne seeding case.

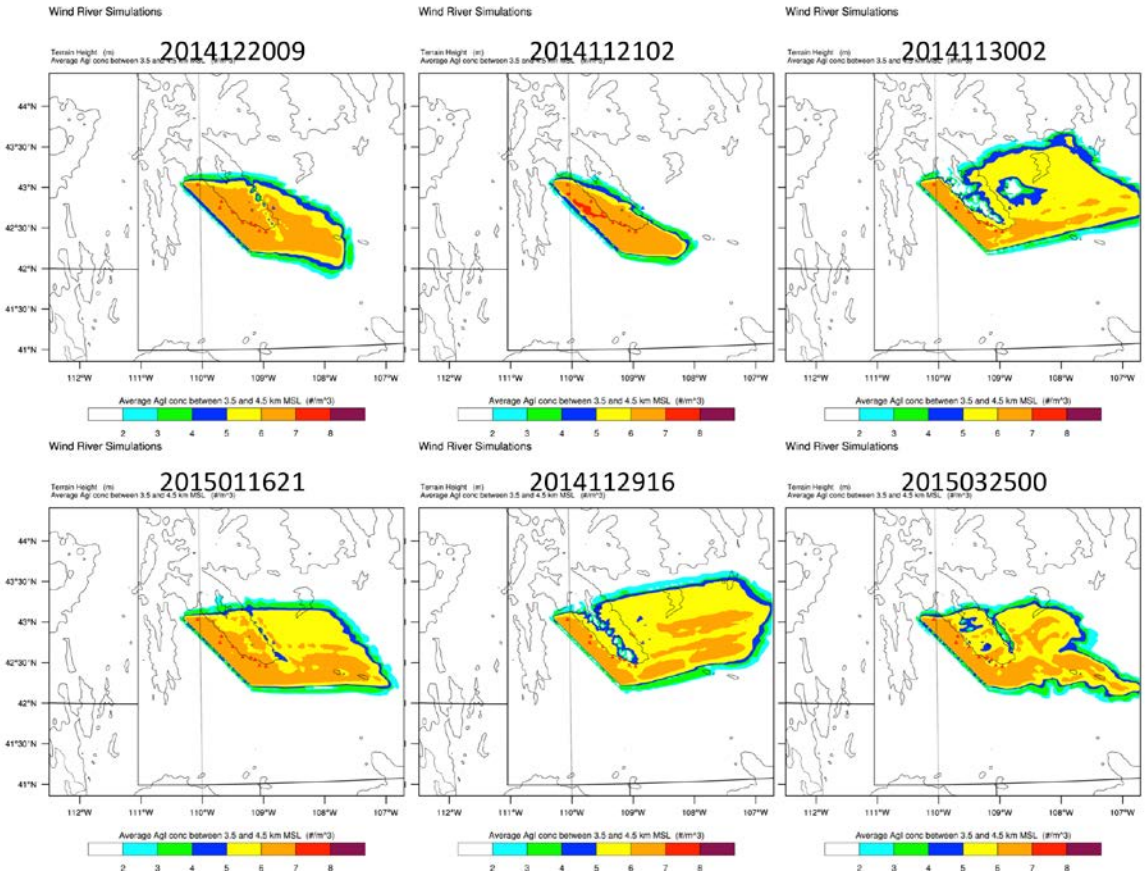

Figure 4.31. Same as Figure 4.28, but for the time at the end of the first airborne seeding case.

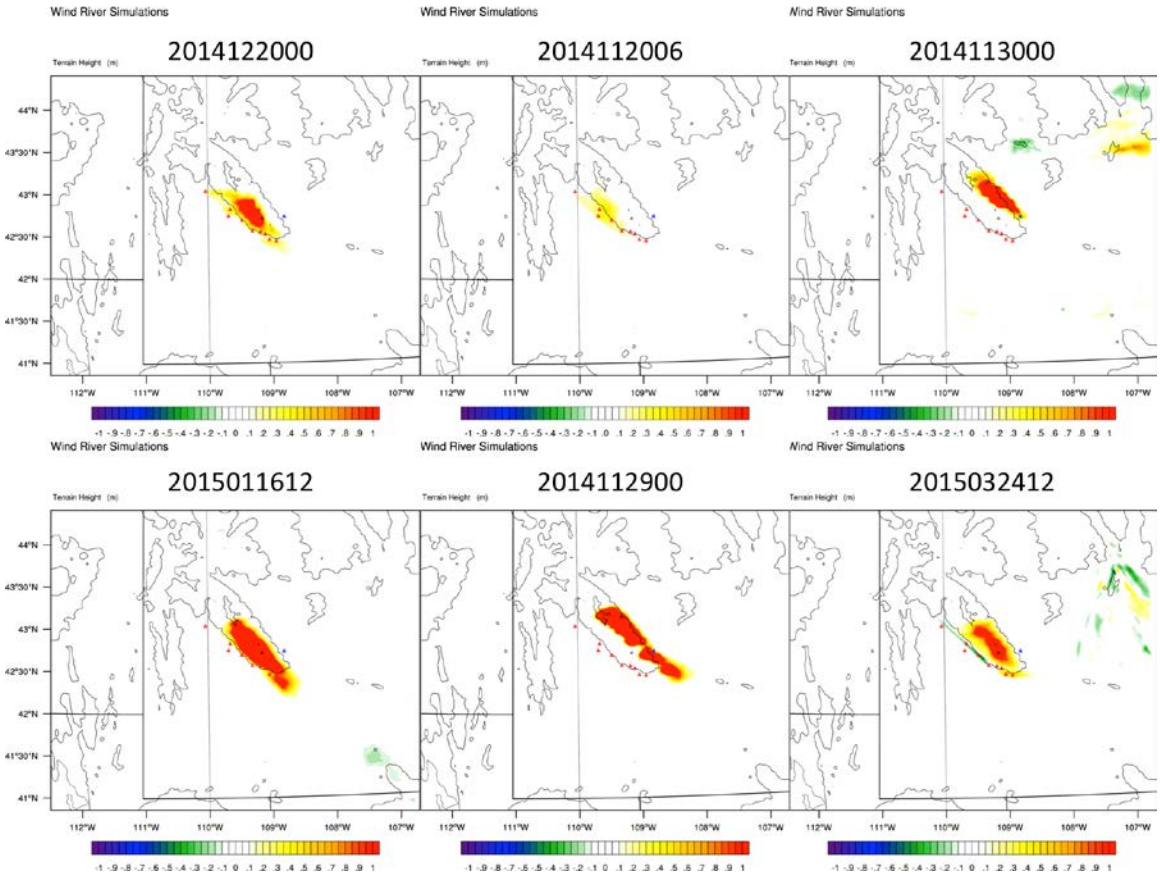

Figure 4.32. Same as Figure 4.29, but for airborne cases.

4.5. Summary of Modeling Efforts

Based on the seasonal simulated ground seeding statistics from the 2014–2015 winter season, ground-based seeding in the Wind River Range was not effective possibly due to the prevailing stable conditions in this region that limits the horizontal and vertical dispersion of the AgI particles. It is also possible that this particular season was anomalous in terms of its seedability.

The airborne seeding simulations of the six forecasts suggested that airborne seeding could generate reasonable amounts of precipitation enhancement, especially when dispersion conditions are not good for ground-based seeding. In fact, for the six forecasts simulated, simulated airborne seeding was roughly 2–3 times more effective at enhancing precipitation than simulated ground-based seeding in the majority of those cases.

5. Discussion

This analysis suggests that the effectiveness of ground seeding in the Wind River Range may be limited, at least for the one season simulated in this study. A key limitation identified by this analysis is the stability of the air mass to the west of the Wind River Range. Analysis of the 18 soundings released by WMI from Pinedale, WY (west of the Range) shows that 16 of the 18 soundings had stable or inversion layers below 650 hPa (~crest height of the Wind River Range) and 12 of 18 below 750 hPa (maximum elevation of ground generators). Considering just the soundings released on days when west slope seeding cases were called (15 of the 18 soundings), stable or inversion layers below 650 hPa (750 hPa) were present in 14 (11) of the 15 soundings (see Figure 5.1 for a sample of these soundings).

A similar analysis was also performed for the east slope seeding cases. On the east slope, the single ground generator is located at about 800 hPa and using the most recent Riverton sounding released before the start of each east slope seeding case, 5 of the 11 east slope seeding cases had inversions or stable layers between 750–800 hPa and 7 of 11 between 650-800 hPa. That means greater than 70% (50%) of the west (east) slope cases may have had limited AgI dispersion up and over the mountain barrier. A few other signs that the air mass to the west of the Range may frequently be stable are the high frequency of LWC near the surface in the climatology spatial mapping analysis (Figure 3.34b), which indicates frequent low-level cloudy conditions (i.e., fog) and comments from Sublette County Conservation District representatives that ozone is a concern in the Eden Valley (Kathy Raper, personal communication, 2014). Generally, that area may be in a region of subsidence as airflow from the west over the Wyoming Range.

The presence of inversions or stable layers in this region will limit the dispersion of AgI up and over the mountains, while airborne seeding showed more promise due to its ability to distribute the AgI above the stable layers. A possible solution would be to ensure that the ground-based generators are placed at elevations above the most frequent inversion and stable layer heights. Alternatively, the draft report of the Phase II Feasibility Study in the Wyoming Range (WWDC 2015) showed potential seeding impacts on the Wind River Range from seeding in the Wyoming Range. That study utilized the WRF cloud seeding parameterization to simulate ground seeding in a few selected case studies the simulated impact in the Wind River Range was wind direction and case dependent. Nonetheless, the current results for this past season suggest a very small seeding impact from ground seeding over the Wind River Range. Perhaps this past season was anomalous or the few case studies selected for the Wyoming Range study are not representative examples, therefore it would be good to run this model for complete seasons in both regions and for multiple years to account for season-to-season variability.

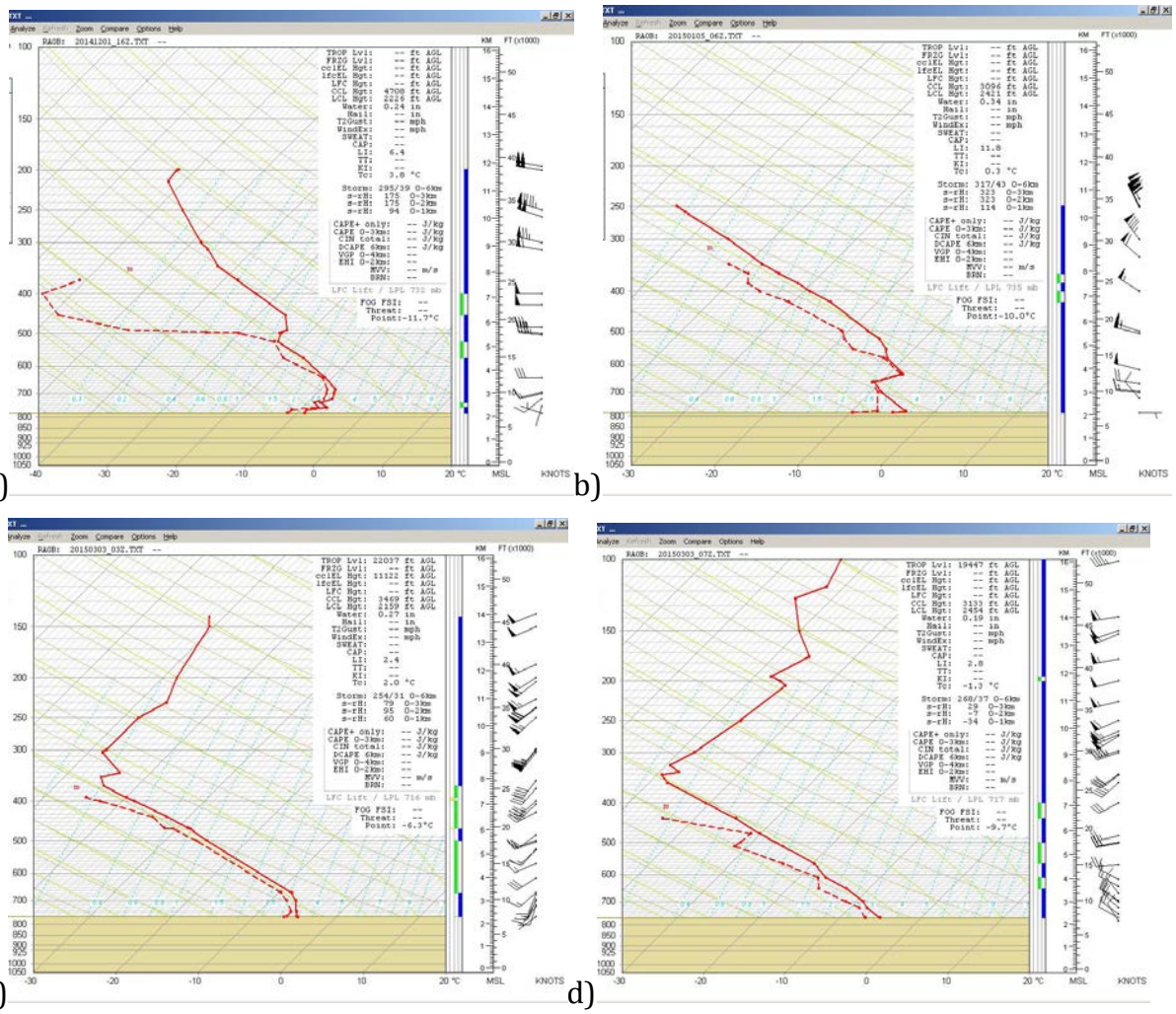

Figure 5.1. Sample of soundings released from Pinedale, WY prior to seeding cases on a) 1 December 2014 at 15:59 UTC, b) 5 January 2015 at 0626 UTC, c) 3 March 2015 at 02:44 UTC, and d) 3 March 2015 at 07:21 UTC. Vertical layers with blue shading along the right side of the plot have stable lapse rates, while those that are conditionally unstable are green.

6. Summary and Recommendations

The purpose of this project was to utilize numerical cloud models to evaluate the potential for cloud seeding to enhance precipitation over the Wind River Range and to assist forecasters in identifying opportunities for cloud seeding over that Range. Three tasks were included in this project: 1) deployment of instrumentation to assist with identifying cloud seeding opportunities and for use in model evaluation, 2) a climatological analysis that utilized an eight-year high-resolution model output to evaluate the cloud seeding potential of storms in the Wind River Range, and 3) real-time forecast modeling activities including adapting a real-time forecast model to identify cloud seeding opportunities over the region and simulate seeding in those cases.

A radiometer and two weather stations were deployed to the Wind River Range as part of Task 1. Data from the radiometer was utilized by the WMI forecasters to call seeding cases for the 2014–2015 winter seeding season, as well as for model evaluation studies. Twenty-one cloud seeding cases were called during the 2014–2015 operational cloud seeding season; 11 on the west slope of the Range. The radiometer data indicated that LWP was present in all of the west slope operational seeding cases, with a typical observed LWP of 0.1 mm or less and a maximum of ~ 0.6 mm (observed in 3 of the 11 west slope cases).

For the second task, an seasonal frequency of seeding opportunities by either ground or airborne seeding on both the west and east slopes of the Wind River Range was performed using an eight year high resolution model dataset (Rasmussen et al. 2014). The typical wind regimes during precipitating events were shown to be westerly to northwesterly, with some southwesterly events, as well as some easterly events on the eastern slopes of the Wind River Range. However, the spatial mapping analysis revealed that LWC is infrequently located on the eastern slopes of the Wind River Range, and therefore the most frequent seeding opportunities were on the western slopes of the Range.

For the eight-year period (2000–2008), SNOTEL data showed that November–April precipitation brings about a half of the annual precipitation to the Wind River Range region. The model indicated that the precipitation is 20 to 100% higher at the crest as compared to the locations of the SNOTEL sites. Additional SNOTEL or snow gauge sites located at these higher locations would be needed verify this result.

The analysis showed high correlations between nearby SNOTEL sites on the same side of the Wind River Range, while sites on the opposite sides of the Range had weaker correlations. This suggests that precipitation does not fall equally on both sides of the Range in a given storm or that precipitation on each side of the Range may result from different storm systems. At several SNOTEL sites the model compared quite well with the observations, however aside from that there was a general tendency for the model to overestimate precipitation. This tendency may be related to the model's slightly wet bias, tendency to have stronger wind, and/or slightly different wind direction, as revealed by comparing with the Riverton soundings. It may also be due to the known undercatch of SNOTEL gauges during windy conditions.

Based on 0–1 km AGL average temperature and LWC criteria, ground seeding had more frequent opportunities than airborne during the November–April wintertime period. When considering the additional criteria for ground-based seeding (wind direction and stability

for transporting ground-released AgI into the targeted clouds), airborne seeding potential at 4–5 km MSL had similar frequencies as ground seeding, with some overlap in the cases between the two layers. A combined airborne and ground program could yield roughly 45% more cases per winter season relative to a ground-based program alone.

The climatology analysis indicated that airborne seeding would be possible outside of the November–April period, and therefore the frequency of seeding opportunities was evaluated over the full year. The full year analysis was conditional on when snow occurred in the mountains, and indicated that airborne seeding year-round can provide, on average, 100 additional hours of opportunities to augment snowfall beyond the number of seedable hours when snow occurred in the November–April period. This suggests the possibility to extend snowpack augmentation activities into the beginning of the runoff season.

Approximately half the time when cloud seeding conditions were present, precipitation occurred over the Wind River Range. This indicates there are some situations with very low precipitation efficiency in which cloud seeding could have potential benefits. Roughly half of the precipitation that fell in a given season was seedable based on ground-seeding criteria being met. Slightly less than half of the precipitation that fell in a given winter season was seedable by airborne seeding.

For the third task, the RT-FDDA version of the WRF model was run in real time during the 2014–2015 winter season over the Wind River Range. WMI forecasters utilized this tailored forecast model output, along with the real-time data from the microwave radiometer, to identify cloud seeding opportunities during the operational seeding program. Software engineering work was completed to set up a real-time cloud seeding forecast system with the RT-FDDA model. The cloud seeding forecast system included the case-calling algorithm that was adapted to run on the RT-FDDA model output to automatically assess the forecast conditions for cloud seeding opportunities. When cloud seeding opportunities were identified by the case-calling algorithm, a second forecast model simulation was initiated that explicitly simulated cloud seeding to provide a forecast of the simulated effects from seeding. The cloud seeding forecast system was run retrospectively for the 2014–2015 and results from those model simulations were analyzed to provide an estimate of the potential seasonal impact from seeding and to compare the model-identified seeding cases with those identified by the forecasters in order to improve the case-calling algorithm.

The model results were also compared against observations from the radiometer and other available measurements (i.e., snow gauges, atmospheric soundings) to evaluate the model's performance.

An important finding was that the model results indicated a very small simulated seeding effect over the Range for ground-based seeding for the 2014–2015 season. The likely reason for this was the presence of stable layers in the upstream sounding, causing the ground generator AgI plumes to be largely diverted around the Range. Adding airborne seeding increased the simulated seeding effect, making it roughly 2–3 times more effective than ground-based seeding, as it was able to target the upper liquid water layer without being significantly blocked by the Range. Additional years of simulations are needed, including sounding data, to confirm this result.

6.1. Recommendations

From the analyses presented herein, we provide eight recommendations related to improving the efficacy of the cloud seeding program in the Wind River Range.

1) We recommend running the real-time cloud seeding forecast system in real time for additional Wyoming operational seeding seasons. There are at least three purposes for these recommended model simulations:
    a. It would provide a tailored forecast model for operational forecasters that would include forecast trajectories from generators and simulated seeding effects forecasts prior to the forecaster calling cases.
    b. The seasonal seeding forecast model output can be used to assess *seasonal* simulated seeding effects for the various basins. This provides a means to evaluate the operational program while also helping proportion where the benefits may accrue (i.e. as shown in Table 4.6–Table 4.9), which can help in determining future cost share arrangements.
    c. It would provide multiple years of simulated seeding effects in order to evaluate how the seasonal simulated seeding impacts vary by season, thereby also resolving if the 2014–2015 season was anomalous. A key aspect of this effort would be to collect and analyze sounding data for each event in order to determine the stability of the air flowing over the Range.
2) We recommend further refinement to the case-calling algorithm to better match operational case calling.
3) We recommend continued radiometer measurements and local soundings to identify seeding cases in the region. These data also provide valuable data for validation of any associated modeling activities. If funds allow, we would recommend a second radiometer on the northwestern side of the Range to capture the high liquid water contents identified in the eight year climatology that often occurred independent of the liquid water content observed by the Boulder radiometer.
4) We recommend the deployment of snow gauges along the crest of the Wind River Range to obtain precipitation measurements to verify the model results in this portion of the Range. The model suggests that the highest snowfall occurs in this region, and thus it is important to know whether this is true or not. This recommendation is challenging due to land use and ownership in those regions, but is a need nonetheless. We recommend using the model eight-year dataset to identify the best sites by doing a correlation analysis between existing gauge sites and potential new sites to identify the best, yet fewest, locations needed for additional gauges.
5) We recommend considering airborne seeding in the region to extend the seeding season, while also providing additional opportunities for seeding, especially for cases that are stable and limit the potential for ground-based seeding dispersion of AgI over the target area.
6) As a follow-on recommendation to #1, we recommend developing a real-time integrated display of the model and observations, which includes the model output

compared to observations for real-time model verification, to aid forecasters in cloud seeding case calling.

7) Conduct additional analysis on the eight-year model dataset by running the case-calling algorithm to identify cases, and conducting both ground and airborne seeding simulations on cases so identified. Annual simulated seeding impacts due to ground, airborne, and the two combined would be estimated and related to the stability of the oncoming flow. This differs from Recommendation #1c in that sounding data would not be available to verify the results, but has the advantage of considering multiple years without having to wait for multiple future seeding seasonal forecasts to be run as in Recommendation #1.
8) Future studies should evaluate ability of the model to vertically disperse AgI from the ground generators over the complex terrain of the Wind River Range using Large Eddy Simulation approach.

References

Barker, D.M., W. Huang, Y.-R.Guo, A.J. Bourgeois and Q.N.Xiao, 2004: A Three-Dimensional Variational Data Assimilation System for MM5: Implementation and Initial Results. *Mon. Wea. Rev.,* **132**, 897–914.

Barlage, M., F. Chen, M. Tewari, K. Ikeda, D. Gochis, J. Dudhia, R. Rasmussen, B. Livneh, M. Ek, and K. Mitchell, 2010: Noah Land Surface Model Modifications to Improve Snowpack Prediction in the Colorado Rocky Mountains. *J. Geophys. Res.*, 115, DOI: 10.1029/2009JD013470.

Caro, D., W. Wobrock, A.I. Flossman, and N. Chaumerliac, 2004: A two-moment parameterization of aerosol nucleation and impaction scavenging for a warm cloud microphysics: Description and results from a two-dimensional simulation. *Atmos. Res.,* **70**, 171-208.

Chen, S. and J. Dudhia, 2000: Annual Report: WRF Physics. NCAR/MMM Internal Reportavailable at http://www.mmm.ucar.edu/wrf/users/docs.

Chen, F., and J. Dudhia, 2001: Coupling an advanced land surface-hydrology model with the Penn State-NCAR MM5 modeling system. Part I: Model implementation and sensitivity. *Mon. Wea. Rev.,* **129**, 569-585.

Collins, W. D., and Coauthors, 2006: The Community Climate System Model version 3 (CCSM3). *J. Climate*, **19**, 2122–2143, doi:10.1175/JCLI3761.1.

DeMott, P.J., 1995: Quantitative descriptions of ice formation mechanisms of silver iodide-type aerosols. *Atmos. Res.*, **38**, 63-99.

DeMott, P.J., 1997: Report to North Dakota Atmospheric Resource Board and Weather Modification Incorporated on tests of the ice nucleating ability of aerosols produced by the Lohse airborne generator. Report from Dept. Atmos. Sci., Colorado State Univ., Fort Collins, CO, 15 pp.

Dudhia, J. 1989: Numerical study of convection observed during the winter monsoon experiment using a mesoscale two-dimensional model. *J. Atmos. Sci.,* **46**, 3077-3107.

Eilers, Paul HC and Hans FM Boelens, 2005: Baseline correction with asymmetric least squares smoothing. Leiden University Medical Centre Report.

Hong, S.-Y., and H.-L. Pan, 1996: Nonlocal boundary layer vertical diffusion in a medium-range forecast model. *Mon. Wea. Rev*.,**124**, 2322–2339.

Hong, S.-Y., Y. Noh, and J. Dudhia, 2006: A new vertical diffusion package with an explicit treatment of entrainment processes. *Mon. Wea. Rev*., **134**, 2318–2341, doi:10.1175/MWR3199.1.

Ikeda, K. and Coauthors, 2010: Simulation of seasonal snowfall over Colorado. *Atmos. Res*., **97**,462-477.

Janjic Z. I., 1994: The step-mountain Eta coordinate model: Further developments of the convection, viscous layer, and turbulence closure schemes. *Mon. Wea. Rev*., **122**, 927–945, doi:10.1175/1520-0493(1994)122,0927:TSMECM.2.0.CO;2.

Janjić, Z.I., 1996: The surface layer in the NCEP Eta Model. *Eleventh Conference on Numerical Weather Prediction*, Norfolk, VA, 19-23 August 1996; Amer. Meteor. Soc., Boston, MA, 354-355.

Janjic, Z. I., 2002: Nonsingular Implementation of the Mellor Yamada Level 2.5 Scheme in the NCEP Meso model. NCEP Office Note, No. 437, 61pp.

Johnson, J. B., and D. Marks, 2004: The detection and correction of snow water equivalent pressure sensor errors. *Hydrological Processes*, **18**, 3513-3525.

Kessler, E., 1969: On the distribution and continuity of water substance in atmospheric circulations. *Meteor. Monogr*., No. 32, Amer. Meteor. Soc., 84 pp.

Klemp, J.B., W.C. Skamarock, and O. Fuhrer. 2003: Numerical Consistency of Metric Terms in Terrain-Following Coordinates. *Mon. Wea. Rev.,* **131**, 1229–1239.

Meyers, M.P., P.J. DeMott, and W.R. Cotton, 1995: A comparison of seeded and nonseeded orographic cloud simulations with an explicit cloud model. *J. Appl. Meteor.,* **34**, 834-846.

Mikalakes, J., J. Dudhia, D. Gill, T. Henderson, J. Klemp, W. Skamarock, and W. Wang, 2004: The Weather Research and Forecast Model: Software Architecture and Performance. *Proceeding of the Eleventh ECMWF Workshop on the Use of High Performance Computing in Meteorology. 25 - 29 October 2004, Reading, U.K.*

Milbrandt, J.A., and M.K. Yau, 2005a: A multimoment bulk microphysics parameterization. Part I: Analysis of the role of the spectral shape parameter. *J. Atmos. Sci.,* **62**, 3051-3064.

Milbrandt, J.A., and M.K. Yau, 2005b: A multimoment bulk microphysics parameterization. Part II: A proposed three-moment closure and scheme description. *J. Atmos. Sci.,* **62**, 3065-3081.

Mlawer, E. J., S. J. Taubman, P. D. Brown, M. J. Iacono, and S. A. Clough, 1997: Radiative transfer for inhomogeneous atmosphere: RRTM, a validated correlated-k model for the long-wave. *J. Geophys. Res*., **120** (D14), 16663-16682.

Poore, K., J-H. Wang, and W. B. Rossow, 1995: Cloud layer thicknesses from a combination of surface and upper air observations. *J. Climate*, **8,**550–568.

Rasmussen, R., and Coauthors, 2011: High-resolution coupled climate runoff simulations of seasonal snowfall over Colorado: A process study of current and warmer climate. *J. Climate*, **24**, 3015–3048.

Rasmussen. R, and Coauthors, 2012: How well are we measuring snow? The NOAA/FAA/NCAR Winter Precipitation Test Bed: *Bull. Amer. Meteorol. Soc.*, **93**, 811–829.

Rasmussen. R., and Coauthors, 2014: Climate change impacts on the water balance of the Colorado Headwaters: High-resolution regional climate model simulations. *J. Hydro. Meteor.,* **15,** 1091–1116.

Ritzman, J., T. Deshler, K. Ikeda, and R. Rasmussen, 2015: Estimating the fraction of winter orographic precipitation that is produced under conditions meeting the seeding criteria from the Wyoming weather modification pilot project. *J. Appl. Meteor. Climatol.*, **54**, 1202–1215.

Serreze, M. C., M. P. Clark, R. L. Armstrong, D. A. McGinnis, and R. S. Pulwarty, 1999: Characteristics of the western United Stated snowpack from snowpack telemetry (SNOTEL) data. *Water Resour. Res.*, **35**, 2145-2160.

Serreze, M. C., M. P. Clark, and A. Frei, 2001: Characteristics of large snowfall events in the montane western United States as examined using snowpack telemetry (SNOTEL) data. *Water Resour. Res.,* **37**, 675-688.

Skamarock, W.C., 2004: Evaluating mesoscale NWP models using kinetic energy spectra. *Mon. Wea. Rev*., **132**, 3019–3032.

Skamarock, W. C., J. B. Klemp, J. Dudhia, D. O. Gill, D. M. Barker, W. Wang, and J. G. Powers, 2005: A description of the Advanced Research WRF version 2. NCAR Tech. Note NCAR/TN-4681STR, 88 pp. [Available online at www.mmm.ucar.edu/wrf/users/docs/arw_v2.pdf.]

Skamarock, W.C. and Coauthors, 2008: A description of the Advanced Research WRF Version 3. NCAR Tech. Note NCAR/TN-4751STR, 113 pp. [Available online athttp://www.mmm.ucar.edu/wrf/users/docs/arw_v3_bw.pdf.]

Thompson, G., R.M. Rasmussen, and K. Manning, 2004: Explicit forecasts of winter precipitation using an improved bulk microphysics scheme. Part I: Description and sensitivity analysis. *Mon. Wea. Rev*., **132**, 519-541.

Thompson, G., P. R. Field, R. M. Rasmussen, and W. D. Hall, 2008: Explicit forecasts of winter precipitation using an improved bulk microphysics scheme. Part II: Implementation of a new snow parameterization. *Mon. Wea. Rev*., **136**, 5095–5115.

Wang, J., H.L. Cole, D.J. Carlson, E.R. Miller, K. Beierle, A. Paukkunen, and T.K. Laine, 2002: Corrections of humidity measurement errors from the Vaisala RS80 radiosonde—Application to TOGA COARE data. *J. Atmos. Oceanic Technol.*, **19,** 981–1002.

WWDC, 2014: The Wyoming Weather Modification Pilot Program – Level II Study, Draft Executive Summary, NCAR, 15 pp. (available at http://wwdc.state.wy.us/)

WWDC, 2015: Weather Modification Feasibility – Wyoming Range – Level II, Phase II Study, NCAR, 183 pp. (submitted to Wyoming Water Development Office, July 2015)

Yang, D., B.E. Goodison, J.R. Metcalfe, V.S. Golubev, R. Bates, T. Pangburn, and C.L. Hanson, 1998: Accuracy of NWS 8" standard nonrecording precipitation gauge: results and application of WMO intercomparison. *J. Atmos and Oceanic Technol.*, **15**, 54–68.

List of Acronyms

ACARS - Aircraft Communications Addressing and Reporting System

AgI – Silver iodide

AGL – Above Ground Level

AS - lower airborne seeding layer

ASH - higher airborne seeding layer

AsLS - asymmetric least squares smoothing

CCN - cloud condensation nuclei

GFS - Global Forecast System

GS - ground seeding

LWC – Liquid Water Content

LWP – Liquid Water Path

MM5 – Mesoscale Model 5

MSL – Mean Sea Level

MYJ – Mellor-Yamada-Janjic

NADP - National Atmospheric Deposition Program

NCAR – National Center for Atmospheric Research

NESDIS - National Environmental Satellite, Data, and Information Service

PDF - probability density function

NRCS - Department of Agriculture Natural Resource Conservation SErvice

NWS – National Weather Service

PBL – Planetary Boundary Layer

PWAT - Precipitable Water

RAL – Research Applications Laboratory

RAMS – Regional Atmospheric Modeling System

RRTM - Rapid Radiate Transfer Model

RT-FDDA – Real-Time Four-Dimensional Data Assimilation modeling system

SLW – Supercooled Liquid Water

SNOTEL – Snow Telemetry precipitation gauges

USFS – United States Forest Service

WMI – Weather Modification Incorporated

WRF – Weather Research and Forecast model

WRR - western Wind River Range

WRR-E - eastern Wind River Range

WWDC – Wyoming Water Development Commission

WWMPP – Wyoming Weather Modification Pilot Program

YSU - Yonsei University